On the Characteristics and Evolution of Dynamically Excited Trans-Neptunian Objects

by

Cory Shankman
B.Sc., University of Western Ontario, 2010
M.Sc., University of British Columbia, 2012

A Dissertation Submitted in Partial Fulfillment of the
Requirements for the Degree of

DOCTOR OF PHILOSOPHY

in the Department of Physics and Astronomy

© Cory Shankman, 2016
University of Victoria

All rights reserved. This dissertation may not be reproduced in whole or in part, by photocopying or other means, without the permission of the author.

On the Characteristics and Evolution of Dynamically Excited Trans-Neptunian Objects

by

Cory Shankman
B.Sc., University of Western Ontario, 2010
M.Sc., University of British Columbia, 2012

Supervisory Committee

Dr. JJ. Kavelaars, Co-Supervisor
(NRC Herzberg)

Dr. F. Herwig, Co-Supervisor
(Department of Physics and Astronomy)

Dr. F. Nathoo, Outside Member
(Department of Mathematics and Statistics)

Supervisory Committee

Dr. JJ. Kavelaars, Co-Supervisor
(NRC Herzberg)

Dr. F. Herwig, Co-Supervisor
(Department of Physics and Astronomy)

Dr. F. Nathoo, Outside Member
(Department of Mathematics and Statistics)

ABSTRACT

The small-body populations of the distant Solar System inform our understanding of the structure, formation, and evolution of the Solar System. The orbits of these Trans-Neptunian Objects (TNOs) act as tracers for dynamical activities either ongoing or past. The distributions of TNO sizes are set by, and so probe, the conditions of the formation and evolution of the Solar System.

Using data from surveys on the Canada-France-Hawaii Telescope, I constrain the size distribution of a TNO subpopulation: the scattering TNOs. The scattering TNOs are chosen as they have orbits that come in closer to the Sun, therefore allowing smaller TNOs to be detected. The characteristics of size distribution for the small-sized TNOs is an important, and only recently observable, constraint on the formation of this population. I find that the H-distribution is consistent with models where TNOs form as large (50 km - 100 km) aggregates from the proto-planetary nebula.

A recent discovery of apparent clustering in the orbits of some TNOs has led to the hypothesis of an additional and unseen planet in the distant Solar System. I examine the formation implications and consequences of such a planet, and the biases in the detected sample used to infer the planet's existence. Via a combination of dynamical simulations, survey simulations, and statistical comparisons of the observed TNOs, I explore the additional planet hypothesis to determine if there exists strong evidence for an additional planet in our Solar System. I find that there is currently no strong evidence for the clustering of orbits in the observed sample and that the proposed additional planet does not produce such a signature in models.

Contents

List of Tables

List of Figures

CO-AUTHORSHIP

This thesis contains collaborative published or submitted works in Chapters 2, 4, 5, and 6. A note at the start of each chapter provides the full author list, state of publication, and reference details for the publication. All works in this thesis were developed with the guidance and insight of my thesis supervisor, JJ Kavelaars.

Much of this work is built on analyzing the detections of several surveys. The work of those surveys is noted in each published paper. All detections and survey characterisations were provided by the teams leading the surveys. In particular, Michele Bannister, JJ Kavelaars, Brett Gladman, Mike Alexandersen, Katherine Volk, and Jean-Marc Petit were instrumental in designing and carrying out the surveys that provide the detected samples in this Thesis.

Chapter 2 was entirely written by me, with contributions to the observing section from JJ Kavelaars. I performed all survey simulations, made all plots, and computed all statistics. This approach is based on previous work of mine, with contributions to the approach made by Brett Gladman at the time. Proofreading and editing was provided by co-authors and in particular by JJ Kavelaars.

Chapter 4 was primarily written by Samantha Lawler. I contributed to the writing of the introduction, wrote parts of Section 4.4, and provided general editing and proofreading. The idea for this project was proposed by Samantha Lawler and developed by Samantha and myself. I performed initial simulations to determine the feasibility of the idea and the approach for the project. Working with Samantha, I helped to develop the approach, scientific questions, and methods within the paper. I wrote code for the plotting, statistical analysis, control of the survey simulator, and computation of population and mass estimates in the paper. The formation simulations and the paragraph describing them were contributed by Nathan Kaib. JJ Kavelaars, Brett Gladman, and Michele Bannister provided helpful discussion throughout the process.

I developed the ideas for Chapter 5 and Chapter 6, wrote the full text, performed all simulations, and made all of the figures for each chapter. For both chapters, JJ Kavelaars, Brett Gladman, Michele Bannister, and Samantha Lawler provided helpful discussion throughout in addition to proofreading and editing.

ACKNOWLEDGEMENTS

This has been a long journey. I don't really know where it started and in many ways this won't be the end of this story. Many people have touched me along the way, supporting, guiding, and giving meaning to my life. Thank you to those below and to those I didn't have the space to mention by name.

Ian Fisher, Greg Michalski, David Grant, Michael Jansen, for nurturing my interest in science and answering my endless hypothetical questions.

Shantanu, Paul, Peter, Pauline, for your guidance throughout my B.Sc.

All my Western friends, especially Chris, the other half of my graduating class.

My officemates and cohorts for putting up with me over the years.

Brett, for guiding me through my M.Sc. and for your continual insight into all things TNO.

Mike, Rosemary, Sam, for being my research sounding board and complaint shoulder.

Sylvia and Fern, for always brightening my days.

Dela, Flo, Hannah, Mike, Rosemary, Sam, Robert, Ryan, Nick, for keeping me grounded and for being the support I needed.

All of my friends in the GSS, Senate, and University Administration for helping me find the way to my next path.

My family, for always supporting who I am and what I do. For whatever has been or will be, family is family.

And lastly, JJ, for your guidance and your support without which I never would have made it here.

All the works by people you and I admire sit atop a foundation of failures.
Pierce Brown

Science is a wonderful thing if one does not have to earn one's living at it.
Albert Einstein

Chapter 1

Introduction

The Solar System is humanity's small corner of existence.

Our understanding of the Solar System has changed dramatically throughout history and in many ways our understanding of the Solar System remains incomplete. Fundamentally, we study the Solar System in search of the answers to existential questions such as: how did the Solar System form and evolve, what factors led to the formation of life in our Solar System and what does this mean for the existence of life elsewhere in the universe? The state of scientific inquiry on the small bodies in the far outer Solar System is focused on detecting, classifying, and measuring the physical properties of the vast swarm of planetesimals that enring the Solar System. This work focuses on measuring the physical properties and orbits of these distant planetesimals, the Trans-Neptunian Objects (TNOs), so-called because their orbits pass beyond the orbit of Neptune. This work develops our understanding of the composition and formation of this distant region of our Solar System, partially forming the basis for addressing the first of the above questions: how did the Solar System form and evolve?

It is not possible to directly observe the conditions and processes that led to the formation of the Solar System, however, we can infer the conditions from the properties of the planetesimals formed by those processes. The small-body populations of the outer Solar System (i.e. the TNOs) are some of the least processed bodies by collisions and surface weathering in the Solar System (Barucci et al., 2008; Leinhardt et al., 2008) and thus best preserve the signatures of the initial conditions of the Solar System. The orbits and physical characteristics of planetesimals in the outer Solar System can be used as a probe of the formation conditions and massive-body dynamics history of the Solar System.

Today we know that there is a large population of planetesimals (the remnant small bodies of the planet formation process) that orbit beyond Neptune. This ensemble is sometimes referred to as the Kuiper Belt or the Edgeworth-Kuiper Belt for historical, and sometimes controversial, reasons. This author prefers to refer to these planetesimals simply as TNOs, avoiding any historically based naming convention. The prediction for the existence of this population is now often recognized to be shared between Kenneth Edgeworth and Gerard Kuiper. The origins for these theories, however, can be traced to the discovery of Pluto.

Erroneous calculations in the orbit fitting of Uranus and Neptune led to the suggestion of an unseen planet beyond Neptune (Davies et al., 2008). Though the underpinning theory was incorrect, Clyde Tombaugh serendipitously discovered Pluto in 1930 in an exhaustive search conducted at Lowell Observatory. For the next 76 years, until Pluto's reclassification, the Solar System would be thought of as a nine-planet system. The reasons for Pluto's demotion, and the seeding idea for the hypothesis of Edgeworth/Kuiper Belt come from the same conclusion: Pluto is but one member of a large population of remnant debris from the formation of this region.

The discovery of Pluto made it clear that there must be more mass in the distant Solar System. Edgeworth was the first to attempt to quantify the mass in this regions, thus postulating the existence of a large reservoir of planetesimals (Edgeworth, 1943, 1949). Later, Kuiper would consider the formation of a planetary disk between 38 astronomical units[1] (au) and 50 au via condensation of volatiles (Kuiper, 1951). Today we know there to be a belt of TNOs in this range, the so-called classical Kuiper Belt, that is believed to have formed in situ (Parker & Kavelaars, 2010), as well as a more extended disk believed to have been transported there during the migration of Neptune (e.g. see Gomes, 2003; Levison et al., 2008; Batygin & Brown, 2010; Nesvorný, 2015). These theories helped to develop a cohesive picture of the Solar System, providing a potential source for previously discovered dynamically unstable small-body populations like the centaurs and Jupiter Family Comets (JFCs).

The first known TNO after Pluto, 1992 QB_1, was detected by Jewitt et al. (1992) in the fall of 1992. This discovery, followed by only a handful of detections over the next few years, led to a new field of Solar System studies. Over the next twenty-five years, the set of known TNOs has expanded to include some three thousand objects.

As the number of detections increased, TNOs were classified into subclasses based

---

[1] The average distance between the Earth and the Sun, approximately 150 million km

on the characteristics and behaviour of their orbits. These classifications identify populations that occupy common orbital space, and thus possibly have a common element to their origin. It is through this classification framework that we study and characterize the present state of the small-body populations in the outer Solar System to probe the formation and evolution history of the Solar System.

The outer Solar System remains an area of active discovery and research. The attention of the scientific community and general public alike have been captured by the recent New Horizons flyby of Pluto and the suggestion that there is another planet in the far reaches of the Solar System (Trujillo & Sheppard, 2014; Batygin & Brown, 2016a). This field of study touches the lives of the general public, and reveals our corner of the cosmic neighbourhood. Now is a good moment in history for the study of the TNO region; major advances in scientific inquiry have been made in a short time and more opportunities await with proposed telescopes and in-space missions.

1.1 Detecting TNOs

> *The history of astronomy is a history of receding horizons.*
>
> Edwin Hubble

Understanding begins with discovery and classification. To first order, whether or not a TNO is detectable is determined by whether or not your telescope has the sensitivity to see faint objects. TNOs are icy rocky bodies with diameters of tens to hundreds of kilometres detected in reflected Solar light at distances of 2–10 billion kilometres (13 au - 65 AU). Telescopes act as light buckets whose capabilities increase with the diameter of the telescope and the integration time of the exposure. Over time we have built larger and more sophisticated telescopes that allow the detection of both more distant and smaller TNOs. Brightness remains one of the major limiting factors for the detections of TNOs today.

Astronomy uses a relative and logarithmic scale for comparing the brightness of two objects: the magnitude system. This system allows for an easy comparison of many objects with vastly different brightnesses and also somewhat corresponds to the logarithmic way the eye perceives light. The difference in magnitude, m, of two objects is defined by the logarithm of the ratio of their fluxes, F:

$$m_1 - m_2 = -2.5 \cdot \log_{10}\left(\frac{F_1}{F_2}\right) \tag{1.1}$$

By convention, Vega has been set as the reference star for the magnitude system, with a defined magnitude of 0. When magnitudes are discussed, they refer to the light collected in a specific wavelength range (called a filter or band). TNO surveys will report their limiting magnitude, that is the magnitude of the faintest detection possible in the survey, as it is one of several important observing biases that must be taken into consideration in the analysis of the survey.

Discovering and characterizing TNOs is a difficult process with many inherent biases. TNOs move from night to night relative to the background stellar field, exhibit phase brightness effects (Benecchi & Sheppard, 2013), and must be imaged multiple times to determine an orbit. At these great distances, a TNO's apparent motion on the sky is dominated not by its own intrinsic motion, but rather results from parallax due to the motion of the Earth. TNOs are not uniformly distributed across the Solar System; TNOs occupy various regions or configurations resulting from their formation history or driven by the dynamics of Neptune (see Section 1.2). In some cases, different TNO populations have unique observational bias effects such as only being detectable at longitudes away from Neptune, or only being detectable near their closest approaches to the Sun. Understanding and modelling the observational biases of surveys is a crucial element for the study of TNO populations (see Section 1.5.1; Kavelaars et al., 2008).

This work uses a family of surveys that were designed on a similar and continually refined observing strategy (Kavelaars et al., 2009), each with well measured and reported survey biases. The surveys are the Canada France Ecliptic Plane Survey (CFEPS; Petit et al., 2011, 2017), Alexandersen et al. (2016), and the Outer Solar System Origins Survey (OSSOS; Bannister et al., 2016). By using wide field cameras and a targeted follow-up strategy, these surveys were able to detect a large number of TNOs and determine orbits quickly, building a dataset of orbit-classified TNOs. Because the surveys were able to determine orbits quickly, they tracked more discoveries and find a more complete sample that does not have biases associated with loss due to rates of motion on the sky. CFEPS, Alexandersen et al. (2016), and OSSOS each measure and report their observing biases, one of several features that distinguishes these surveys from other TNO surveys. Together, these three surveys have detected approximately one third of all known TNOs and half of the TNOs with well determined orbits, producing a powerful set of TNOs with well determined orbits and published observing biases that provides the best foundation for detailed TNO studies.

1.2 Dynamical Classification

All science is either physics or stamp collecting.
Ernest Rutherford

When measuring the bulk physical properties of TNOs, it is essential that these properties have been shaped by the same processes. Several subpopulations of TNOs have been identified and one of the main science goals in TNO studies is to explain the cosmogony of these different subpopulations. TNOs are primarily classified into their subpopulations by their orbital dynamics with the assumption that objects that exhibit the same behaviour likely share the same formation and history - a first order best guess. It is therefore necessary to properly classify TNO orbits when studying their bulk physical properties.

The orbits of Solar System bodies are quantified by the parameters of the elliptical orbit that is consistent with their position and velocity at the time of discovery. Orbits are defined by 6 quantities that describe the shape and orientation of the orbital ellipse as well as the position of the object in its orbit. The orbital parameters are: the semi-major axis (a), the eccentricity (e), inclination (i), longitude of the ascending node (Ω), argument of periapsis or pericentre (ω), and the true anomaly (ν). The semi-major axis and eccentricity describe the size and shape of the orbit while the inclination, longitude of the ascending node, and argument of pericentre define the orientation of the orbit. The true anomaly measures the current location of the object along its orbit. Another quantity regularly used is the mean anomaly, M, which is an angle that advances from pericentre along the orbit uniformly in time and is equivalent to the true anomaly for a circular orbit. Figure 1.1 shows the parameters that define an orbit.

TNOs are classified by forward integrating their orbit via a numerical n-body simulation (see Section 1.5.2) and examining how the orbit evolves over time (Gladman et al., 2008). There are several subpopulations of TNOs (e.g. resonant, scattering, detached, classical belt), each with a unique dynamical relationship to the giant planets. The origins of these different populations as well as the links between them is an open question and the main area of active research in TNO studies. Figure 1.2 shows the dynamical structure of known objects in the TNO region. The complex and overlapping structure of TNOs requires that the orbits of observed TNOs be well determined in order to perform a proper analysis of the bulk properties of a population.

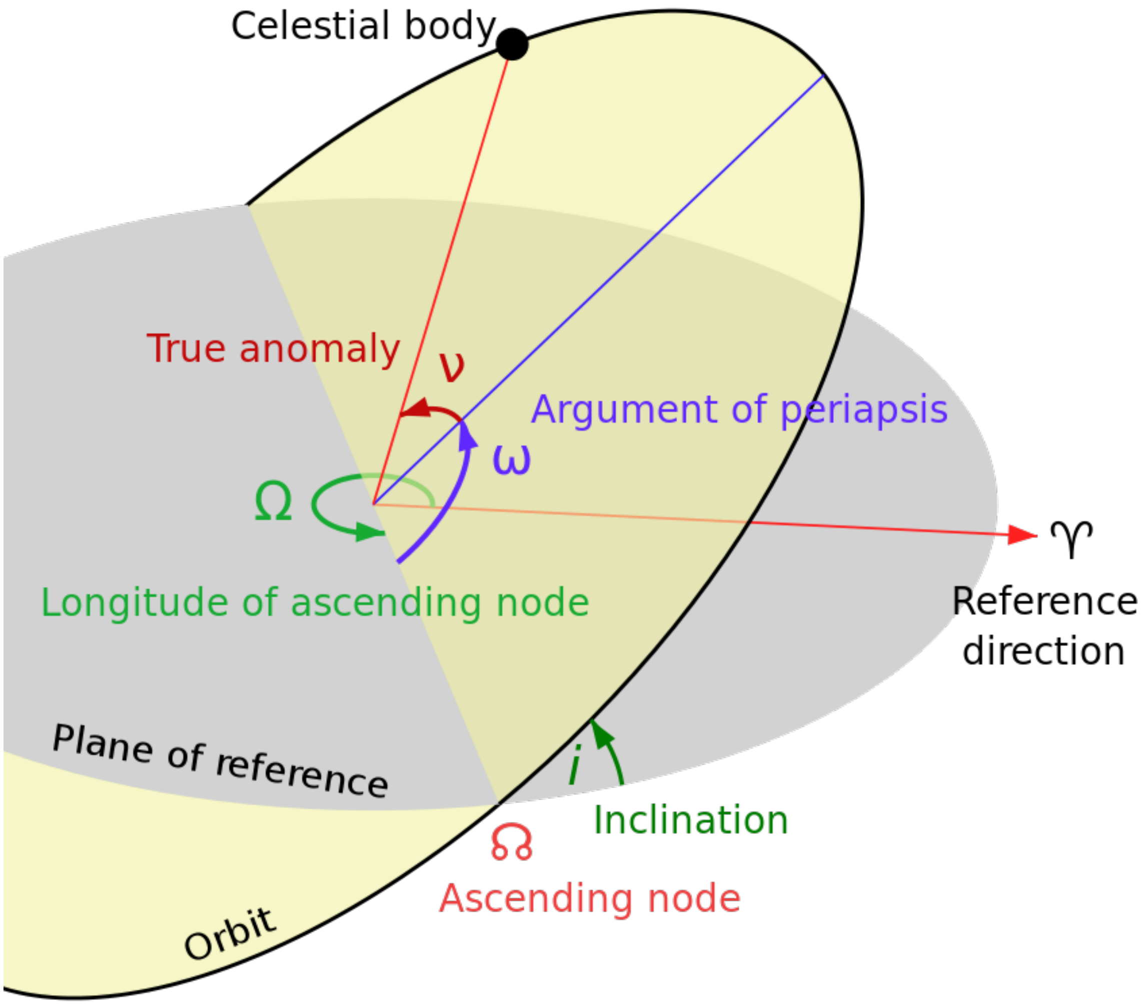

Figure 1.1: The parameters that specify a Keplarian orbit. Diagram sourced from https://en.wikipedia.org/wiki/File:Orbit1.svg, distributed under a CC BY-SA 3.0 license

There are two broad dynamical classes of TNOs: those without excited orbits (i.e. small e, i; the "cold" population) which are believed to have formed in situ and those with excited orbits (i.e. large e, i; the "hot" populations) believed to have been transplanted to their current locations. This thesis focuses primarily on the largest-orbit TNOs across two subclasses: scattering and detached.

The scattering TNOs have strong dynamical interactions with Neptune that change their orbits on short timescales; they are scattered by Neptune. Scattering TNOs are defined as those which undergo an evolution in a of ≥ 1.5 au within 10 Myr (Gladman et al., 2008).

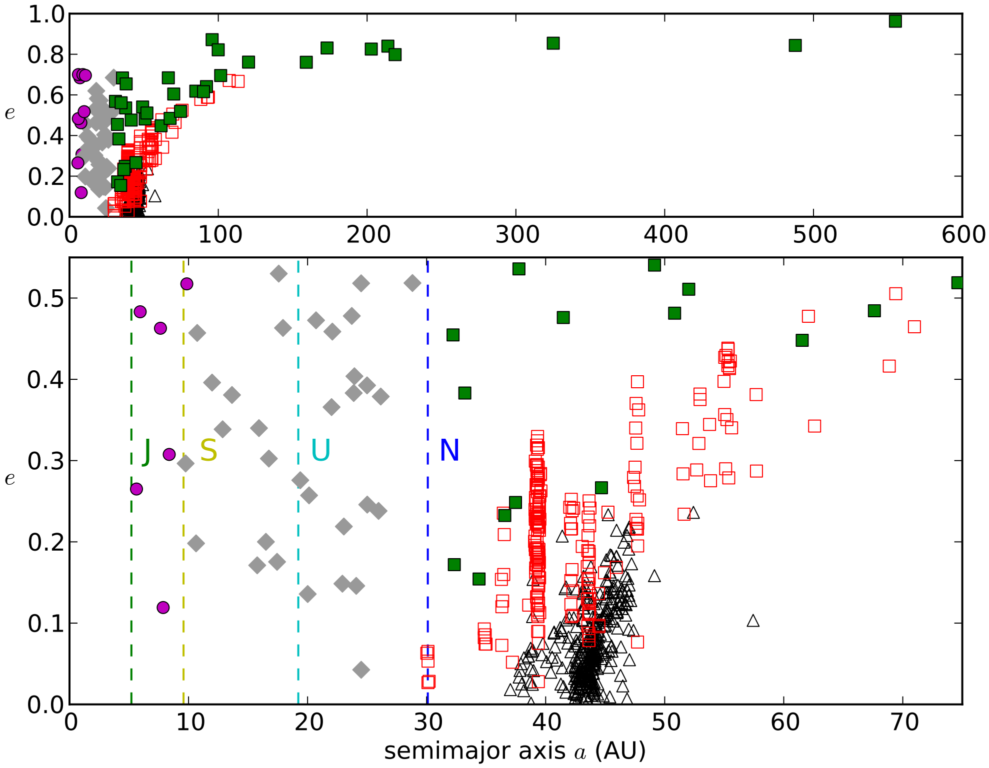

Figure 1.2: a vs e for known TNOs and outer Solar System objects. The orbital distances of the giant planets (Jupiter, Saturn, Uranus, and Neptune) are indicated with dashed lines. Five subpopulations are plotted: resonant objects (red open squares), scattering objects (green squares), classical belt objects (black open triangles), centaurs (grey diamonds), and Jupiter-family comets (magenta circles). Data from the International Astronomical Union's Minor Planet Center. This figure appears in Shankman (2012) and is reproduced with permission.

The detached TNOs have a pericentre[2], q, that is beyond the influence of the giant planets (Lykawka & Mukai, 2007b; Gladman et al., 2008), but a semi-major axis that is not large enough to experience tidal torquing from the galaxy ($a \sim 2000$ au; Duncan et al., 1987) and are on non-circular orbits (Gladman et al., 2008). These TNOs are detached from the dynamics of the planets (distinguishing them from scattering TNOs on large orbits) and the galaxy, but are unlikely to have formed in situ due to their eccentric orbits. There has been no consensus on a formation mechanism for these isolated TNOs, but options include an additional planet in the Solar System (e.g.

---

[2] point of closest approach to the Sun

Gladman et al., 2002; Brown et al., 2004; Gomes et al., 2006; Soares & Gomes, 2013), the effects of passing stars (e.g. Ida et al., 2000; Kenyon & Bromley, 2004; Morbidelli & Levison, 2004; Kaib et al., 2011b; Soares & Gomes, 2013; Brasser & Schwamb, 2015) and rogue planets ejected from the inner Solar System (e.g. Thommes et al., 2002; Gladman & Chan, 2006).

1.3 Size and H Distributions

The distribution of sizes of TNOs arises from the accretion physics and the collision history of the TNO population. Measuring the size distribution of TNO populations can provide constraints on the conditions and history of these processes in the Solar System. Accretion is the process of agglomerating small particles into larger bodies and collision processes break larger bodies into smaller fragments; both processes have the end result of more objects at small sizes and each has been described by a single power-law distribution in diameter, D:

$$\frac{\mathrm{d}N}{\mathrm{d}D} \propto D^{-q} \tag{1.2}$$

with the power-law index, q, set by the conditions of the accretion or collision process (e.g. see Dohnanyi, 1969; Davis & Farinella, 1997; Schlichting et al., 2013).

A scaling of this functional form is easy to understand intuitively. Consider a simplified case of collisional disruption of a body of mass M_0, with constant density ρ, and radius r:

$$M_0 = \frac{4}{3}\pi \mathrm{r}^3\,\rho \tag{1.3}$$

If this body is broken into N smaller pieces of equal size r, we can express the mass and number as follows:

$$M_0 = M_f = \sum_{i=1}^{N} \frac{4}{3}\pi \mathrm{r}^3\,\rho \tag{1.4}$$

$$M_0 = M_f = \mathrm{N}\,\frac{4}{3}\pi \mathrm{r}^3\,\rho \tag{1.5}$$

Which gives:

$$\mathrm{N} \propto r^{-3} \tag{1.6}$$

And therefore:

$$\frac{\mathrm{d}N}{\mathrm{d}r} \propto r^{-4} \tag{1.7}$$

Equation 1.7 exhibits the same functional form as Equation 1.2, with a size distribution q coefficient of 4. Accretion processes can be analogously thought of as building up a massive body from many smaller bodies, resulting in the same functional form. These two thought experiments intuitively demonstrate why the size distribution has the form in Equation 1.2.

The exact mechanisms for the formation of TNOs remains an open question. Two competing theories exist: that TNOs formed bottom-up from the accretion of small-sized particles (e.g. see Kenyon & Luu, 1998; **?**) and that TNOs formed directly as large objects (e.g. see Morbidelli et al., 2009). These formation processes shape the large-size end of the size-distribution. Collisional grinding shapes the small-size end of size-distribution, where collisions have dominated over formation mechanisms. Collisions are not generally disruptive, as in the above thought experiment, but rather a cascade of collisions is what shapes the form of the small-end size-distribution. In either regime, the exact value of the size distribution exponent q will depend on the specific physics and conditions for forming initial bodies in the accretion regime and will depend on the physical binding properties of TNOs and timescales in the collisional regime (e.g. see Dohnanyi, 1969; Davis & Farinella, 1997; Kenyon & Luu, 1998; O'Brien & Greenberg, 2005; Pan & Sari, 2005; Schlichting et al., 2013). It has been shown that a population in collisional equilibrium has q near 3.5 (Dohnanyi, 1969; O'Brien & Greenberg, 2005), depending on some factors such as the tensile strength of the objects.

TNOs are generally too small and far away to be resolved in direct imaging and thus their sizes cannot be measured directly. Instead, we measure the brightness of the object, quantified by its magnitude, to access information about the object's size. As TNOs are not emissive at visible wavelengths, their magnitude depends on three things: their size, distance, and the fraction of light reflected by the surface (the albedo). The absolute magnitude, H, is the magnitude an object would have if it were one au away from the Sun as viewed by an observer on the surface of the Sun. To quantify H, we first examine the magnitude, m, relative to the Sun. The magnitude is determined by its flux (as in Equation 1.1), which depends on the object's radius R, albedo A, phase function ϕ with phase angle α, distance from the Sun r and distance from the Earth Δ. Equation 1.8 is a re-expression of Equation 1.1, with the fluxes re-expressed and a constant that sets the size scale to km and the distance scale to

AU.

$$m = m_{\odot} - 2.5 \cdot \log_{10}\left(\frac{AR_{km}^2\phi(\alpha)}{2.25\times 10^{16} r_{AU}^2 \Delta_{AU}^2}\right) \tag{1.8}$$

H is found by setting $r = \Delta = 1$ and $\phi = 1$:

$$H = m_{\odot} - 2.5 \cdot \log_{10}\left(\frac{AR_{km}^2}{2.25\times 10^{16}}\right) \tag{1.9}$$

Measuring the H-distribution acts as a proxy for measuring the size distribution - H is directly mappable to size, requiring only the albedo of the object. The above expression (Equation 1.2) for the size distribution can be converted to H and then takes on the form of an exponential distribution in H:

$$\frac{\mathrm{d}N}{\mathrm{d}H} \propto 10^{\alpha H} \tag{1.10}$$

where α arises from the accretion and collision physics and can be converted directly to q with $q = (5\alpha + 1)$. TNO studies seek to measure the H-distribution in order to constrain the accretion and collision history of the TNO populations.

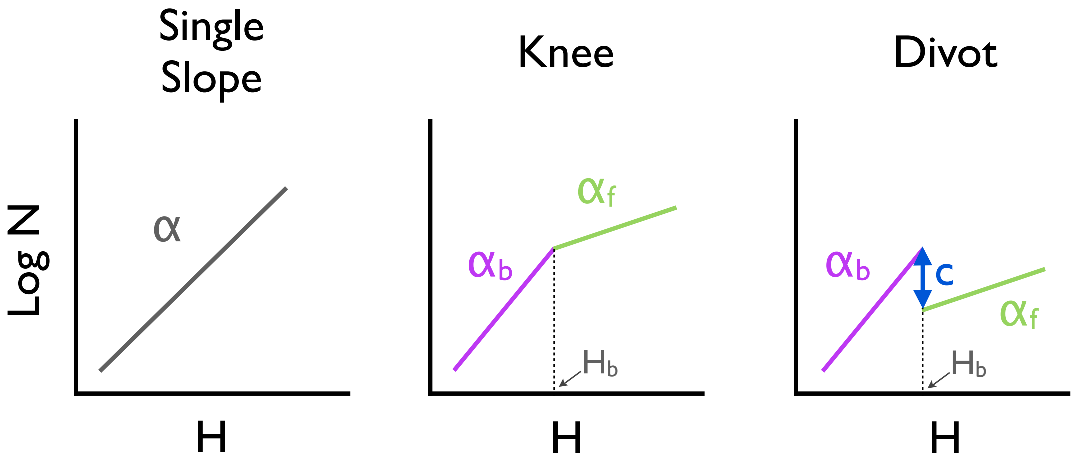

Figure 1.3: A schematic of the differential forms of the three H-distribution cases: single slope, knee, and divot. A single slope is parameterized by a logarithmic slope α. A knee is parameterized by a bright slope α_b, a faint slope α_f, and a break location H_b. A divot is parameterized as a knee, but with a contrast c (≥ 1), which is the ratio of the differential number of objects right before the divot to the number just after the divot, located at H_b. This figure appears in Shankman (2012) and Shankman et al. (2016) and is reproduced with permission.

In the TNO region, at large sizes, the H-magnitude distribution has been well measured with a steep single slope (α) for various dynamical sub-poplations of TNOs (Gladman & Kavelaars 1997; Gladman et al. 2001; Bernstein et al. 2004; Fraser & Kavelaars 2008; Fuentes & Holman 2008). At smaller sizes, the H-distribution has been shown to transition to a shallower slope in the dynamically "hot" population; this transition can be interpreted as the point where collisional grinding dominates the size distribution, producing a different slope. Measuring the slope past this transition may help constrain timescale for the migration of Neptune, as this disruptive event would increase the volume TNOs occupy, thereby shutting off collisional evolution and freezing in the size distribution. The form of the transition has been modelled as a sharp knee, smooth rollover, and as a divot (e.g. see Figure 1.3, Gladman et al. 2012; Shankman et al. 2013; Adams et al. 2014; Fraser et al. 2014; Alexandersen et al. 2016, Shankman et al. 2016).

There have been several measurements of the H-distribution in the hot TNO populations. The hot populations include the Trojans, the mean-motion resonances (e.g. Plutinos), the hot classicals, and the scattering TNOs. The scattering TNO population is the focus of the H-distribution analyses in this work as they come closer to the Sun, allowing for the detection of smaller TNOs and thus allowing for a better constraint on the formation conditions as compared to what can be achieved by studying the "cold" populations. Dynamical models have proposed that the hot TNOs formed closer to the Sun and were later scattered, during a giant planet instability phase, to their present orbits (Gomes, 2003; Levison et al., 2008; Batygin & Brown, 2010; Nesvorný, 2015). Assuming they formed together, the hot: populations are imbued with the same H-distribution. This H-distribution that formed pre-instability was then "frozen-in" as the number densities in the outer Solar System make collisions improbable. Thus by measuring the H-distribution for one of the hot populations, the formation conditions of all of the populations can be constrained.

The main asteroid belt, between Mars and Jupiter, provides an analogous (but visually resolvable) set of planetesimals to compare with TNOs. Figure 1.4 plots a parametric model of the main asteroid belt size distribution. There is an abundance of structure, with numerous transitions, in the size distribution of the main belt asteroids, resulting from the complex processes of formation and collisional evolution as well as a mixing of populations. It is reasonable to expect that the TNO size distributions are complex, with many transitions that are being revealed as we probe to smaller and smaller sizes. The cratering records of Pluto recently revealed by the New Horizons spacecraft hint at this, showing transitions in the impactor distribution at sizes that are presently unobservable in the TNO population, indicating that there are numerous transitions in the TNO size distribution. The challenge now is to constrain the location and form of these transitions in the observable size ranges of TNO populations.

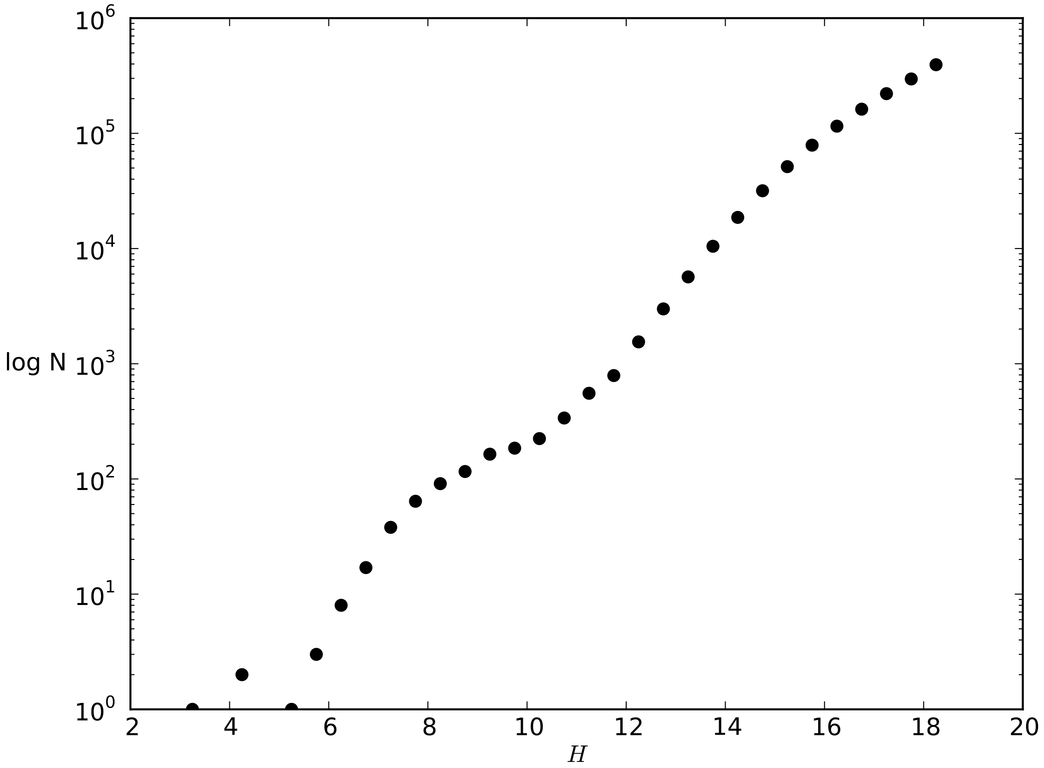

Figure 1.4: Here the H-distribution of the main asteroid belt based on the Jedicke et al. (2002) parametric model with data from Bottke et al. (2005) is plotted. The structure of the distribution is complex, with many features. TNO size distributions are likely to be similarly complex. This figure appears in Shankman (2012) and is reproduced with permission.

1.4 On the Existence of an Additional Massive Planet in the Distant Solar System

There has been a flurry of recent press and scientific activity around the question of the existence of an additional planet in the far outer Solar System. Trujillo & Sheppard (2014) first noted that the detached TNOs ($<$ 20 known objects) appear to cluster near 0° in argument of pericentre (ω), which is unexpected as any observing bias in ω should be symmetric about 0° and 180°. An additional perturber was invoked, but not demonstrated, in order to potentially explain how TNOs could be driven to cluster near $\omega = 0°$. Batygin & Brown (2016a) drew greater attention to the idea of an extra planet with the claim of a dynamical pathway showing that a super-Earth-mass planet in the distant Solar System could explain the large-a TNO orbits. The existence of an additional planet in the outer Solar System would have a profound impact on our understanding of the formation and evolution of the Solar System. The theories of the outer Solar System's formation, the way we classify TNO subpopulations and existing dynamical models would all require an overhaul in the presence of such a planet. In particular, the scattering and detached TNOs would both be strongly affected by the gravity of such a planet, requiring a new classification for these TNOs. This would have impacts on existing analyses of the bulk properties of these populations, as populations that are currently considered dynamically separate would mix in the presence of the proposed planet. Exploring the implications and undperinning arguments for the additional planet theory is important not only for the public interest the theory has generated, but also because the existence of such a planet would reshape the field of study of the most distant TNOs.

1.5 Methods

The subsequent chapters will detail the specifics of the methods used in each study. Two main techniques are used in this work: survey simulator and n-body integrator. An overview of these two methods is provided here as context for the following chapters. The statistical methods used in this work are described in Section 2.4.5.

1.5.1 Survey Simulator

For a meaningful analysis, the biases in any dataset must be accounted for. It is not possible to take a TNO survey and "debias" the survey to reveal the real intrinsic distributions of TNOs in the Solar System. Simply, one can never know what was not seen. To account for the biases, we conduct simulated surveys that forward model the measured biases of a survey onto a model intrinsic population. This approach is simply referred to as using a survey simulator, with the simulator developed by Jones et al. (2006), Kavelaars et al. (2009), Petit et al. (2011), and Alexandersen et al. (2016).

The survey simulator takes as input the characteristics of the real survey that was performed, including the factors that contribute to various observing biases. Each survey is broken into segments (blocks) that point in specific parts of the sky (pointings) with limits on how faint they were able to observe (limiting magnitude).

A number of other measured parameters are reported, including estimates of the efficiency for tracking discovered TNOs, the limiting rate of motion on sky for tracked TNOs and the light filter the survey was conducted in. All of these parameters are provided for the three surveys used in this work.

At its core, the survey simulator computes one thing: would a given TNO have been detectable by one of the surveys being simulated? To use the simulator, one specifies a TNO orbit, the position of the TNO on its orbit, an H-magnitude for the TNO, and any conversions between observing filters (if necessary). The simulator then computes if the TNO would be at a sky position that was observed, if the TNO would be bright enough to be observed by the appropriate block, if the TNO would be moving at a rate that allows for tracking of the TNO, and then applies observing effects (such as noise in measured magnitude, tracking fractions for the detected block). The simulator then reports out whether or not TNO would have been detected by the survey.

This tool can be used to achieve various science goals. In Chapters 2 and 3 the survey simulator is used to compare the detected TNO orbital distributions to model distributions for candidate H-mag distributions to constrain the possible H-mag distributions of a population. In Chapter 4 the survey simulator is used to explore the observable effects of an additional massive planet by comparison with a detected sample. Finally, in Chapter 6 the survey simulator is used to explore the structure of the observing biases for detecting large-a TNOs.

1.5.2 N-body Integrations

To study the orbital behaviour over time of an object, an n-body integrator is used. N-body integrators numerically approximate the solutions to the integrals for the equations of motion for n gravitationally interacting particles. This work primarily uses the MERCURY6 (Chambers, 1999) suite for its ease of use, wide adoption in the Solar System Dynamics community, and ability to approximate close encounters between bodies. In these simulations, the Sun, 4 gas giant planets, and in some cases an additional planet are added as massive objects. TNOs are added as massless "test particles" as their motion is dominated by interactions with the giant planets; their masses are comparatively negligible and the distances between TNOs are vast. Adding the TNOs as massless test particles dramatically reduces the computation time and allows for simulations that model more TNOs. N-body simulations are used in Chapter 4 to explore the effects of an additional massive planet on the formation of the outer Solar System. Chapter 5 uses n-body simulations to explore the effects of gravitational interactions from an additional massive planet on the detached TNOs.

1.6 Thesis Outline

In Chapter 2, I measure the form of the scattering TNO H-distribution from the detections of CFEPS, Alexandersen et al. (2016), and the first quarter of OSSOS. I parameterise the H-distribution to examine single-slope, knee, and divot forms of the H-distribution. I then discuss the results in the context of the other measured hot TNO H-distribtuions. In Chapter 3, I present an examination of the scattering TNO H-distribution with the complete OSSOS sample in the framework described in Chapter 2.

Chapter 4 examines the effects of an additional massive planet on the formation of the TNO orbit distributions. An N-body simulation is performed for the age of the Solar System with the planets in their current configurations, an additional massive planet, and an initial disk of planetesimals. The detectability of the signatures imposed by the additional planet are then tested via a survey simulator. Mass estimates are determined for the scattering and detached populations required to explain the detected sample in the case that an additional massive planet shaped the distant TNO orbit distribution.

Chapter 5 explores the consequences of a distant massive planet on the large-a TNOs that were used to infer its existence. Via N-body simulation, I model the orbital behaviour of the known large-a TNOs in the presence of the proposed additional planet. I examine the ability of the proposed planet to reproduce the observed signature that led to the theory. The mass required to expect to have detected the known TNOs in this scenario is also estimated.

Chapter 6 explores the evidence for the argument of clustering of TNO orbits that led to the additional planet hypothesis. Via survey simulation, I measure the biases of OSSOS for detecting TNOs at such large distances and demonstrate the potential impact of these biases on the observed TNO sample. I then examine the OSSOS dataset, which provides an independent and comparably sized sample, for evidence of clustering. The full dataset of known TNOs, with the inclusion of OSSOS, is then examined for evidence of clustering.

Finally, in Chapter 7 I summarize my findings and offer concluding remarks.

Chapter 2

OSSOS. II. A Sharp Transition in the Absolute Magnitude Distribution of the Kuiper Belt's Scattering Population

Published as: C. Shankman, JJ. Kavelaars, B. J. Gladman, M. Alexandersen, N. Kaib, J.-M. Petit, M. T. Bannister, Y.-T. Chen, S. Gwyn, M. Jakubik, and K. Volk 2016 *AJ* 151 31

Available online here: http://iopscience.iop.org/article/10.3847/0004-6256/151/2/31/meta

2.1 Abstract

We measure the absolute magnitude, H, distribution, $dN(H) \propto 10^{\alpha H}$ of the scattering Trans-Neptunian Objects (TNOs) as a proxy for their size-frequency distribution. We show that the H-distribution of the scattering TNOs is not consistent with a single-slope distribution, but must transition around $H_g \sim 9$ to either a knee with a shallow slope or to a divot, which is a differential drop followed by second exponential distribution. Our analysis is based on a sample of 22 scattering TNOs drawn from three different TNO surveys — the Canada-France Ecliptic Plane Survey (CFEPS, Petit et al., 2011), Alexandersen et al. (2016), and the Outer Solar System Origins Survey (OSSOS, Bannister et al., 2016), all of which provide well characterized detection thresholds — combined with a cosmogonic model for the formation of the

scattering TNO population. Our measured absolute magnitude distribution result is independent of the choice of cosmogonic model. Based on our analysis, we estimate that number of scattering TNOs is (2.4-8.3)$\times 10^5$ for $H_r < 12$. A divot H-distribution is seen in a variety of formation scenarios and may explain several puzzles in Kuiper Belt science. We find that a divot H-distribution simultaneously explains the observed scattering TNO, Neptune Trojan, Plutino, and Centaur H-distributions while simultaneously predicting a large enough scattering TNO population to act as the sole supply of the Jupiter-Family Comets.

2.2 Introduction

There are many important unanswered questions about the formation of the Solar System. For example: What were the conditions of the initial accretion disk and how long did the planetessimals grind collisionally? These questions cannot be answered by direct observation of the phenomena. Instead, using signatures implanted in its small-body populations, we infer the formation history from the present state of the Solar System. The size-frequency distribution of small-body populations is shaped by the formation physics (large-sized objects) and the collisional history (small-size objects) of the population, and is thus a key signature of the history of the population (for a review see Leinhardt et al. 2008). Here we study the absolute magnitude distribution of the scattering Trans-Neptunian Objects (TNOs), examining an important piece of the complex TNO puzzle.

TNOs are too small (unresolved), cold, and distant (Stansberry et al., 2008) to allow for direct measurement of their sizes; instead, measurements of the luminosity function have been used to probe the size-frequency distribution of TNOs (see Petit et al. 2008 for a review). Steep slopes of 0.8-1.2 have been measured for the luminosity functions of bright objects over spans of a few magnitudes (Gladman & Kavelaars 1997; Gladman et al. 2001; Bernstein et al. 2004; Fraser & Kavelaars 2008; Fuentes & Holman 2008) and these steep slopes have been shown to break in the dynamically "hot" populations at smaller size (Bernstein et al. 2004; Fraser & Kavelaars 2008; Fuentes & Holman 2008). While measuring the luminosity function has found strong features, this approach introduces uncertainties for assumptions of the size, albedo and radial distributions, which are often not well constrained in sky surveys for TNO discovery that are sensitive to faint sources.

A more direct approach to probe the underlying size-frequency distribution is to measure the absolute magnitude distribution, or H-distribution. Measuring the H-distribution removes observation distance dependencies and only requires an albedo measurement to be converted into size. The H-distribution approach has been used to probe the size-frequency distribution of the TNO populations (e.g. see Gladman et al. 2012; Shankman et al. 2013; Adams et al. 2014; Fraser et al. 2014; Alexandersen et al. 2016) and here we use the H-distribution to probe the size-frequency distribution of the scattering TNOs.

The scattering TNOs are the best Trans-Neptunian population to use to measure the small-size H or size distribution. Because of their interactions with the giant planets, scattering TNOs come in the closest to the Sun of any TNO sub-population. As TNOs are discovered in reflected light and in flux-limited surveys, the best way to detect smaller objects is to have them be closer-in. Because of their close distances (d down to 20-30 AU), a 4m class telescope can detect scattering TNOs down to $H_r \sim 12$, which is past the observed break in the TNO hot populations seen at $H_r \sim 8$ (Shankman et al. 2013; Fraser et al. 2014). The scattering TNOs have smaller pericenters allowing flux-limited surveys to probe to small sizes in this population, providing an accessible sample of TNOs that cross the size range where the size-distribution appears to transition from steep (large objects) to shallow (small objects) slopes. Here we present a measure of the H-distribution, a proxy for the size-frequency distribution, of the largest bias-understood sample of scattering TNOs crossing the transition (see Section 2.3).

The measured H-distribution of the scattering TNOs acts as a useful proxy for many other dynamically hot populations in the outer Solar System, and even beyond the Kuiper Belt, as these populations may share a common evolution. Several dynamical models posit that many or all TNOs formed closer-in to the Sun and were later scattered out to their current orbits (Gomes, 2003; Levison et al., 2008; Batygin & Brown, 2010; Nesvorný, 2015) during an instability phase with the giant planets. This would have depleted all Trojan populations of the giant planets and thus all current Neptune Trojans must have been captured from the scattering TNOs post-instability. The Neptune Trojan population is of particular interest for its observed lack of small-sized objects (Sheppard & Trujillo, 2010), which is incompatible with a steep single-slope size-distribution. These hot populations would share a common "frozen-in" size-frequency distribution, formed pre-instability, as the number densities in the outer Solar System make collisions improbable. The scattering TNOs present an opportunity to measure the small-size end of the frozen-in TNO size-frequency distribution which may be shared by the Neptune Trojans and other TNO hot populations.

To date there have been three measurements of the scattering TNO luminosity function or H-distribution. (1) With a scattering TNO sample of 4, Trujillo et al. (2000) do not measure the slope of the size-distribution directly, but find that slopes of $\alpha = 0.4$ and 0.6 are not rejectable for their sample. (2) Shankman et al. (2013), with a sample of 11 scattering TNOs, reject a single slope H-distribution and require a break in the H-distribution around $H_g = 9$ (diameter, $D \sim 100$ km for 5% albedo), confirming the need for a transition in the TNO hot populations. Shankman et al. (2013) argue in favor of a divot H-distribution, finding that the population of scattering TNOs with a divot H-distribution is numerous enough to be the source for the Jupiter Family Comets (JFCs). (3) Adams et al. (2014), using a sample of 23 objects that includes scattering TNOs and the so-called Hot Classicals, measure the pre-break (large size) slope, finding a steep slope of $\alpha = 1.05$. The Adams et al. (2014) sample includes multiple dynamical TNO populations and is thus not directly comparable to this analysis which only measures the scattering TNO population. Adams et al. (2014) compare the scattering TNO H-distribution to their measured Centaur slope of $\alpha = 0.42$, as the Centaurs could be supplied by the scattering TNOs. The Adams et al. (2014) Centaur sample of 7 objects only contains one object that is brighter than the break magnitude in the hot populations, and thus they measure the faint slope with no lever arm on the form of the transition at the break. In this work we measure the H-distribution of the scattering TNOs, extending the sample and analysis used in Shankman et al. (2013); this work provides stronger and more robust constraints on the form of the scattering TNO H-distribution.

In Section 2.3 we discuss our observations. In Section 2.4 we discuss the dynamical model used, our survey simulator approach, and our statistical tests. In Section 2.5 we present our results. In Section 2.6 we consider the implications of our results for other small-body populations in the outer Solar System and finally in Section 2.7 we provide our concluding remarks.

2.3 Observations

Observing and characterizing TNOs is difficult. TNOs are distant, faint, and move relative to the background stellar field. Their sky density is not uniform and they are detected in reflected light over a small range of phase angles, often exhibiting a surge in brightness near opposition (Benecchi & Sheppard, 2013). The choice of pointing direction, the efficiency of tracking objects (necessary for determining orbits), and survey magnitude limits add complexity to the already difficult problem of interpreting the observed samples. To be properly identified, a TNO must be bright enough to be detected and then must be linked in follow-up observations to establish an orbit so that the object can be classified into a TNO sub-category. To take a sample of observed TNOs and determine the intrinsic population requires detailed documentation of the biases inherent in the observation process (e.g. see Kavelaars et al. 2008). With detailed documentation of the biases, the observations can then be "debiased" to infer the model from the sample or, as we do here, models of the intrinsic population can be forward biased and judged in comparison to the detected sample. To properly combine different surveys, the biases must be well measured for all surveys. We emphasize that there are a variety of factors that result in the biased sample, and each must be carefully measured, or characterized.

Here we present our analysis on a sample of 22 scattering TNOs resulting from combining the observed samples of the Canada-France Ecliptic Plane Survey (CFEPS) (Petit et al., 2011; Kavelaars et al., 2011), Alexandersen et al. (2016), and the first quarter results of the Outer Solar System Origins Survey (OSSOS) (Bannister et al., 2016). These three surveys were performed and characterized with similar approaches, allowing the samples to be combined in a straightforward manner. Details on the observing approach and orbital classification are given in the individual survey description papers referenced above. From each survey we select the scattering TNOs, as classified by the classification scheme in Gladman et al. (2008): a non-resonant TNO whose orbital parameters vary by Δa of at least 1.5 AU in a 10 Myr integration is considered to be a scattering TNO. As the objects in our surveys are reported in two different bands, g and r, we adopt a $g-r$ color for the analysis. As we show in Section 2.6.1, the value of $g-r$ does not cause a material change in our results. The observed and derived properties of the 22 scattering TNOs used in this analysis are reported in Table 1.

CFEPS obtained characterized observations between 2003 and 2007, covering 321 deg^2 of sky around the ecliptic to g-band limits of 23.5 (Petit et al., 2011). They provided a catalog of 169 dynamically classified TNOs, 9 of which are scattering, and a set of tables that provide detailed characterization of those detections. The initial CFEPS catalog was supplemented by a high ecliptic latitude survey carried out in 2007 and 2008 that covered 470 deg^2, extended up to 65° ecliptic latitude and found

4 scattering TNOs (Kavelaars et al., 2011). The extended survey's detection and tracking characterization is provided in Petit et al. (2015). This combined data set of 13 scattering TNOs is referred to as the CFEPS sample.

Alexandersen et al. (2016) performed a 32 deg^2 survey to a limiting r-band magnitude of 24.6, finding 77 TNOs. They found two temporary Trojans, one for Uranus and one for Neptune. Using the SWIFT package (Levison & Duncan, 1994) for orbital integrations, they found that both objects ceased to be co-orbitals within $\sim 1\,\text{Myr}$, after which they both rejoin the scattering population (Alexandersen et al. 2013, Alexandersen et al. 2016). Both objects satisfy the scattering classification criterion as above. The survey analysis from Alexandersen et al. (2016) followed the same careful characterization process as used in CFEPS. The characterization information for this survey can be found in Alexandersen et al. (2016)

In the northern hemisphere fall of 2013, OSSOS searched 42 square degrees of sky, detecting 86 TNOs brighter than the survey's limiting r' magnitudes of 24.04 and 24.40 (for OSSOS's E and O blocks respectively). Of those, 7 were found to be on scattering orbits and are included in the analysis presented here. For the OSSOS and Alexandersen et al. (2016) surveys (as distinct from the CFEPS sample) the orbital tracking observations were more frequent during the discovery year, enabling orbital classification after only two years of observing as compared to the four to five years needed for the more sparsely observed CFEPS targets. The complete details of the OSSOS characterization can be found in Bannister et al. (2016).

Our observed sample of 22 scattering TNOs down to H_r of 12 is the largest sample of scattering TNOs from characterized surveys, and the only sample that extends beyond the confirmed break in the H-distribution. This is the best sample available to probe the form of the H-distribution at and beyond the transition in the size-frequency distribution.

2.4 Methods

Our observationally biased sample of scattering TNOs can be used to explore the characteristics of the intrinsic scattering population via a model comparison. Through the process of characterization, each input survey provides a careful estimate of the detection and tracking bias that is present in the detected sample. Rather than debias our observed sample into an estimate of the intrinsic population, we forward bias intrinsic orbital models of the scattering TNOs and compare them with the observed

Designation **Internal**	**Designation** **MPC**	**a** **(AU)**	**q** **(AU)**	**i** **(deg)**	**d** **(AU)**	**m**	**H**	**Filter**	**Survey**
L4k09	2004 KV18	30.19	24.6	13.59	26.63	23.64	9.33	g	CFEPS
L4m01	2004 MW8	33.47	22.33	8.21	31.36	23.75	8.75	g	CFEPS
L4p07	2004 PY117	39.95	28.73	23.55	29.59	22.41	7.67	g	CFEPS
L3q01	2003 QW113	51.05	26.31	6.92	38.17	24.0	8.16	g	CFEPS
L7a03	2006 BS284	59.61	33.41	4.58	46.99	23.84	7.12	g	CFEPS
L4v04	2004 VG131	64.1	31.64	13.64	31.85	24.14	9.09	g	CFEPS
L4v11	2004 VH131	60.04	22.26	11.97	26.76	24.19	9.94	g	CFEPS
L4v15	2004 VM131	68.68	20.61	14.03	22.97	22.0	8.96	g	CFEPS
L3h08	2003 HB57	159.68	38.1	15.5	38.45	24.29	8.36	g	CFEPS
HL8a1	2008 AU138	32.39	20.26	42.83	44.52	22.93	6.29	r	CFEPS
HL8n1/Drac	2008 KV42	41.53	21.12	103.45	31.85	23.73	8.52	r	CFEPS
HL7j2	2007 LH38	133.9	36.8	34.2	37.38	23.37	7.5	r	CFEPS
ms9	2009 MS9	348.81	11.0	68.02	12.87	21.13	9.57	r	CFEPS
mal01	2011 QF99	19.09	15.72	10.81	20.3	22.57	9.57	r	A14
mah01	2012 UW177	30.06	22.29	53.89	22.43	24.2	10.65	r	A14
o3o01	2013 JC64	22.14	13.76	32.02	13.77	23.39	11.95	r	OSSOS
o3e01	2002 GG166	34.42	14.12	7.71	23.29	21.5	7.73	r	OSSOS
o3o36	2013 JQ64	48.79	22.38	34.88	57.34	23.73	6.09	r	OSSOS
o3o16	2013 JP64	57.44	32.35	13.7	35.68	23.92	8.34	r	OSSOS
o3o17	2013 JR64	77.56	35.64	10.46	35.81	24.31	8.71	r	OSSOS
o3e11	2013 GZ136	86.74	33.89	18.36	36.85	23.6	7.86	r	OSSOS
o3o14	2013 JO64	143.35	35.13	8.58	35.46	23.54	8.0	r	OSSOS

Table 2.1: The combined scattering TNO samples from CFEPS, OSSOS and Alexandersen et al. (2016). The magnitude and H-magnitude given are both in the listed filter.

sample. We forward bias a model of scattering TNOs using our Survey Simulator (Jones et al., 2006; Petit et al., 2011). The resulting biased model of the intrinsic population is then tested by comparison to the detected sample. Each model is the combination of an orbital model paired with an H-magnitude distribution in a specific filter, a color conversion distribution, and light curve effects. We test the joint model by comparing orbital parameters (semi-major axis, inclination, pericenter) and observed parameters (H-mag, distance at detection, magnitude at detection) of the simulated detections against our observed sample via the Anderson-Darling (AD) test (see Section 2.4.5). We show in Section 2.6.1 that the rejection of this combined model constitutes a rejection of the H-magnitude distribution and we thus are able to determine the H-magnitude distribution of the scattering TNOs. This approach introduces orbital and color model dependencies. We show in Section 2.6.1 that our analysis is not sensitive to the choice of orbital model or color distribution.

All tools required to perform this analysis are available at:
http://dx.doi.org/10.5281/zenodo.31297

2.4.1 Survey Simulator

The Survey Simulator determines whether a given object would have been detected and tracked by one of our surveys. The simulator is given a list of survey pointings and the detection efficiency for each pointing in order to perform a simulated survey. A randomly selected model object, with an assigned H-magnitude and color, is tested for detection by the survey simulator. The simulator first checks that the object is bright enough to have been seen in any of our surveys' fields, then checks that the object was in a particular field, and that it was bright enough to be detected in that field. Based on a model object's simulator-observed magnitude and the field's detection and tracking efficiencies, model objects are assessed for "observability". The survey simulator reports the orbital parameters, the specified H-magnitude, and color conversion for all orbital model objects determined to have been "detected" and "tracked". The object's "observed" magnitude, and corresponding H-magnitude, which includes accounting for measurement uncertainties, are also reported. Using the Survey Simulator, we produce a statistically large model sample that has been biased in a way that matches the biases present in our observed survey sample. This large Survey Simulator produced model sample is then compared directly to the detected sample.

2.4.2 Models

In order to carry out a simulated survey, one requires an orbital model for the objects being "observed". For our model we select out the scattering TNOs from a modified version of the Kaib et al. (2011b, KRQ11) orbital model of the TNO population. The KRQ11 model (see Figure 2.1) is the end-state of a dynamical simulation of the evolution of the Solar System that includes the gravitational effects of the giant planets, stellar passages and galactic tides. The simulation begins with an initial disk of massless test particles between semi-major axis $a = 4$ AU and $a = 40$ AU following a surface density proportional to $a^{-3/2}$, eccentricities, $e < 0.01$ and inclinations, i, drawn from $\sin(i)$ times a gaussian, as introduced by Brown (2001). The giant planets are placed on their present-day orbits (see Section 2.6.1 for a discussion on the effects of the planet configuration and how it does not affect our result), the stellar neighbourhood is modeled assuming the local stellar density, and the effects of torques from galactic tides are added (for more detail, see Kaib et al. 2011b). This system is then integrated forward in time for 4.5 Gyr, resulting in a model for the current state of bodies in the outer Solar System. The resulting orbital distribution is then joined with a candidate H-distribution, and a TNO color distribution derived from Petit et al. (2011). This joint orbit, H-distribution and color distribution model forms the input for the Survey Simulator.

Shankman et al. (2013) demonstrate that the inclinations in KRQ11 are too low to match the observed scattering TNOs; the model's assumed initial inclination distribution is too "cold". A model with a "hotter" initial i distribution (with gaussian width $\sigma = 12°$) was created and dynamically evolved forward for the age of the Solar System. We continue to use this modified KRQ11 as our orbital model in this analysis. In Section 2.6.1 we discuss the effect that the choice of model has on our analysis.

We use the modified KRQ11 orbital model as a representation of the current-day population of scattering objects in the Solar System in order to perform a simulated survey of scattering TNOs. We select out the scattering TNOs from the orbital model (i.e. those with $\Delta a \geq 1.5$ AU in 10 Myr) in plausibly observable ranges ($a < 1000$ AU, pericenter $q < 200$ AU), which results in a relatively small number of objects. To account for the finite size of the model, we draw objects from the model and add a small random offset to some of the orbital parameters. The scattering TNOs don't have specific orbital phase space constraints (unlike the resonances which are

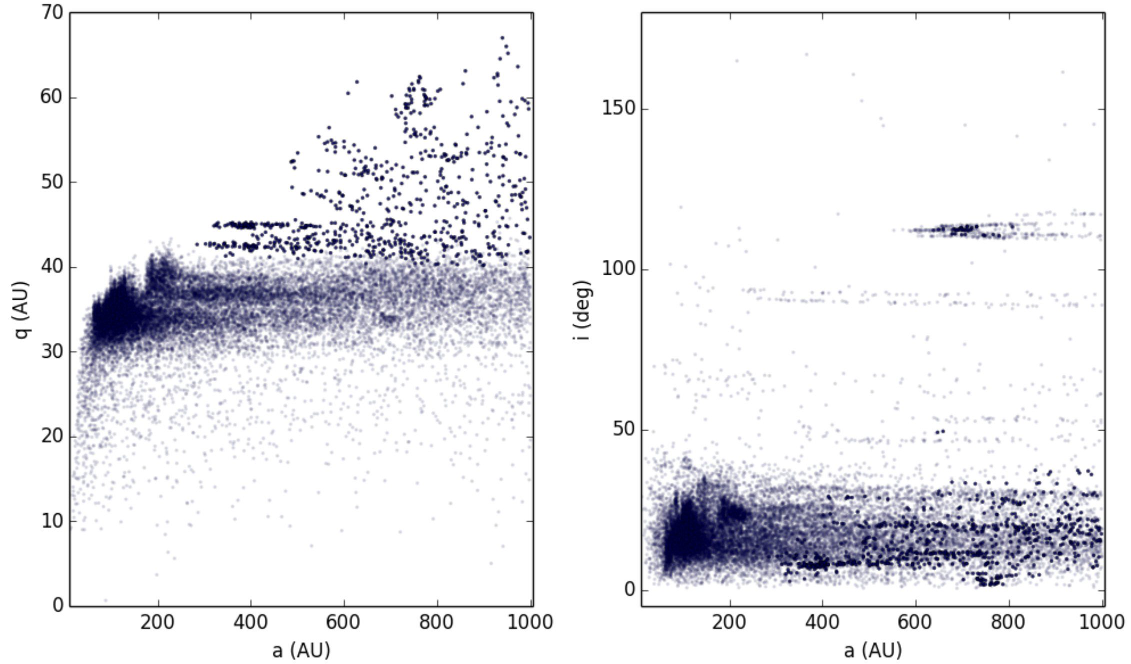

Figure 2.1: Scatter plots of pericenter q vs a and i vs a for the modified Kaib et al. (2011b) orbital model, sliced as $a < 1000$ AU, and $q < 200$ AU. Each point represents one object in the simulation. Points have transparency of 0.1 to highlight densities in the model. Some points appear solidly dark as they were cloned in place at the end-state of the simulation to balance that they were not cloned at any other point in the simulation (for details see Kaib et al. 2011b).

constrained in a, e, and resonant angles) and thus we can better sample the space the model occupies by slightly adding this small random offset. This extends the model beyond the set of TNOs produced in the original run (~29k for above a, q slices) that was necessarily limited by computation times. We resample a, q, and i by randomly adding up to ± 10 %, ± 10 %, and ± 1°, respectively, to the model-drawn values. We also randomize the longitude of the ascending node, the argument of pericenter and the mean anomaly of each model object. This modified KRQ11 orbital model, resampled to increase its utility, is used as the input orbital model for the scattering TNOs.

2.4.3 H-magnitude Distribution

A variety of forms have been used to try to match the observed magnitude or H-magnitude distributions of various TNO populations. Single slopes (e.g. Jewitt et al.

1998; Gladman et al. 2001; Fraser & Kavelaars 2008; Gladman et al. 2012; Adams et al. 2014), knees (Fuentes & Holman 2008; Fraser & Kavelaars 2009; Fraser et al. 2014), knees with smooth rollovers (Bernstein et al. 2004), and divots (Shankman et al. 2013; Alexandersen et al. 2016) have all been proposed. Here we present a generalized form of the H-magnitude distribution for testing, which in limiting cases becomes either a knee or a single-slope.

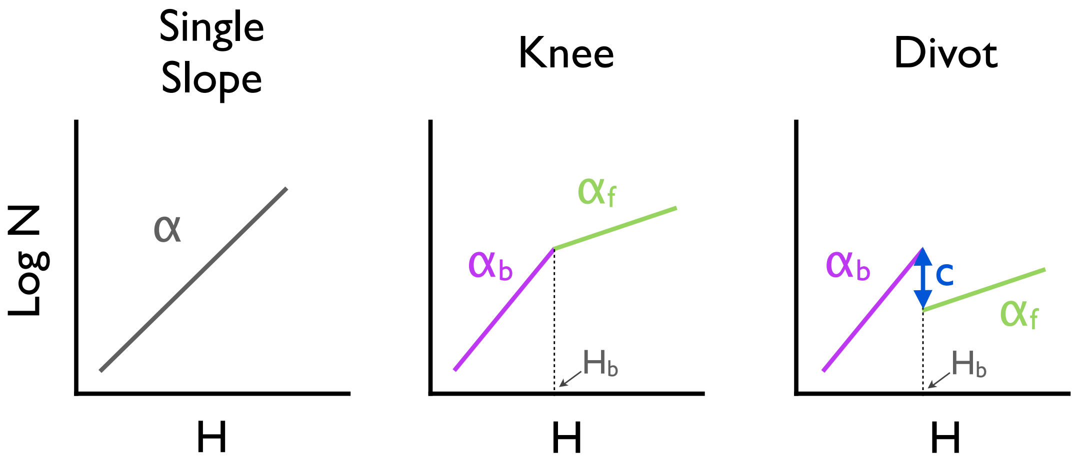

Figure 2.2: A schematic of the differential forms of the three H-distribution cases we test: single slope, knee, and divot. A single slope is parameterized by a logarithmic slope α. A knee is parameterized by a bright slope α_b, a faint slope α_f, and a break location H_b. A divot is parameterized as a knee, but with a contrast c (≥ 1), which is the ratio of the differential number of objects right before the divot to the number just after the divot, located at H_b.

We characterize the H-distribution by four parameters: a bright (large-size) slope, α_b, a faint (small-size) slope, α_f, a break absolute magnitude, H_b, and a contrast, c, that is the ratio of the differential frequency of objects just bright of the break to those just faint of the break. Depending on the parameters, our H-distribution takes one of three forms: single-slope, knee, or divot (schematic shown in Figure 2.2). We model the transition in the H-distribution as an instantaneous break, as the sample size of our observation does not merit constraining the form of a potential rollover. All H-distributions and values given in this work are presented in H_r unless otherwise specified. Our formulation of the H-distribution allows for the testing of the proposed H-distribution from a single framework.

In the literature, the single slope distribution has been referred to as a single power-law distribution because it corresponds directly to the theorized distributions of diameters, D, which is a power-law to an exponent, $q : \frac{\mathrm{d}N}{\mathrm{d}D} \propto D^{-\mathrm{q}}$. This distribution is convertible to absolute magnitude and parameterized by a logarithmic "slope" α: $\frac{\mathrm{d}N}{\mathrm{d}H} \propto 10^{\alpha H}$, with $q = 5\alpha + 1$. H-distributions can be mapped to D-distributions, with an albedo, providing an observable way to probe size-distributions.

In order to create a synthetic H-distribution sample with a transition, one randomly samples from the two single-slope distributions (bright and faint ends), choosing which to sample from according to the fraction of the total distribution each section comprises. If the bright end of the distribution accounts for 60% of the whole distribution, then when randomly drawing objects, 60% of the time they should be drawn from a single-slope H-distribution corresponding to the bright distribution, and thus 40% of the time they should be drawn from the faint end distribution. The ratio of the number of objects in the bright end of the distribution to the total distribution depends on the two slopes, the contrast, the break magnitude, and the faintest magnitude, $H_{faintest}$; no normalization constants or knowledge of population size are required. The ratio can be calculated with (see Shankman 2012 for a derivation):

$$\frac{N_{bright}}{N_{total}} = \left(1 + \frac{\alpha_b}{\alpha_f}\,\frac{1}{c}\,\left(10^{\alpha_f\left(H_{faintest} - H_b\right)} - 1\right)\right)^{-1} \tag{2.1}$$

The H-distribution has four parameters: α_b, α_f, H_{break}, and c; with arguments from other TNO populations, we fix two of these parameters. Our sample of large-size objects is not large enough to measure the large-end slope, α_b. Motivated by other hot TNO populations, we fix $\alpha_b = 0.9$, which matches our bright-end sample and is consistent with the slopes found for the hot Classical belt (Fuentes & Holman 2008; Fraser & Kavelaars 2009; Petit et al. 2011), the aggregated hot population (Adams et al. 2014; Fraser et al. 2014), the 3:2 resonators (Gladman et al., 2012; Alexandersen et al., 2016) and the pre-transition scattering plus Hot Classical TNOs (Adams et al., 2014). As in Shankman et al. (2013), we fix the break location to H_r

= 8.3 (corresponding to $H_g = 9.0$ and $D \approx 100$ km for 5% albedo). A single-slope H-distribution of $\alpha = 0.9$ to the break magnitude of $H_r = 8.3$ is not rejectable at even the 1-σ level by our sample, and thus provides good agreement to our observations. A steep slope and break at $H_r = 8.3$ is consistent with the Adams et al. (2014) scattering and Hot Classical TNO H-distribution with $\alpha = 1.05$ measured down to $H_r \sim 6.7$ that did not find a break, and the hot population breaks of $H_r = 8.4$ and $H_r = 7.7^{+1.0}_{-0.5}$ found by Fraser et al. (2014). Our detected sample near the transition is not large enough to constrain the exact position of the break; moving the break location by several tenths of magnitude does not affect the conclusions of this work. Having fixed two parameters, we are left α_f and c as free parameters to test and constrain.

2.4.4 Colors and Light Curves

Because CFEPS was primarily performed in g-band and Alexandersen et al. (2016) and OSSOS were performed in r-band, we must account for conversion between these two filters. The majority of our detections (13 vs 9) are r-band detections and so we choose to convert everything to r, requiring us to adopt a $g - r$ color conversion for both the survey simulator and our detections. We do not have measurements of g and r for all of our objects, and so we adopt the CFEPS reported color conversion of $g - r = 0.7$ (Petit et al., 2011) which is consistent with the color measurements we do have for our scattering TNOs. This conversion allows us to combine the samples from several surveys.

We convert all of our observed scattering TNOs into r-band with the above conversion. We select colors for our modeled objects from a gaussian $g - r$ distribution centered at 0.7 with a standard deviation of 0.2 (the range seen in the CFEPS object sample with $g - r$ available). We test our analysis by choosing extreme values for our color conversions (i.e. 0.5 and 0.9). The effects of these color choices do not alter the conclusions of the analysis (see Section 2.6.1).

While the survey simulator allows for the modelling of light curve effects, we do not model the unknown light curves of our scattering TNO sample. Each of our detections is measured at a random phase of its light curve and the magnitude of light curve variation is small in comparison to the uncertainty in converting between detection band passes, which we show has no meaningful impact on our analysis (see Section 2.6.1). We conclude that light curves do not affect our analysis.

2.4.5 Statistics

We want to test whether our model (orbital distribution, H-magnitude distribution, and observation biases) is a good representation for our observations. Having generated a set of simulated detections for a candidate H-distribution, we then test the hypothesis that our detected sample can be drawn from the simulated detections. If this hypothesis is rejected, the model used to generate our simulated detections is rejected; in particular, we conclude that this is a rejection of the candidate H-magnitude distribution used. We use a variant of the Anderson-Darling statistical test (Anderson & Darling, 1954) to assess if our observations can be drawn from our simulated detections for a candidate H-magnitude distribution.

The Anderson-Darling test is a variant of the Kolmogorov-Smirnov two-sample test, weighted such that there is greater sensitivity to the tails of the distribution (Anderson & Darling, 1954). The test metric can be thought of as the distance between two cumulative distributions. Typically, the test is used to determine if data are consistent with being drawn from a well known distribution (e.g. normal, uniform, lognormal) for which there is a look-up table of critical values for the AD metric. In our case, our simulated detections take the place of the well known distribution, and we have no look-up table of critical values for the metric. We therefore bootstrap our sample, repeating draws of 22 objects (the same as our observed sample), calculating their AD distance from their parent distribution in order to build a distribution of critical values for the simulated sample distribution. If the AD metric for our observed sample is in the tails (3-σ of the bootstrap-built distribution for our simulated detections), we reject the hypothesis that our observations could have been drawn from the candidate simulated detection distribution and we thus reject the candidate H-distribution used.

We apply the AD test across several variables in our data set. We have a set of observed scattering TNOs which can be characterized by their orbital parameters and their observable characteristics. We test our model on a combination of three orbital parameters (semi-major axis, inclination, pericenter) and three observable parameters (magnitude at detection, distance at detection, H-magnitude). We sum the AD metrics for all of our tested distributions, and use this summed metric to test for the rejection of our model. While bootstrapping to build up our distribution of critical values as described above, we sample out 22 objects and simultaneously compute the AD metric for each distribution, as opposed to testing the distributions independently. This preserves the relationships between the parameters; in essence we calculate the dimensionless AD metric for a set of 22 orbits across our six observational and dynamical characteristics to build a distribution of AD values. We use the sum of the AD metrics, as the sum will be small if all of the distributions are in good agreement, large if one is in poor agreement or several are in moderately poor agreement, and larger still if all are in poor agreement (Parker, 2015). This approach has less power than rejecting based on the worst failing tested distribution, as has been commonly done in the literature, but is a more robust and multivariate approach.

2.5 Results: Absolute Magnitude Distribution

We test a grid of α_f (0.0 - 0.9) and contrast, c, (1 - 100) values, and a range of single-slope α values (0.1 to 0.9), performing a simulated survey for each candidate H-distribution. Our scattering TNO sample rejects single slopes, requiring a transition to a shallower α_f slope. We determine the plausible c and α_f values that are consistent with our observed sample. The depth of the added surveys and the added observation sample provide a significant improvement in constraining the H-distribution, with a much higher rejection power over the analysis of the CFEPS sample alone (Shankman et al., 2013).

We find that there is a dearth of small objects in the detected sample compared to the number predicted by H-distributions with steep slopes. Steep slopes dramatically overpredict the number of small objects, providing strong leverage to reject such H-distributions. The blue dashed line in Figure 2.3 shows the over-prediction of a single-slope of 0.9, in particular in panels E and F. This is the the strongest rejection of a single-sloped H-distribution in a TNO sub-population.

Our sample rejects all single slopes in the range 0.1 - 0.9 at greater than 95% significance with the exception of $\alpha_f = 0.5$, due to measuring a shallow slope across a transition. When measuring a small sample across a transition from a steep region to a shallow region, a moderate slope can average out to an acceptable match across the distribution. This effect can also explain the shallow slope found by Fraser et al. (2010). Testing the 0.5 H-distribution in pre-break and post-break slices of H, we find that the candidate H-distribution performs substantially better across the whole distribution, than in either of the slices. Figure 2.4 shows that the H-distribution for a single-slope of 0.5 does not provide a compelling match to the detected sample. A

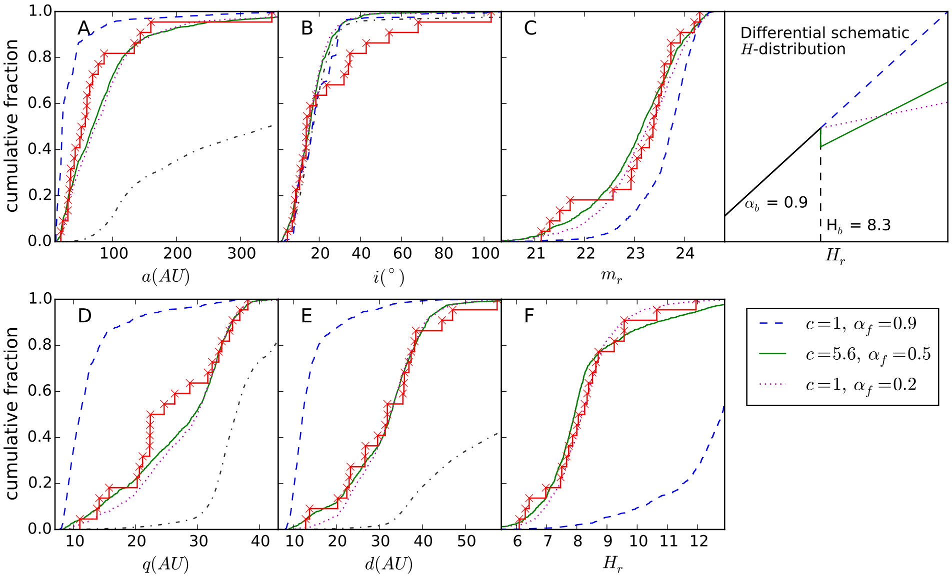

Figure 2.3: Cumulative distributions across six parameters for the intrinsic orbital model (black dash-dot), the observations (red step-function), and three candidate H-distributions (solid green, dotted magenta, and dashed blue). Panels A-F correspond to the semi-major axis, inclination, magnitude at detection in r-band, pericenter, distance at detection, and H magnitude in r, respectively. The rightmost panel provides schematics for our three H-distributions: **(1)** our preferred (c, α_f) pair (solid green; see Section 2.6.2), **(2)** the $\alpha = 0.9$ single-slope distribution (dashed blue), and **(3)** for comparison, our knee distribution which is closest to the Fraser et al. (2014) hot population H-distribution (dotted magenta).

slope of 0.5 has been ruled out by other measurements of the hot TNO populations. A single slope of 0.5 is inconsistent with prior constraints and the non-rejection is likely an artifact arising from measuring a small sample across the transition, and therefore we do not consider a slope of 0.5 to be a plausible H-distribution for the scattering TNOs. Our analysis rejects a single slope ($c = 1$, $\alpha_f = \alpha_b$) as the form of the scattering TNO H-distribution.

The KRQ11 inclination, i, distribution is not representative of our observed sample and is excluded from our analysis. The KRQ11 orbital model contains too few high-i objects to match our observations (see Figure 2.3). The intrinsic and survey simulator-observed i-distributions are very similar, regardless of choice of H-distribution (see Figure 2.3 panel B), indicating that the discrepancy comes from the intrinsic KRQ11 i-distribution. The semi-major axis, a, distribution is strongly

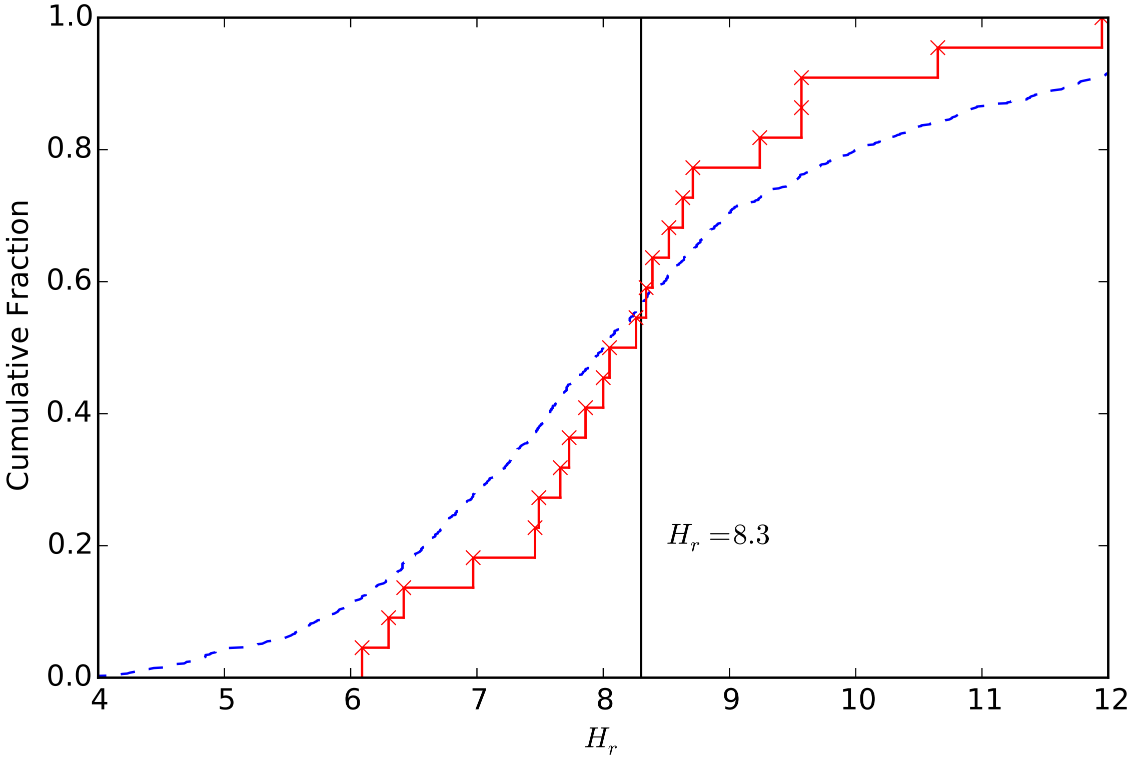

Figure 2.4: Cumulative H-distributions in r for our observed sample (red step function) and a simulator biased single-slopes of $\alpha = 0.5$ (dashed blue). The single-slope of 0.5 over predicts for $H < 8.3$ and under predicts for $H > 8.3$, but provides an acceptable match when measuring across a transition from steep to shallow.

sensitive to the discrepant i-distribution and we thus exclude it from the analysis as well. We demonstrate in Section 2.6.1 that the m, q, d, and H distributions are not dependent on the i and a distributions and that our analysis is not affected by the exclusion of a and i.

We find that the scattering TNO H-distribution is consistent with a range of model distributions that exhibit a knee ($c = 1$) or a divot ($c > 1$). In Figure 2.5 we present a grid of (α_f, c) values that describe H-distributions that are consistent with our scattering TNO sample. All models with $\alpha_f = \alpha_b$ (i.e. single-slope models) are rejected. Figure 2.5 shows that models with $\alpha_f > 0.5$ and $c = 1$ are rejected at or above the 3-σ level. Models with $c = 1$ (i.e. a knee) provide an acceptable distribution for $0 < \alpha_f < 0.5$. Table 2.2 gives the non-rejectable c ranges for each tested α_f. In Table 2.3 we provide population estimates to the limit of our observed sample, $H = 12$, for divots along the 1-σ ridge and all knee distributions not rejectable at 1-

σ. In this H range, the population estimates are relatively consistent, with the largest and smallest estimates differing by a factor of ~ 3. The size of the scattering TNO population provides an observational constraint on the population's H-distribution; our analysis converges to H-distributions that imply a similar size for the intrinsic population in the size range that our survey is sensitive to. Using only this dataset, we constrain the form of the H-distribution to knees and divots; knee distributions may be considered as having fewer free parameters (expressly forcing $c = 1$ as special case of the model) and are thus preferred when no external factors are considered. Having determined the possible parameters of the H-distribution, in the next section we consider the implications of our result for other populations in the outer Solar System.

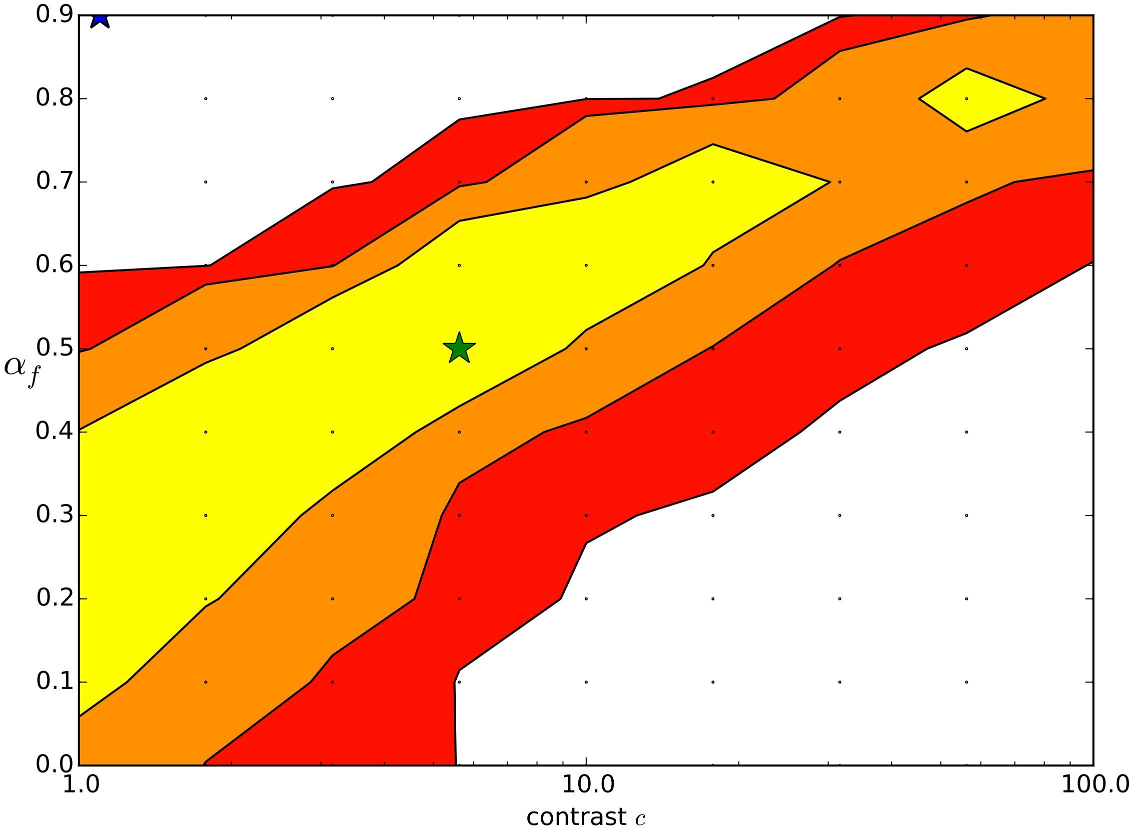

Figure 2.5: Contours of the rejectability for the tested α_f and contrast pairs. The contours represent the 1-σ, 2-σ and 3-σ rejectability levels with white being rejectable at $>$ 3-σ, red being rejectable at $>$ 2-σ, orange rejectable at $>$ 1-σ and yellow rejectable at $<$ 1-σ. The green star denotes our preferred (α_f, c) pair (see Section 2.6.2), and the blue star, offset from $c = 1$ for clarity, denotes the single slope of $\alpha = 0.9$

α_f	c
0.9	56.2 - 100.0
0.8	17.8 - 100.0
0.7	15.6 - 100.0
0.6	3.2 - 56.2
0.5	1.0 - 31.6
0.4	1.0 - 17.8
0.3	1.0 - 10.0
0.2	1.0 - 5.6
0.1	1.0 - 3.2
0.0	1.0 - 3.2

Table 2.2: This table gives the non-rejectable contrast values contained in the 3-σ contours of Figure 2.5, arranged by faint slope, α_f. A contrast value of 1 corresponds to a knee and all other contrast values are divot H-distributions.

	Divots	
α_f	**contrast**	**Pop. Est.** # $[H < 12]$
0.4	1.8	6.4×10^5
0.5	3.2	7.6×10^5
0.5	5.6	5.0×10^5
0.6	5.6	8.3×10^5
0.6	10	5.9×10^5
	Knees	
α_f		**Pop. Est.** # $[H < 12]$
0.4		7.9×10^5
0.3		3.6×10^5
0.2		5.3×10^5
0.1		2.4×10^5

Table 2.3: Population estimates for divots along the $1-\sigma$ ridge in Figure 2.5 and all knees that are not rejectable at the 1-σ level. Population estimates are given to $H_r = 12$, the limit of the observed sample. Population estimates are determined by counting the number of required model object draws for a simulated surveys to reproduce the observed number of detections, 22.

2.6 Discussion

We have constrained the form of the scattering TNO H-distribution to a set of acceptable α_f and c pairs. In this section we discuss the choice of model, including the orbital model and color distribution, and we argue in favor of a divot H-distribution for the scattering TNOs.

2.6.1 Choice of Model

As this work is model dependent, it is important to examine the effects of model choice. The scattering TNOs are insensitive to the history of the exact number and configuration of planets in the outer Solar System (Shankman et al., 2013) as long as the end-state is the current planet configuration; the scattering TNO interactions are so disruptive and chaotic that the exact history is "erased". We have shown above that the KRQ11 i-distribution is discrepant with our observations, and we thus test the effects of the i-distribution on this work. We perform the same analysis as above on the original version of the KRQ11 orbital model, which has a colder initial i-distribution that is then evolved forward for the age of the Solar System. Figure 2.6 shows the simulator-observed cumulative distributions for both the initially hot (green) and initially cold (blue) models with the same H and color distributions. While the i and a distributions vary dramatically between the two orbital models, the m, q, d and H distributions only show small variations that do not statistically differentiate the two models. Figure 2.7 shows the confidence contours for the hot model (solid contour as in Figure 2.5) and cold model (blue line overlays) when testing the AD statistic on the m, q, d and H distributions. There is only minor tension between these two models which have good agreement at the 3-σ level. The observed objects Drac (peculiar i) and MS9 (peculiar a) have distinct orbital elements, but are classified as scattering TNOs by the Gladman et al. (2008) criterion. Given their unusual orbital elements, we consider that they may not be members of the scattering TNO population and we examine the effect of their inclusion in the analysis. Drac and MS9 have no effect on the conclusions of the analysis for the a and i distributions. Removing Drac and MS9 from the analysis also removes the tension between the hot and cold orbital models when testing on m, q, d and H and has no effect on the conclusions of this work regarding the a and i distributions. Our analysis is not strongly dependent on the i-distribution of the orbital model when testing on the m, q, d and H distributions.

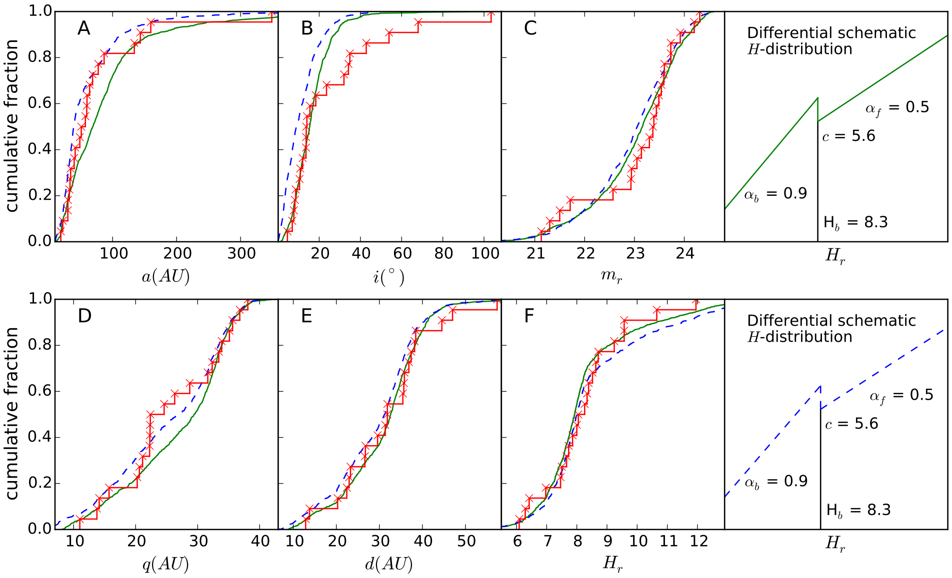

Figure 2.6: Cumulative distributions for the hotter inclination (solid green) and colder inclination (dashed blue) KRQ11 models using the same H-distribution for clear comparison. Colors and panels are as in Figure 2.3 with the exclusion of the intrinsic orbital model distributions (black dash-dot in Figure 2.3). In panel A and in panel B the two KRQ11 orbital model distributions (cold, hot) differ strongly from each other. Panel A shows that the a-distribution is strongly dependent on the initial i-distribution. In panels C-F the two KRQ11 orbital models (cold, hot) only show minor variations from each other; testing with either model on these distributions does not affect the conclusions of this work.

We also test the effects of the $g-r$ color distribution used. In our analysis we draw model object $g-r$ colors from a gaussian centered at 0.7 with a standard deviation of 0.2, based on the measured CFEPS $g-r$ colors (Petit et al., 2011). We test the effects of our adopted $g-r$ distribution by performing the same analysis with fixed $g-r$ values at the 1-σ extremes of our adopted distribution. Figure 2.8 shows the results of performing the same analysis with color conversions of $g-r = 0.5$ and $g-r = 0.9$. There is no tension between rejectable (α_f, c) parameters for these two very different $g-r$ color values. This analysis is not sensitive to exact knowledge of the intrinsic color of the TNOs in our sample, within reasonable bounds on those colors.

We test a combination of the orbital model, the color distribution and the H-distribution. We have shown that our analysis is not strongly dependent on the choice of color distribution nor on orbital model and thus when a candidate model is rejected, it is a rejection of the modeled H-distribution.

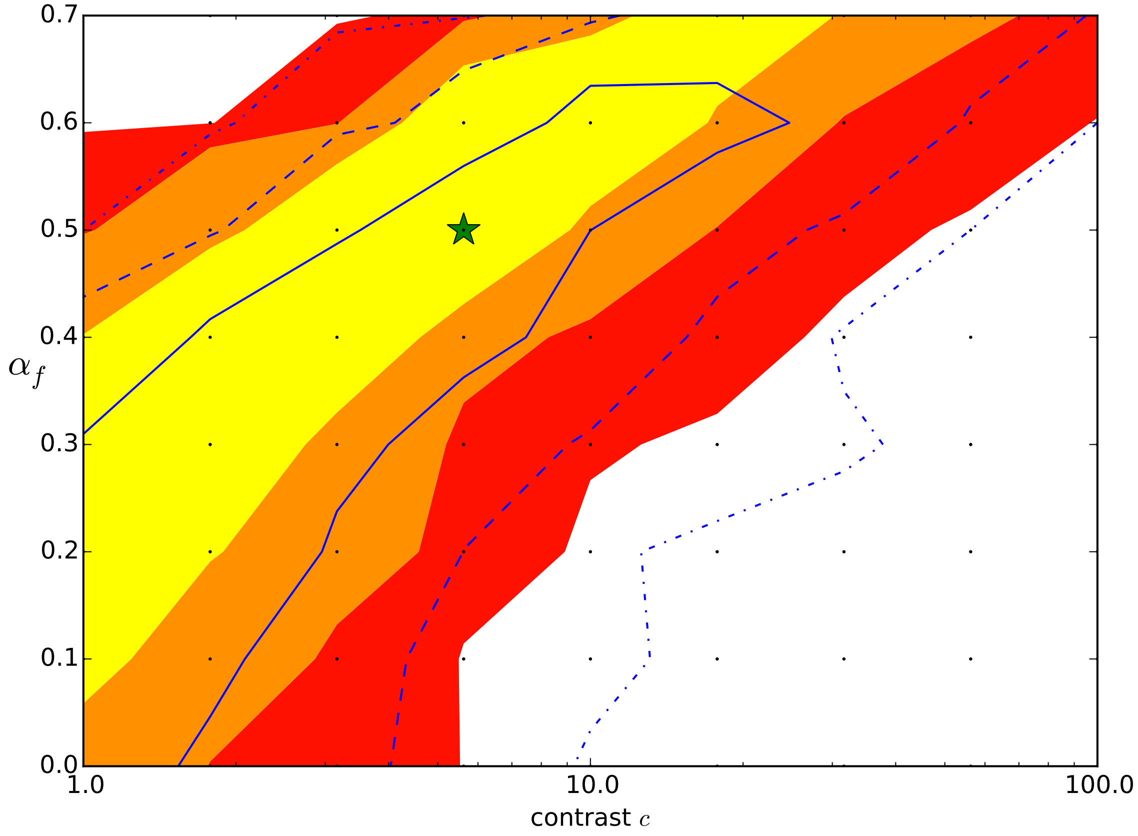

Figure 2.7: Comparison of the contours of rejectability for the hotter KRQ11 orbital model (colors as in Figure 2.5) and the colder inclination KRQ11 orbital model (blue overlaid lines). The blue lines represent the 1-σ (solid), 2-σ (dashed) and 3-σ (dash-dot) contours for the colder KRQ11 orbital model. The green star indicates our preferred (α_f, c) parameters. There is only minor tension between these models.

2.6.2 Arguments for a divot

Motivated by the measured JFC slopes (see Solontoi et al. (2012) Table 6), the Centaur slopes (Adams et al., 2014), and the theoretical slope of collisionally ground populations (O'Brien & Greenberg, 2005), all of which suggest $\alpha_f \sim 0.5$, we favor $\alpha_f = 0.5$. Our analysis has constrained the scattering TNO H-distribution to contrast values ranging from 1 (knees) to ~ 32 (divots) for $\alpha_f = 0.5$. Here we consider the implications of a shared H-distribution among the hot populations of the outer Solar System. We use the observed Neptune Trojan and Plutino samples and the

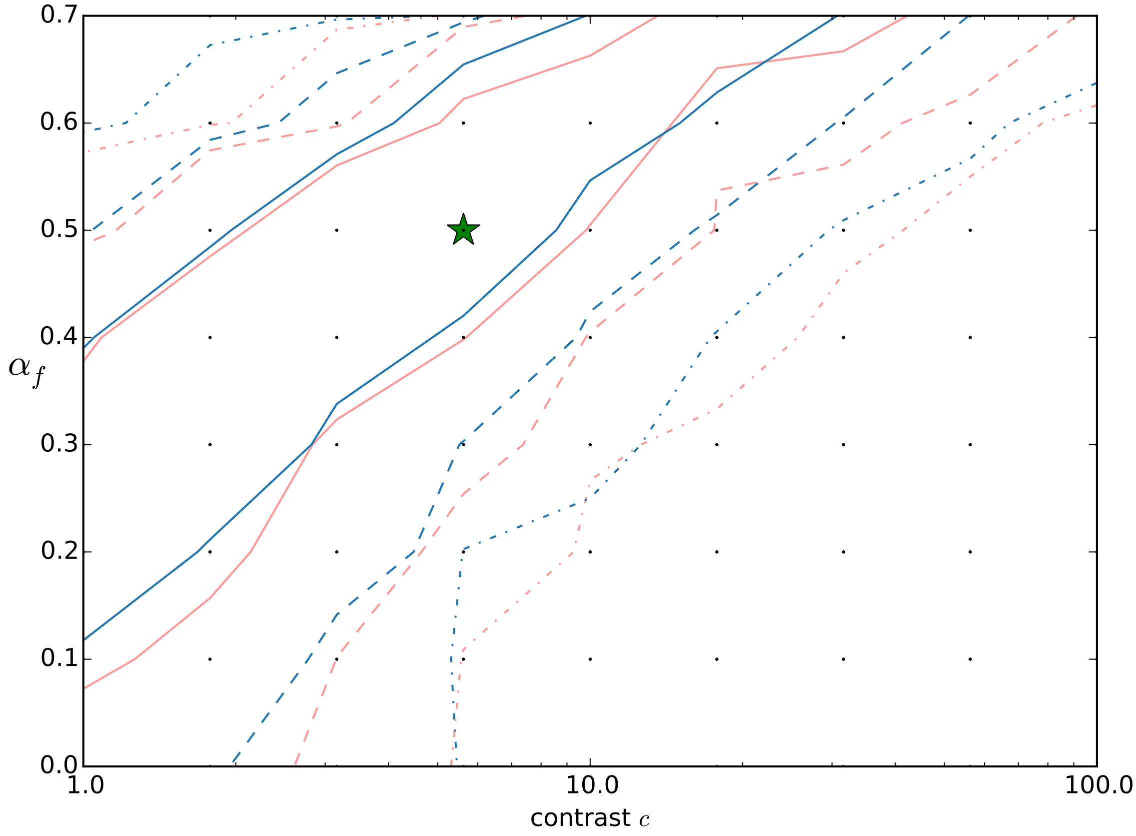

Figure 2.8: 1, 2, and 3-σ contours (solid, dashed, and dash-dot lines respective) for two extreme cases of $g - r$ color choice. The blue lines denote $g - r = 0.5$ and the red lines denote $g - r = 0.9$. The green star marks our preferred (α_f, c) parameters. There is no tension between these two color choices.

JFC source problem to inform the scattering TNO c value.

Requiring the scattering TNOs to be the source of the JFCs sets strong lower limits on the size of the scattering TNO population (Volk & Malhotra, 2008), which can be used to constrain the form of the H-distribution. Volk & Malhotra (2008) find $(0.8 - 1.7) \times 10^8$ $D > 1$ km scattering TNOs in the 30-50 AU heliocentric distance range are required in order for the scattering TNOs to be the JFC source region. To apply this constraint to our measured H-distribution values, we extend our knee and divot population estimates down to $D \sim 1$ km, using albedos of 5% and 15%, the range of measured albedos for the scattering TNOs and the Centaurs (Santos-Sanz et al., 2012; Duffard et al., 2014). H-distributions with $c \leq 10$ and $\alpha_f = 0.5$ produce a scattering TNO population that is large enough to act as the source of the JFCs for both 5% and 15% albedos. For $c = 1$ (knees), our sample requires $\alpha_f \geq 0.4$ for 5%

albedo and $\alpha_f \geq 0.5$ for 15% albedo. If the H distribution transitions to a shallow slope of $\alpha_f \sim 0.2$ as seen in Fraser et al. (2014) and not rejected by this analysis, it must then transition to a third, steeper, slope, α_{f2}, at a smaller H in order for the scattering TNOs to be numerous enough to act as the source population of the JFCs. A transition to $\alpha_f \sim 0.2$ in the scattering TNO H-distribution requires two transitions, the faint one at a break that has yet to be observed, and three slopes in order to explain the source of the JFCs. The H-distribution of the scattering TNOs must transition to $\alpha_f \geq 0.4$ slope to provide a large enough scattering TNO population to act as the source for the JFCs.

Under the hypothesis that all of the hot TNO populations were implanted from the same source, a contrast value of $c > 1$ (a divot) is preferred as this would simultaneously explain the Neptune Trojan and Plutino H-distributions. The Neptune Trojans must have been captured from the scattering TNOs and thus share the same H-distribution. The observed lack of small-sized Neptune Trojans (Sheppard & Trujillo, 2010; Parker et al., 2013) requires that there be a sharp decrease in the number of Neptune Trojans below a certain size. Figure 3 of Sheppard & Trujillo (2010) shows that this decrease must be in the form of a drop in the *differential* number distribution of Neptune Trojans in order to explain the lack of detected Neptune Trojans within their magnitude limit. This drop can either be explained by a *differential* H-distribution of a transition to a steep negative slope, disfavoured by our sample of scattering TNOs, or an H-distribution with $c > 1$. The preference of $c > 1$ from jointly considering the scattering TNOs and Neptune Trojans must also be consistent with the Plutino population if these three hot populations share a common source. Alexandersen et al. (2016) find a decrease in observed Plutinos at H magnitudes fainter (smaller) than our reported transitions in the scattering and Neptune Trojan H-distributions. Exploring a variety of H-distribution parameters, Alexandersen et al. (2016) find that the divot parameters favored by Shankman et al. (2013), with no tuning, provide a good representation of the observed H-distribution for $5 < H < 11$ Plutinos. A divot ($c > 1$) solution simultaneously matches the observed scattering TNO, Neptune Trojan, Centaur, and Plutino H-distributions.

The Shankman et al. (2013) preferred H-distribution, with parameters of $\alpha_f = 0.5$ and $c \sim 5.6$, continues to provide an excellent match to our observations, even with the inclusion of two new surveys that add survey depth and double the observed sample. This H-distribution remains our preferred choice for its ability to match our observed Scattering TNO sample. Figure 2.9 shows the population estimates

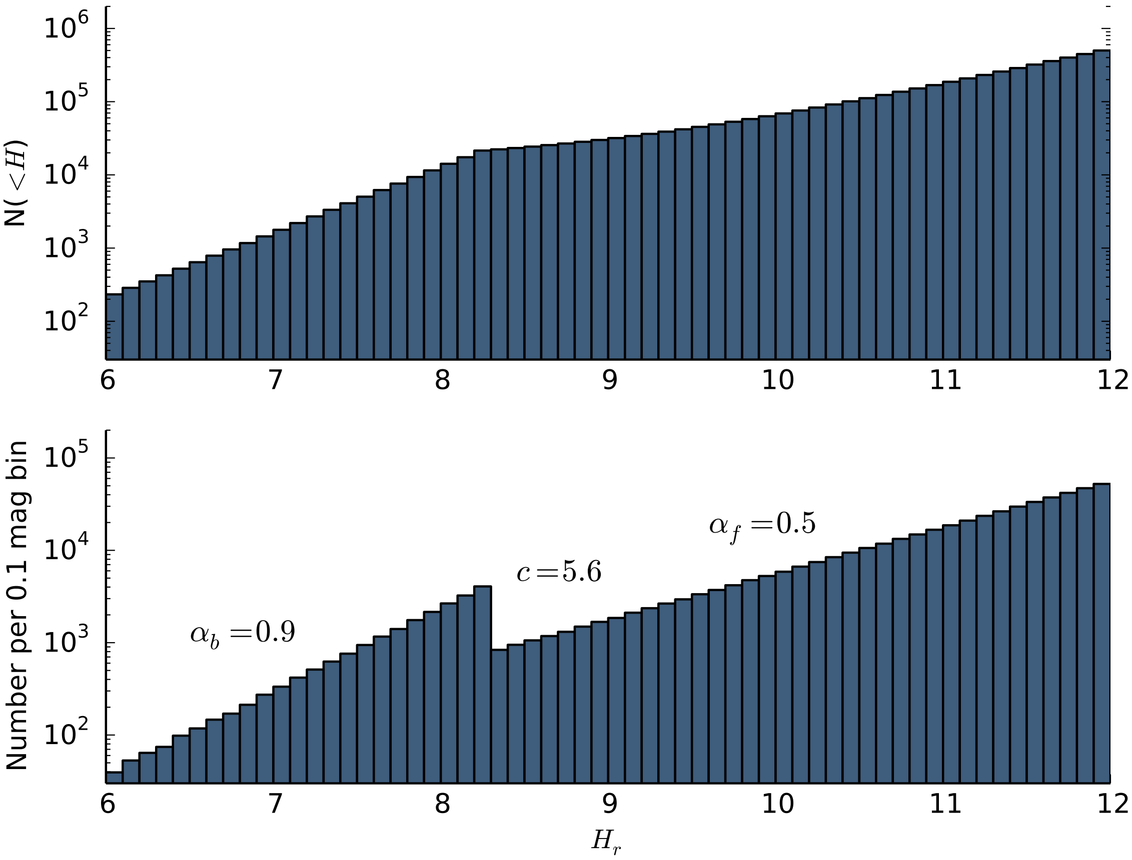

Figure 2.9: Histograms of the population estimate for our preferred (α_f, c) H-distribution. The vertical axes show the estimated total scattering TNO population numbers for this H-distribution. **Top:** The cumulative distribution. The divot with a contrast of $\sim$ 5.6 is a striking feature when viewed differentially, but when viewed cumulatively only results in a small flattened section before $\alpha_f = 0.5$ dominates the distribution and the signature of a divot is erased. **Bottom:** The differential distribution with 0.1 magnitude bins.

for our preferred divot in both cumulative and differential representations. We provide the cumulative representation to highlight how such a visually obvious feature is completely suppressed when viewed cumulatively. The flattening of the cumulative distribution seen in Figure 2 of Sheppard & Trujillo (2010) that then gradually transitions to a positive slope is characteristic of a divot. Figure 2.9 demonstrates that when you view a divot cumulatively, it produces exactly this signature. If there is a divot in the H-distribution of the TNO populations, prior studies of the luminosity function, or even H, could be suppressing the signature of this feature if they combine surveys which were not characterized in the same way

A divot can also explain the rollover to negative slopes that some groups have measured (Bernstein et al. 2004; Fraser & Kavelaars 2009). The transition in the size-frequency distribution for a divot would likely take the form of a steep negative slope over a short size range, rather than a discontinuous drop. If a survey terminates just past the break point, one could measure a signature of this transition as a negative slope without measuring the recovery.

Two different formation mechanisms have been shown to produce divot size-frequency distributions. Fraser (2009) shows that a kink in the size-frequency distribution collisionally propagates to larger sizes and produces a divot. Campo Bagatin & Benavidez (2012) explore the "born big" scenario (Morbidelli et al., 2009) in the Kuiper Belt, collisionally evolving a population with no initial objects smaller than 100 km. As the population evolves under collisions, a divot is produced and the small-sized objects have a collisional equilibrium slope and a contrast of the same scale (~ 5; see Fig. 6 of Campo Bagatin & Benavidez 2012) as our preferred model parameters ($\alpha_f = 0.5$ and $c \sim 5.6$). Divot size-frequency distributions are consistent with our understanding of small-body formation physics, and have been shown to arise from two different formation mechanisms.

Divot H-distributions are plausible, explain our observations and when generalized to other hot TNO populations can explain several outstanding questions. Our preferred H-distribution parameter set is one of the least rejectable H-distributions we tested, provides a good match with the observed H-distribution (see Figure 2.4), is consistent with the observed JFC slopes, can solve the problem of JFC supply, is consistent with the observed Centaur H-distribution, is consistent with the observed Neptune Trojan and Plutino H-distributions and is consistent with divots produced in collisional models. We find a divot of contrast c $\sim$ 5.6 and faint slope α_f to be compelling and argue that it provides a better, versus knees, solution to the observed lack of small-sized hot TNOs while simultaneously explaining the supply of JFCs.

2.7 Conclusion

Using our 22 object scattering TNO sample, we have constrained the form of the scattering TNO H-distribution as a proxy for its size-frequency distribution. Our sample rules out all single-slope distributions and constrains the form to divots or shallow ($\alpha_f < 0.6$) knees. We find that a particular scattering orbital model for the formation of the scattering TNOs is not consistent with the observed i distribution, producing too few high-i scatterers, possibly indicating an additional inclination component in the scattering TNOs. We argue in favor of a divot H-distribution and find a population estimate of (2.4-8.3)$\times 10^5$ down to $H_r = 12$ is required to match our observed sample. Extrapolating our preferred divot H-distribution down to the km scale predicts a scattering TNO population large enough to act as the sole supply of the JFCs, allowing a divot to explain JFC supply, while simultaneously explaining the observed Neptune Trojan, Plutino and scattering TNO size or H distributions.

Chapter 3

Full OSSOS sample scattering TNO analysis

In Chapter 2 I provide a framework for the measurement of scattering TNO H-distributions. Here I provide an update for the measurement of the scattering TNO H-distribution with results from the inclusion of the full OSSOS dataset. OSSOS has completed its observing run, adding three more quarters of discovery, and released the full set of detected TNOs to the team in spring of 2017; the full full dataset will be published in the upcoming survey paper, expected summer 2017. The analysis here follows on the work of Chapter 2, using the same methodologies.

Chapter 2 analyses a scattering TNO sample of 22 objects. OSSOS has since detected 38 new scattering TNOs, bringing the full sample to 60 objects. I performed survey simulations for a grid of candidate H-distributions using the new and complete OSSOS characterisations, in addition to those from CFEPS and Alexandersen et al. (2016) following the same methodology in the preceding chapter. I find that the preferred divot H-distribution from Chapter 2 remains a viable explanation for the scattering TNO H-distribution and that the number of rejectable models increases.

An analysis of the orbital parameters (Figure 3.1) shows that the preferred divot ($\alpha_f = 0.5$, green line) and a divot with a shallower post-transition slope ($\alpha_f = 0.4$, blue dashed line) provide a good match to the observed sample, which has now nearly tripled in number. A divot with $\alpha_f = 0.5$ shows discrepancies with the observed sample in d, H, and q that are greater than a divot with $\alpha_f = 0.4$, indicating that there are too many simulated detections at small sizes (large H). The original model, first proposed in Shankman et al. (2013), still provides one of the most convincing matches to the observed scattering TNO H-distribution, even with the sample size having increased by nearly a factor of 5 since the original analysis.

An analysis of the non-rejectable H-distributions (Figure 3.2) shows the increased constraints imposed by the full OSSOS dataset. There is broad agreement between these results and the previous results shown in Figure 2.5.

The distribution of craters on a planetary surface can be used to infer the distribution of impactor sizes. Using imaging from the New Horizons Pluto encounter, the distribution of impactor sizes has been estimated to arise from an H-distribution with $\alpha = 0.4$ (Singer et al, submitted). The impactors have sizes that are smaller than the smallest scattering TNO in this dataset. If the hot populations provide the source of Pluto impactors, the small-size (large-H) scattering TNO slope should be in agreement with the cratering records on Pluto. In order to have $\alpha_f = 0.4$ and a break location at $H_r = 8.3$, a divot is required to match the scattering TNO population.

Fraser et al. (2014) finds a break location at larger sizes, near $H_r = 7.7$, which transitions to a knee with shallow slope of $\alpha_f = 0.2$. Figure 3.3 and Figure 3.4 show the acceptable scattering TNO H-distributions for break locations of $H_r = 7.7$ and $H_r = 7.2$, respectively. This shows that a transition at larger size (smaller H) to a shallow slope remains an acceptable match for the TNO H-distribution across a range of break locations.

This work is an exploration of the scattering TNO H-distribution with the full OSSOS sample. I have demonstrated that existing models (both the divot and knee) provide acceptable matches for the observed scattering TNOs. The divot scattering TNO distributions are consistent with the Pluto cratering record. Divot H-distributions remain uniquely able to explain the observed size and H-distributions of all of the TNO hot populations while simultaneously explaining the source for the JFCs.

A full exploration of possible size distributions would be best done in the context of a formation and evolutionary model of the Solar System. We are reaching the limits of the current approach of constraining the form of the H-distribution, and now require models of fully consistent self evolution. The current degeneracy across potential break locations and divot or knee distributions can be addressed through additional constraints from formation theories. In order to explore this, one must understand the conditions under which accretion takes place (e.g. born big or core accretion) and must also understand the dynamical excitation process (e.g. Neptune migration) that emplaced the hot TNOs and shut off collisional grinding. As a clue for these processes, I now look to the dynamics of the large-a TNOs whose unknown dynamical origins may contain tracers of the TNO emplacement history.

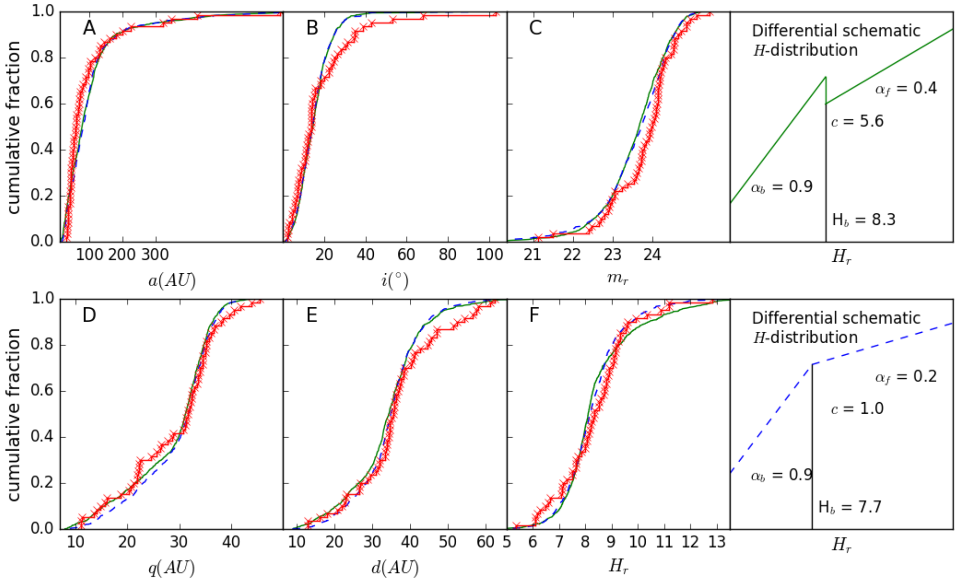

Figure 3.1: Cumulative distributions across six parameters for the intrinsic orbital model (black dash-dot), the observations (red step-function), and two candidate H-distributions (solid green and dashed blue). Panels A-F correspond to the semi-major axis, inclination, magnitude at detection in r-band, pericenter, distance at detection, and H magnitude in r, respectively. The rightmost panel provides schematics for our three H-distributions: **(1)** our preferred (c, α_f) pair (solid green; see Section 2.6.2) and **(2)** the Fraser et al. (2014) knee (dashed blue)

. The divot distribution is rejectable at 76% and the knee is rejectable at 74%.

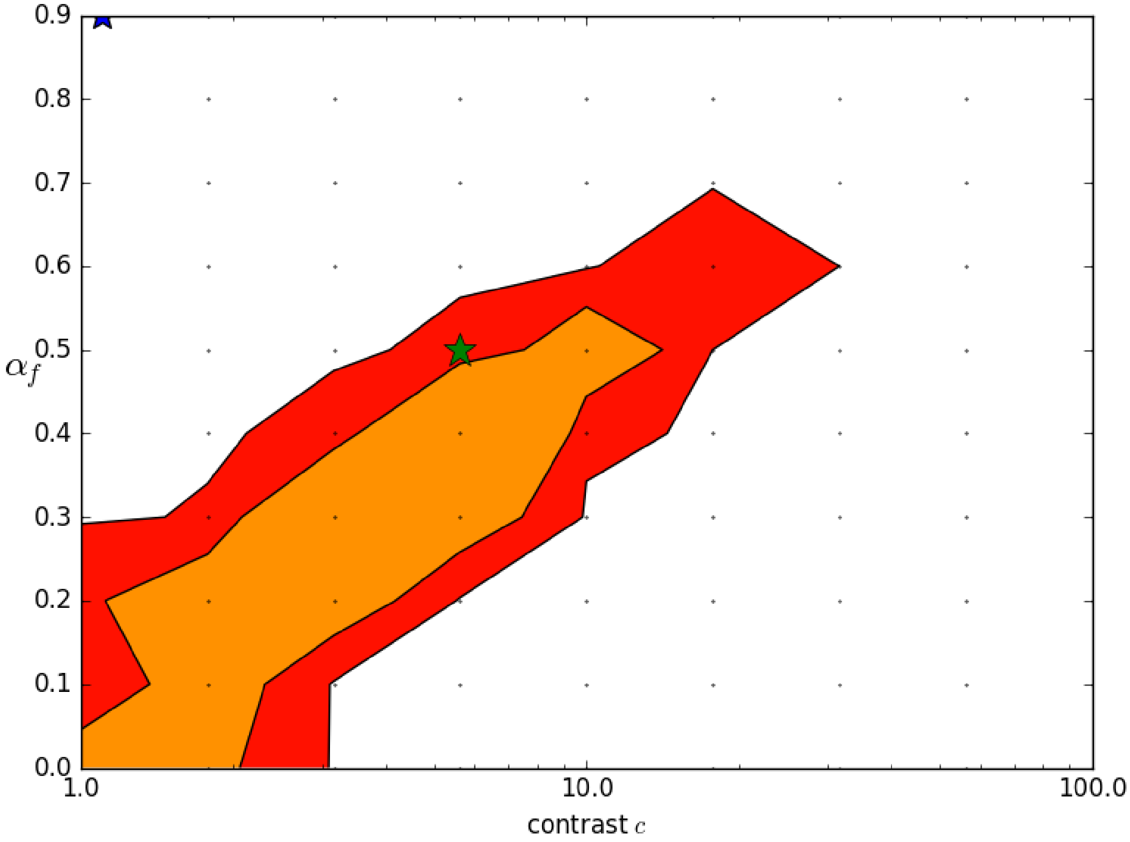

Figure 3.2: Contours of the rejectability for the tested α_f and contrast pairs with a break located at $H_r = 8.3$. The contours represent the 1-σ, 2-σ and 3-σ rejectability levels with white being rejectable at $>$ 3-σ, red being rejectable at $>$ 2-σ, and orange rejectable at $>$ 1-σ. The green star denotes our preferred (α_f, c) pair (see Section 2.6.2), and the blue star, offset from $c = 1$ for clarity, denotes the single slope of $\alpha = 0.9$

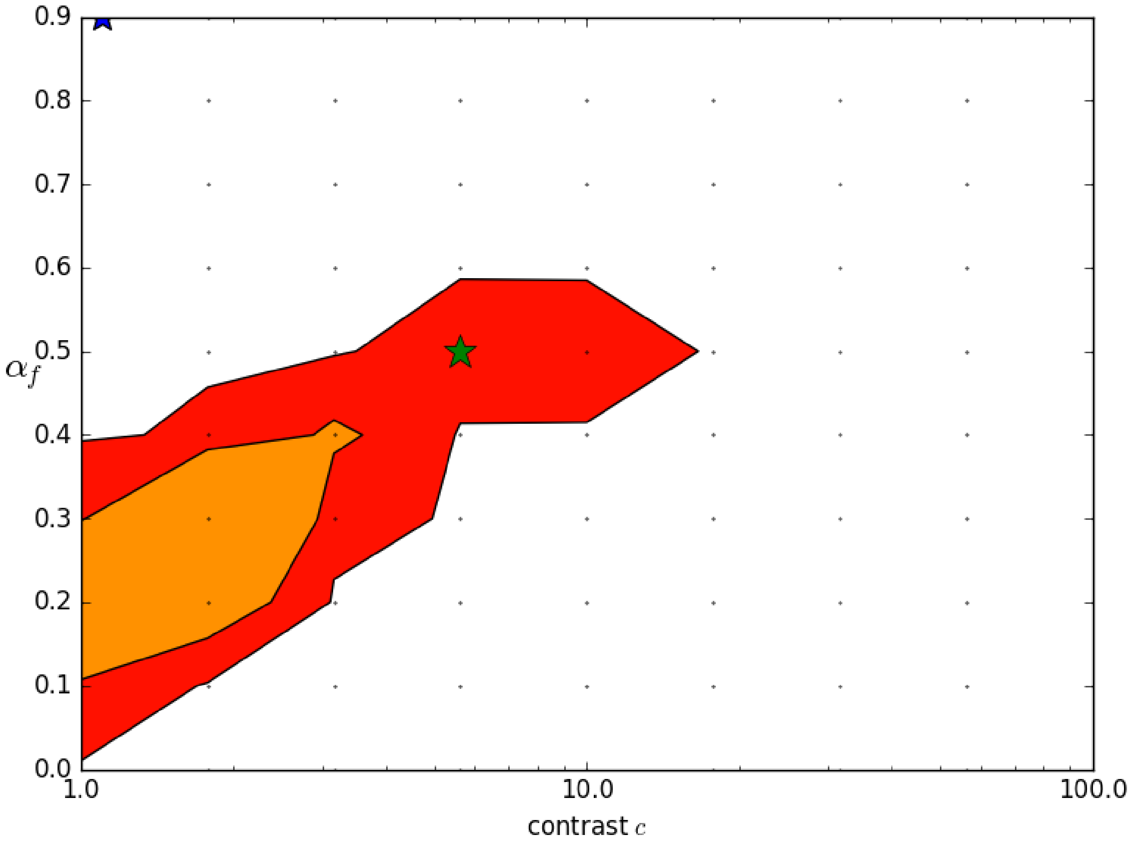

Figure 3.3: Contours of the rejectability for the tested α_f and contrast pairs with a break located at $H_r = 7.7$ as in Fraser et al. (2014). Plot styles as described in Figure 3.2

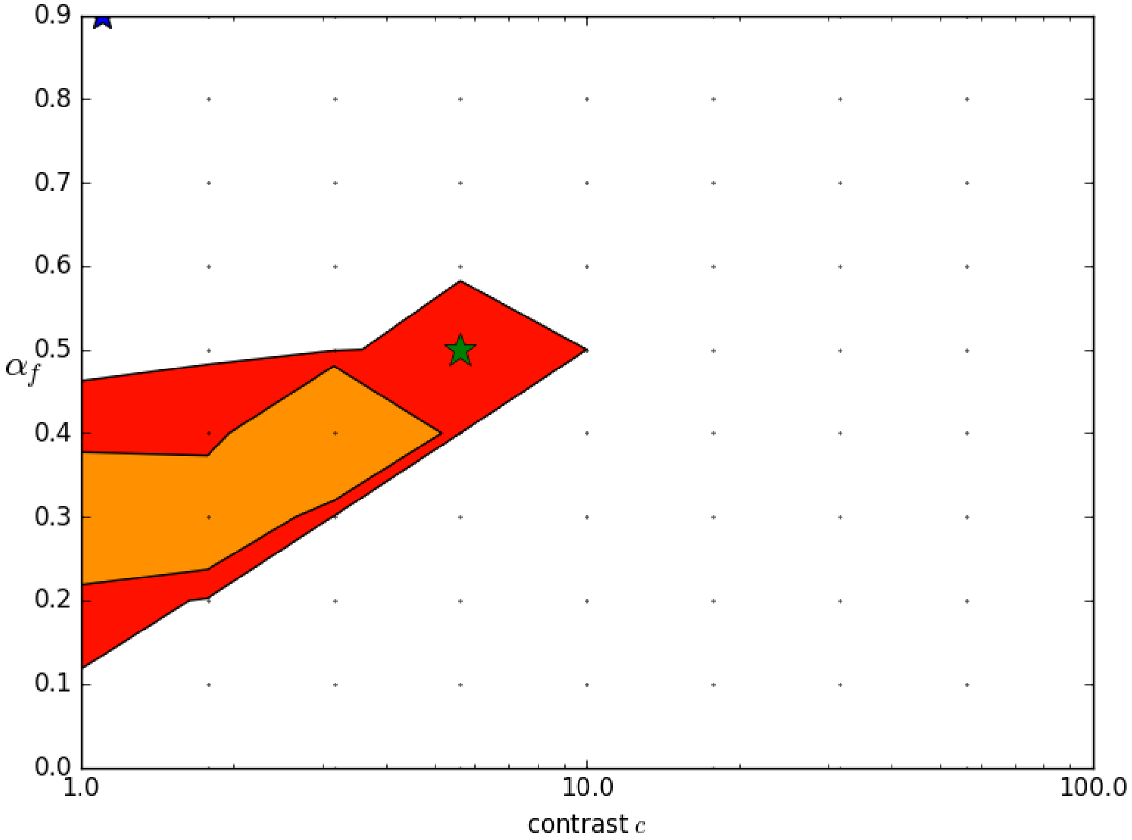

Figure 3.4: Contours of the rejectability for the tested α_f and contrast pairs with a break located at $H_r = 7.2$. Plot styles as described in Figure 3.2

Chapter 4

A Ninth Planet Would Produce a Distinctly Different Distant Kuiper Belt

Published as: S. M. Lawler, C. Shankman, N. Kaib, M. T. Bannister, B. Gladman, and J. J. Kavelaars 2017 *AJ* 153 33

*R*eproduced here with the permission of S. M. Lawler

Available online here: http://iopscience.iop.org/article/10.3847/1538-3881/153/1/33/meta

4.1 Abstract

The orbital element distribution of trans-Neptunian objects (TNOs) with large pericenters has been suggested to be influenced by the presence of an undetected, large planet at 200 or more AU from the Sun. We perform 4 Gyr N-body simulations with the currently known Solar System planetary architecture, plus a 10 $M_\oplus$ planet with similar orbital parameters to those suggested by Batygin & Brown (2016a) or Trujillo & Sheppard (2014), and a hundred thousand test particles in an initial planetesimal disk. We find that including a distant superearth-mass ninth planet produces a substantially different orbital distribution for the scattering and detached TNOs, raising the pericenters and inclinations of moderate semimajor axis ($50 < a < 500$ AU) objects. We test whether this signature is detectable via a simulator with the observational characteristics of four precisely characterized TNO surveys. We find that the qualitatively very distinct Solar System models that include a ninth planet are essen-

tially observationally indistinguishable from an outer Solar System produced solely by the four giant planets. We also find that the mass of the Kuiper Belt's current scattering and detached populations is required be 3–10 times larger in the presence of an additional planet. Wide-field, deep surveys targeting inclined high-pericenter objects will be required to distinguish between these different scenarios.

4.2 Introduction

The trans-Neptunian region contains far more structure than the originally hypothesized flat vestigial disk (Edgeworth, 1949; Kuiper, 1951). While the bulk of the Kuiper Belt's mass is contained in the classical belt, which has TNOs on fairly circular, low inclination orbits, TNOs on higher eccentricity orbits are plentiful. Resonant TNOs are protected from close Neptune encounters and can attain high eccentricity, allowing them to be more easily detected when near perihelion. Scattering TNOs often approach the Sun even more closely, as by definition they are required to have scattering encounters with Neptune or another giant planet (Gladman et al., 2008) and thus have pericenters in the giant planet region. Though scattering TNOs can have very large semimajor axis orbits ($a \gg 50$ AU) and only make up ∼2% of the Kuiper Belt's total population (Petit et al., 2011), their very high eccentricities boost detection rates, allowing detailed study of the population's characteristics (Shankman et al., 2013; Adams et al., 2014; Shankman et al., 2016). Detached TNOs make up a larger fraction of the Kuiper Belt total population (∼29% for $D \gtrsim 100$ km; Petit et al., 2011), but never approach Neptune closely enough to have their orbits affected by scattering encounters, and so are much harder to detect, due to their high pericenter distances and large semi-major axes.

The history of the understanding of the $a > 50$ AU population is important context that frames both our current conception of these distant TNOs and their implications for an additional planet in this region. The $a \simeq 40 - 50$ AU low-e Kuiper Belt initially seemed promising as the long-sought source of the Jupiter-Family comets (JFCs). However, once the population was observationally constrained, the estimated escape rate from that region was too low to allow it to serve as a JFC source (Duncan et al., 1995). It became clear that no near-circular belt in the trans-Neptunian region *could* feed in JFCs without creating a scattering structure of large-a TNOs once strong encounters with Neptune begin (Duncan & Levison, 1997), and the discovery of the first member of this population, 1996 TL$_{66}$, was nearly simultaneous

(Luu et al., 1997). Dynamical simulations (Duncan & Levison, 1997) showed the surprising possibility that a non-negligible fraction ($\sim$1%) of the initial planetesimal disk could still be in the scattering structure today; it need not be in steady state with an eroding main Kuiper Belt. In this picture, the present-day structure of this scattering population is a band of objects with perihelia dominantly in the range $q \simeq 35 - 39$ AU (Duncan & Levison, 1997; Trujillo et al., 2000; Morbidelli et al., 2004; Lykawka & Mukai, 2007a), steadily decreasing in number as a function of semi-major axis; TNOs are displaced outwards almost solely by gravitational interactions with Neptune; TNOs with $q < 35$ AU are rapidly depleted, and thus relatively rare, while TNOs with $q > 38$ AU are extremely rare. The recognition that TNOs with $q > 38$ AU existed, and in what must be great numbers (Gladman et al., 2002) led to the realization that the perihelion distribution must be extended to larger values (Morbidelli et al., 2004). The current terminology in the literature is to use the term 'detached' for TNOs whose orbits are not today evolving due to Neptune encounters (Gladman et al., 2008), and scattering for those which are. Unfortunately this does not correspond to a simple perihelion cut, although $q = 37$ AU is sometimes used (Lykawka & Mukai, 2007a).

The existence of the detached population requires some other major process, either historical or ongoing, to produce TNOs on these orbits. Sedna (Brown et al., 2004) and recently-discovered 2012 VP_{113} (Trujillo & Sheppard, 2014) are the highest-pericenter examples of detached TNOs. Possible explanations for the production of detached orbits include close stellar flybys (e.g. Kenyon & Bromley, 2004; Brasser & Schwamb, 2015), changes in galactic tides caused by different Solar position within the Galaxy (e.g. Kaib et al., 2011b), "rogue planets" which were ejected early in the Solar System's history (e.g. Gladman & Chan, 2006) and undiscovered, additional planets (e.g. Gladman et al., 2002; Brown et al., 2004). Lykawka & Mukai (2008) suggest the presence of a distant Earth-mass planet to explain some of the structure of the Kuiper Belt, but one of their key arguments requires that there be no objects in distant Neptune mean-motion resonances. Several distant resonances, including the 3:1, 4:1, and 5:1, have been shown by recent surveys to be heavily populated (Gladman et al., 2012; Alexandersen et al., 2014; Pike et al., 2015).

Limits exist on the presence of distant Solar System planets: analysis of data from the Wide-Field Infrared Survey Explorer (WISE) has shown that Jupiter-mass planets can be ruled out within 26,000 AU of the Sun (Luhman, 2014), though a superearth would be too faint in infrared wavelengths to be yet observed in the distant outer

Solar System (5–20 $M_\oplus$; Fortney et al., 2016). The measured position of Saturn using Cassini data has also been used to place constraints on possible distant planets (Iorio, 2014; Fienga et al., 2016). Additionally, Li & Adams (2016) find via dynamical simulations that a distant ninth planet is highly susceptible to disruption by passing stars and is unlikely to survive to the present day on a wide $500 < a < 700$ AU eccentric orbit.

Trujillo & Sheppard (2014) have proposed a superearth on a circular orbit at roughly 250 AU to explain the apparent clustering in argument of pericenter (ω) of a half-dozen detached TNOs with large perihelia. This idea is modified and expanded upon by Batygin & Brown (2016a), who find that an eccentric superearth is capable of apsidally aligning high-pericenter TNOs. However, both of these works rely on data from the Minor Planet Center (MPC) database, the repository of the orbital parameters for all known TNOs[1], but which contains no information about observational parameters of the surveys in which these objects were discovered. The MPC TNOs are from a multitude of different surveys, which largely have unreported pointings, limiting magnitudes, detection efficiencies, and tracking efficiency post-discovery; this masks the true number of TNOs in different dynamical classes (Kavelaars et al., 2008). Biased sampling is particularly prone to affecting the discovery and recovery of the observed high a/e population. An effect such as the apparent clustering of pericenters could be produced or significantly modified in non-intuitive ways. A survey with fully recorded observational biases can be properly debiased, giving the true numbers of objects required to exist in the unseen population in order to match the number of detections (Jones et al., 2006). We therefore select a subset of the published wide-field surveys, permitting highly precise tests of the effects of observational bias on the observability of the distant-TNO orbital distributions. Our test suite is an ensemble of four well-characterized surveys (Section 4.4): the Canada-France Ecliptic Plane Survey (CFEPS; Petit et al., 2011), the HiLat Survey (Petit et al., 2014), the survey of Alexandersen et al. (2014), and the first two sky blocks from the Outer Solar System Origins Survey (OSSOS; Bannister et al., 2016, in press).

Our goal is to see if the addition of a superearth-scale planet generates an observational signature on the scattering and detached populations that is in conflict with available observational constraints. In this paper, we measure the effect a distant superearth would have on the orbital distribution of the high-q ($q > 37$ AU), moderate-a

---

[1] As of 16 May 2016, this database contains 1986 TNOs, Centaurs and scattering objects, ~ 1300 of which have orbits known from observation on multiple oppositions.

($50 < a < 500$ AU) component of the trans-Neptunian populations, using a detailed dynamical simulation containing many thousands of test particles. We consider this population because it orbits beyond the dynamical dominance of Neptune, will be gravitationally sculpted by any potential ninth planet, and has still has pericenters within the detectable range of existing surveys.

We show that although the differences between the intrinsic distribution of high-pericenter TNOs in models with and without an ninth planet are substantial, after observational biases are applied, the differences are currently indistinguishable. The fact that almost all known scattering objects have q=35–38 AU has tended to be viewed as confirmation of the baseline scattering scenario; our results show that the detection biases in the scattering population are so strong that the $q > 38$ AU population could be numerous, but so weakly detectable that they are not represented in the observed sample. Also using the survey simulator, we compare the predicted number of objects in the distant Solar System, and find that having an additional planet requires 3-10 times as many objects in the moderate-a population.

4.3 Orbital Integrations

In order to make a realistic model of the distant TNOs as influenced by a possible superearth, we begin with the framework for building a scattering TNO and Oort Cloud model used by Shankman et al. (2016), which is a modified version of the model from Kaib et al. (2011b). Our three dynamical simulations begin with a hundred thousand massless test particles distributed from 4-40 AU, along with the 4 giant planets on their present-day orbits. The “control” sample is identical to that used by Shankman et al. (2016), while the other two simulations have an additional superearth with similar parameters to what was suggested by Batygin & Brown (2016a) (eccentric P9: $M = 10\ M_{\oplus}$, $a = 500$ AU, $e = 0.5$, $i = 5°$) or what was suggested by Trujillo & Sheppard (2014) (circular P9: $M = 10\ M_{\oplus}$, $a = 250$ AU, $e = 0.0$, $i = 5°$). These test particles and planets are evolved forward in time for 4 Gyr, under the influence of stellar flybys and Galactic tides (for details, see Kaib et al., 2011b). In order to ensure that the scattering and detached populations are not contaminated by the initial 4-40 AU disk, any objects that have $q > 34$ AU and $a < 42$ AU at 3.5 Gyr into the simulation are removed (this is the same procedure used in Shankman et al., 2016), as we are not here interested in the classical belt region.

What makes this simulation much more powerful than previous analyses is the sheer number of particles. As a result, this dynamical simulation was computationally expensive to run. Previous integrations of Kuiper belt and Oort cloud formation were able to be sped up through a combination of adaptive timestepping and the exclusion of planetary perturbations on very distant particles (e.g., Kaib et al., 2011a). However, the inclusion of a distant ninth planet prevents this shortcut. Consequently, our integrations consumed over 10^5 core-hours.

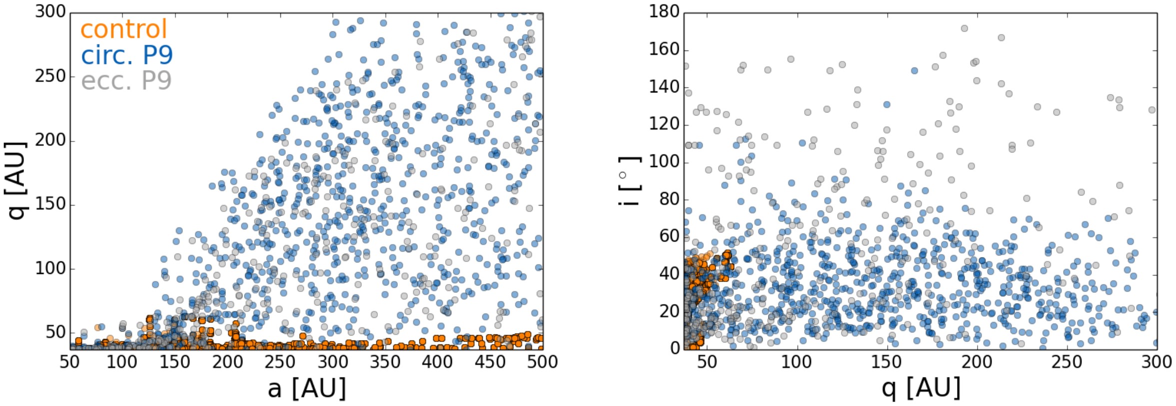

Figure 4.1: Orbital elements of all simulated TNOs with $q > 37$ AU and $50 < a < 500$ AU from the control dynamical model (orange), the circular superarth dynamical model (blue), and the eccentric superearth dynamical model (gray). Left panel shows semi-major axis a vs. pericenter distance q, right panel shows semi-major axis a vs. inclination i. The presence of a superearth on either a circular or eccentric orbit dramatically raises both the pericenter distribution and the inclination distribution of the distant TNOs.

Figure 4.1 shows the orbital element distributions for the high-q population in the control dynamical model (the currently known Solar System; Shankman et al., 2016) and our nine-planet dynamical models after 4 Gyr of integration. The scattering TNO disk visible in the control dynamical model (orange) is the expected population of q=30-38 AU particles extending smoothly out to large a (the classic scattering disk). At no semi-major axes (except a few rare resonant locations which can produce a few lower-e particles via resonance sticking) do perihelia get raised into the detached region. The introduction of a superearth results in frequent perihelion lifting for $a > 150$ AU scattering objects, destroying the confinement and thus potentially offering a production method for the entire detached population all the way out to Sedna.

Figure 4.2 shows the distribution of semimajor axes at the end of each of the

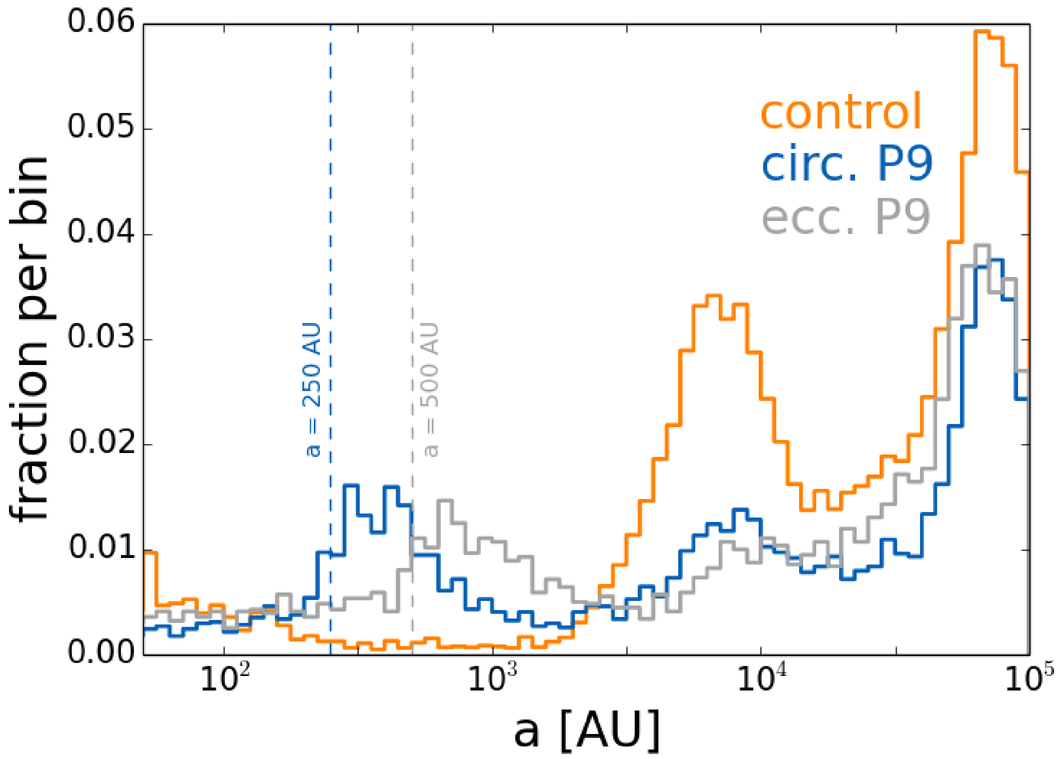

Figure 4.2: Semimajor axis distribution from 50 to 100,000 AU at the $\sim$ 4.5 Gyr state from three simulations: a control dynamical model (orange), the circular superearth dynamical model (blue), and the eccentric superearth dynamical model (gray). Histograms are normalized to the number of objects in each dynamical simulation. The presence of a superearth on either a circular or eccentric orbit produces a concentration in objects with semimajor axes just outside that of the ninth planet.

three simulations. The control shows the number of moderate-a objects per log(a) bin steadily drops with larger distances from Neptune; the scattering physics is poor at retaining a=200-2000 AU objects over 4 Gyr (Dones et al., 2004). Further out, there is a climb to a peak at the inner Oort Cloud, starting at roughly $a \sim 2000$ AU as expected (Gladman et al., 2008). Here the timescale of pericenter raising due to Galactic tides grows short enough that objects are efficiently decoupled from planetary scattering (Duncan et al., 1987). The most distant (and highest) peak is the main, or outer, Oort Cloud, where objects become isotropized by tidal torques. These two Oort Cloud peaks are also seen in the simulations with superearths. Both P9 sims have an additional peak located just outside the semimajor axes of their respective ninth planets; in both simulations there is a $q \sim 200$ AU peak, just inside q of both superearths ($q = 250$ AU).

These simulated orbital distributions are very different from the control case with no additional planet; the next step is to determine whether or not these stark differences are observable with current surveys.

4.4 Simulating Observations with Well-Calibrated Surveys

We use the OSSOS survey simulator (Bannister et al., 2016; Shankman et al., 2016), which offers some improvements on the CFEPS survey simulator (Jones et al., 2006; Petit et al., 2011). The survey simulator works by drawing objects from a dynamical model, applying survey biases for surveys where all the pointings, tracking efficiencies, and detection efficiencies are well-known, and determining whether or not a given simulated object could have been detected.

When each object is drawn from our dynamical model, its major orbital elements (a, e, and i) are randomized within a small percentage of their model values, and its angular orbital elements (ω, Ω, and $\mathcal{M}$) are randomized. The object is also given an absolute H_r magnitude using either the best-fit divot size distribution found by Shankman et al. (2016) for the scattering population, or the knee size distribution preferred by Fraser et al. (2014), but we find that this choice has no statistical effect on the analysis presented here. The object's simulated instantaneous on-sky position, distance, and resulting r-band magnitude determine whether or not this particular object would have been detected and tracked by any of the included surveys. Simulated objects are drawn until the number of simulated detections specified by the user is met.

In this analysis, we use characterizations from four published surveys[2]. A wide range of longitudes along the ecliptic are sampled by three surveys: CFEPS (Petit et al., 2011), Alexandersen et al. (2014), and the OSSOS O and E blocks (Bannister et al., 2016). High ecliptic latitudes are sampled by the HiLat survey (Petit et al., 2014). We focus on the high-q, moderate-a population ($q > 37$ AU, 50 AU $< a <$ 500 AU). These are the objects most strongly perturbed by the distant superearth (Figure 4.1). 15 real TNOs have been detected in this a/q cut in the above surveys,

---

[2] Available for use as an ensemble at `http://dx.doi.org/10.5281/zenodo.31297`

which allows estimation of absolute population numbers (Section 4.4.2).

4.4.1 Superearth-Induced Structure in the Kuiper Belt Region Can't Yet be Observed

Figure 4.1 highlights the differences in orbital elements of the high-q, moderate-a population expected for no superearth, a circular superearth, and an eccentric superearth in the form of scatterplots. The very obvious difference is that the distant planet provides perturbations that raise inclinations and perihelia, potentially addressing two puzzles in Kuiper Belt science (Gomes, 2003; Gladman, 2005). For comparative analysis, it is more straightforward to measure the differences between these distributions as cumulative distributions than scatterplots. Figure 4.3 shows a comparison between the three different dynamical models as cumulative distributions in three different orbital parameters: a, i, and q. Here each distribution has been cut at the same minimum and maximum values for each parameter.

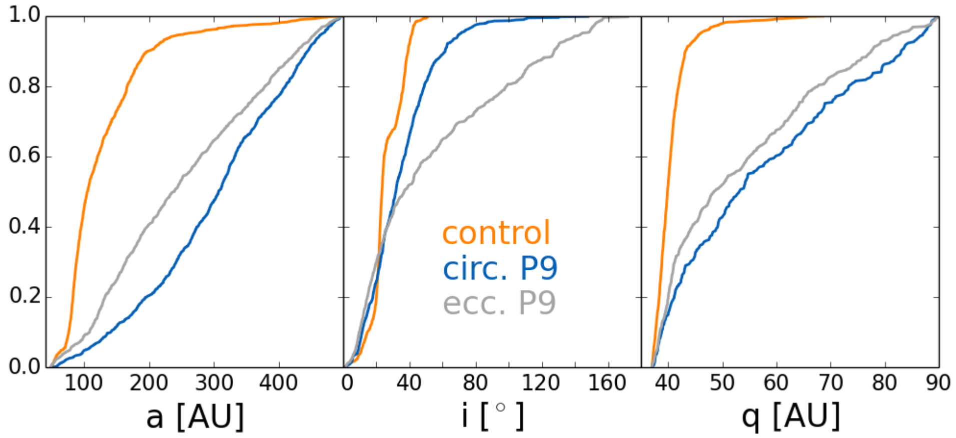

Figure 4.3: Cumulative histograms showing the intrinsic orbital distributions for moderate-a orbits in each of the three dynamical models, to the same minimum and maximum values in each parameter: semi-major axis a, inclination i, and pericenter distance q. The baseline Solar System dynamical model is shown in orange, the circular 9-planet dynamical model in blue and the eccentric 9-planet dynamical model in gray. Only test particles with $q > 37$ AU and $50 < a < 500$ AU are shown.

The strong differences between the three model distributions are immediately apparent in Figure 4.3. Both superearth dynamical models result in a more uniform distributions in a: $< 10\%$ of the surviving high-q population have orbits with $a <$

100 AU, while in the control dynamical model about 50% have orbits with $a < 100$ AU. The fraction of the intrinsic distributions with $a < 100$ AU is a clear diagnostic of the presence of a distant superearth. The control dynamical model has essentially no test particles with inclinations higher than ∼45°, while the circular superearth dynamical model has ∼20% of objects with $i > 45°$, and the eccentric superearth dynamical model has ∼40% of objects with $i > 45°$ and ∼20% of objects on retrograde orbits. The circular and eccentric superearth dynamical models are very similar to each other in q, lacking the $q <$40 AU concentration of the control dynamical model where the q-distribution is dominated solely by interactions with Neptune.

These dynamical models produce clear predictions for what the orbital distributions of the high-q population should look like in the absence of any observational biases. However, we are not able to detect all TNOs equally. In order to compare these models using present surveys, we must use a survey simulator (Section 4.4) to apply the known biases of the surveys to our simulated populations.

Figure 4.4 shows the biased distributions in six orbital parameters. Immediately notable is that the three dynamical models which differ strongly are, when biased by the surveys, nearly indistinguishable from each other. This underscores the peril of using TNOs at the fringe of detectability and where the discovery biases are substantial and complex to assess the underlying population. We confirmed that these biased distributions are consistent with currently published TNO detections from these surveys.

Because these surveys are all flux-limited, detectability of these objects drops sharply with distance (d), proportional d^{-4}. Due to this effect, as q increases, the probability of detection drops dramatically, and the bias towards detection of the numerous small and also lowest q objects becomes overwhelming. The flux bias effect completely overwhelms the superearth induced signature of a significant population with highly inclined orbits at high-q.

Using the survey simulator, we estimate that a deep wide-field, off-ecliptic survey of several thousand square degrees, sensitive to TNOs with $i > 30°$ and $q > 37$ AU, will be needed to distinguish between these dynamical models of the distant Solar System. In our survey set, only the HiLat survey (480 deg^2 to $m_g = 23.9$; Kavelaars et al., 2008) contained detections in this region of orbital phase space, and the three objects it provided were insufficient to make this test. In order to debias its detections to gain absolute populations and orbital element distributions, the crucial detection and tracking efficiencies as well as all pointings of a future, deeper, high-latitude survey must be published along with the detections.

4.4.2 A Distant Ninth Planet Requires a Much Larger High-q Population

The survey simulator draws a large number of undetectable, large q, TNOs before "detecting" the required number of simulated objects (in this case, 15, as that is the number of real detected TNOs in the four surveys inside this a/q cut). By keeping track of the number of drawn simulated objects, we measure the absolute number of objects required by a model to produce the same number of detections as in the observed sample, down to a given H_r magnitude limit. Using our control dynamical model with just the currently known planets, we find that the high-q, moderate-a population for $H_r < 9.0$ is 1.2×10^5 TNOs. The population required by including a circular superearth is almost three times larger, at 3×10^5, while an eccentric superearth requires nearly an order of magnitude larger high-q population than the control simulation, at 9×10^5. These population values all use the divot size distribution found to be most appropriate for the scattering population (Shankman et al., 2016). If we instead use a size distribution with a knee (similar to that favored by Fraser et al., 2014), this approximately doubles all three required populations, while the relative population ratios remain the same.

By assuming an albedo (0.04) and density (1 g/cm^3), we can use the size distribution to convert the population numbers to mass estimates. The control dynamical model requires a present-day disk of $q > 37$ AU, $50 < a < 500$ AU TNOs with a mass of 0.02 $M_\oplus$, while the circular superearth model requires a mass of 0.06 $M_\oplus$, and the eccentric superearth model requires a mass of 0.2 $M_\oplus$. For comparison, even the control model requires a mass that is larger than the entire classical Kuiper belt (0.01 $M_\oplus$; Fraser et al., 2014). It is important to note that current observations are rather insensitive to this high-q population (Section 4.4.1), so it is unknown whether these mass estimates violate any observational constraints. The possibility exists that a large high-q population could be hidden at the edge of observability.

4.5 Discussion and Conclusion

We find that a superearth on either a circular or eccentric orbit in the outer Solar System strongly affects the orbital distribution of the distant Kuiper belt ($q > 37$ AU and $50 < a < 500$ AU) when compared to a control dynamical model containing only the currently known planets. However, because flux-limited survey detections will always be dominated by the lowest q objects, the strong differences between the predicted distributions are undetectable in the well-characterized surveys we examined here.

In order to match observations, the predicted mass of this high-q population is 3× higher for a Solar System containing a circular superearth, and nearly 10× higher for an eccentric superearth. This is higher than other published estimates of the size of the population in this region, but we note that this high-q population is not well constrained by current observations and therefore the uncertainties are large.

The presence or absence of an additional superearth-mass planet also has important implications for the structure of the scattering TNO disk and inner Oort Cloud. We find that the fraction of test particles that end up in the Oort Cloud population ($q > 45$ AU and $a > 1000$ AU) is almost the same for each of the three surveys (∼3%), so the presence of a distant superearth does not appear to be an important dynamical barrier to Oort Cloud production (see Figure 4.2). The fraction of objects that end up in the high-q and moderate-a population ($q > 37$ AU, $50 < a < 500$ AU), however, is significantly different for the three simulations. With an eccentric superearth, the fraction is three times higher than the control simulation's value of 0.1% while a circular superearth produces a fraction that is nine times higher. These population ratios are largely beyond the current realm of detectability, but could provide an important diagnostic of our Solar System's true planetary architecture in the future when compared with other TNO populations.

A wide-field, relatively deep, off-ecliptic survey will have great power in constraining the presence or absence of an additional massive planet in our Solar System. These surveys must be meticulous about recording detection and tracking biases, and must take care not to preferentially lose high-inclination, large a/e TNOs due to tracking difficulties. In particular, since the full a and q distribution contains so much information, placing a constraint on the presence of a superearth requires tracking all large-a objects to high-quality orbits; this is expensive because getting a to converge for highly eccentric orbits requires many astrometric observations, over a long time period. Making sure that the survey is sensitive to TNOs with inclinations greater than 30° and pericenters outside the immediate dynamical dominance zone of Neptune ($q \gtrsim 37$ AU) is vital for distinguishing between the dynamical models presented in this work.

Acknowledgements

SML gratefully acknowledges support from the NRC-Canada Plaskett Fellowship. This research was supported by funding from the National Research Council of Canada and the National Science and Engineering Research Council of Canada. This research used the facilities of the Canadian Astronomy Data Centre and the Canadian Advanced Network for Astronomical Research operated by the National Research Council of Canada with the support of the Canadian Space Agency.

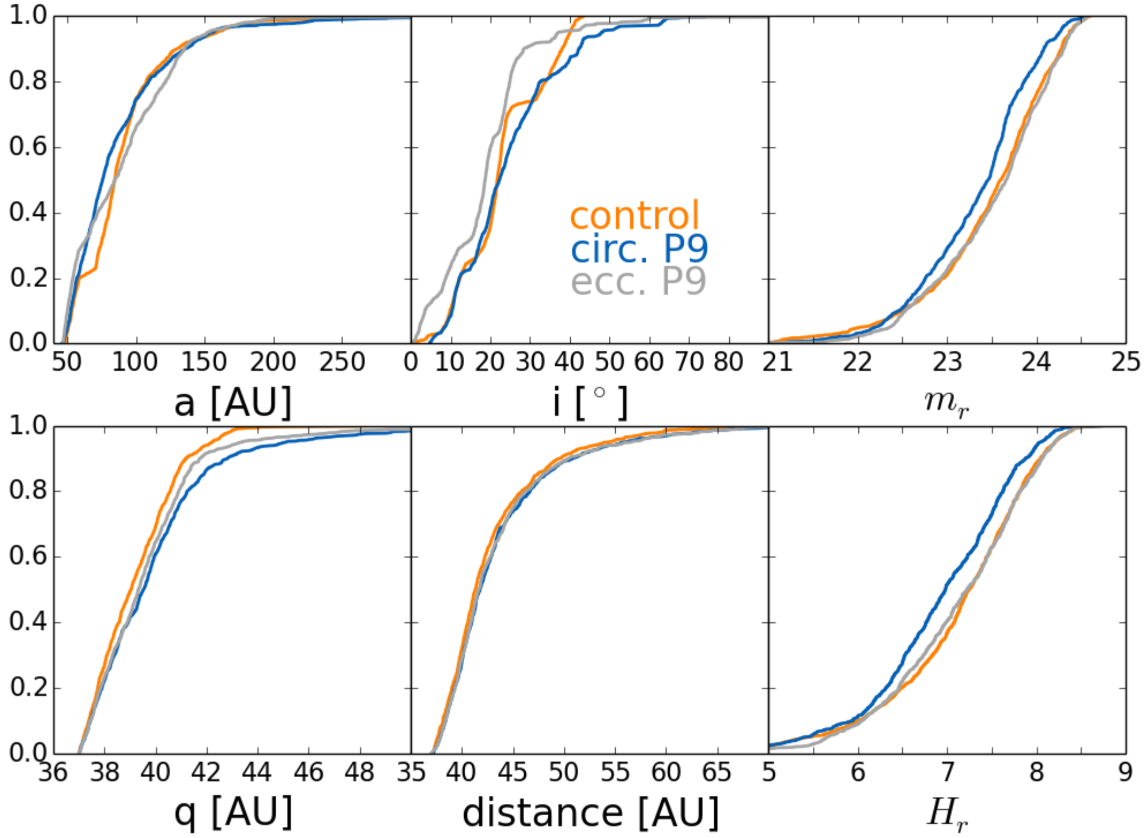

Figure 4.4: Cumulative histograms showing comparison between the three dynamical models biased by the survey simulator in semi-major axis a, inclination i, r-band magnitude m_r, pericenter distance q, distance at detection, and absolute r-band magnitude H_r. The standard Solar System dynamical model is shown in orange, and the 9-planet dynamical models are shown in blue and gray. Here we use the Shankman et al. (2016) divot size distribution, but a knee size distribution produces statistically and qualitatively indistinguishable results. Despite the huge differences in intrinsic distributions (Figure 4.3), after applying survey biases, the three dynamical models are indistinguishable from each other.

Chapter 5

Consequences of a distant massive planet on the large semi-major axis Trans-Neptunian Objects

Published as: C. Shankman, JJ. Kavelaars, S. Lawler, B. Gladman, and M. Bannister 2017 *AJ* 153 63

Available online here: http://iopscience.iop.org/article/10.3847/1538-3881/153/2/63/meta

5.1 Abstract

We explore the distant giant planet hypothesis by integrating the large semi-major axis, large pericenter Trans-Neptunian Objects (TNOs) in the presence of the giant planets and an external perturber whose orbit is consistent with the proposed distant, eccentric, and inclined giant planet, so called planet 9. We find that TNOs with semi-major axes greater than 250 au experience some longitude of perihelion shepherding, but that a generic outcome of such evolutions is that the TNOs evolve to larger pericenter orbits, and commonly get raised to retrograde inclinations. This pericenter and inclination evolution requires a massive disk of TNOs (tens of $M_\oplus$) in order to explain the detection of the known sample today. Some of the highly inclined orbits produced by the examined perturbers will be inside of the orbital parameter space probed by prior surveys, implying a missing signature of the 9th planet scenario. The distant giant planet scenarios explored in this work do not reproduce the observed signal of simultaneous clustering in argument of pericenter, longitude of the ascending

node, and longitude of perihelion in the region of the known TNOs.

5.2 Introduction

In Solar System studies, the observation of unexpected orbital behavior has been used to further our understanding of both physics and the composition of the Solar System. Two exemplary successes of this process can be found in the prediction of the existence of Neptune from observing the evolving orbit of Uranus (Le Verrier, 1846), and the confirmation of General Relativity through its ability to explain the precession of Mercury's orbit (Le Verrier, 1859; Einstein, 1916). This pattern repeats itself in the outer Solar System today as we discover new mysteries in the Trans-Neptunian Object (TNO) population.

The distant perihelion of 2001 CR_{105} (Gladman et al., 2002) demonstrated that some TNOs inhabit the space beyond the domain that is dominated by the gravitational influence of Neptune. With a large semi-major axis a of 226 astronomical units (au) and a pericenter q of 44 au, well beyond the $q \lesssim 37$ au active influence of Neptune (Lykawka & Mukai, 2007b; Gladman et al., 2008), 2001 CR_{105} required a new dynamical process to emplace TNOs on orbits so separated from the influence of the giant planets. Gladman et al. (2002) explore various possible formation scenarios for 2001 CR_{105} including a fossilized disk, a passing star, the presence of a small (lunar to Mars sized) planet beyond the orbit of Neptune, and others argue that 2001 CR_{105} can be emplaced on its orbit by a complex path of planetary migration and resonance capture, but only for objects with $a < 260$ au (Gomes, 2003; Gomes et al., 2005). The discovery of 2001 CR_{105} was followed by surveys finding other TNOs with orbits outside the gravitational domain of Neptune (now numbering in the tens) that have revealed unexpected and difficult to explain structure in the outer Solar System.

With the discovery of (90377) Sedna (Brown et al., 2004), an even more extreme orbit space was revealed. Sedna, with its q at 76 au and a of 500 au, is not dynamically coupled to the giant planets nor to galactic tides. It is difficult to form planetesimals at such a large distance given current models of planetesimal formation, and therefore the current orbits of these detached TNOs requires some dynamical interaction (ongoing or long past) to have emplaced them on such orbits. Theories for emplacement of TNOs on large-q orbits have included an additional planet in the Solar System (e.g. Gladman et al., 2002; Brown et al., 2004; Gomes et al., 2006; Soares & Gomes, 2013), stellar flybys (e.g. Ida et al., 2000; Kenyon & Bromley, 2004; Morbidelli & Levison, 2004; Kaib et al., 2011b; Soares & Gomes, 2013; Brasser & Schwamb, 2015) and ejected rogue planets (e.g. Thommes et al., 2002; Gladman & Chan, 2006). These discoveries have continued, with one new extreme orbit TNO discovered every few years (e.g. 2004 VN_{112}, Becker et al. (2008), and 2010 GB_{174}, Chen et al. (2013)).

In 2014, Trujillo & Sheppard (2014) reported the discovery of another large pericenter TNO, 2012 VP_{113}, with $q \simeq 80$. Trujillo & Sheppard (2014) also noted a clustering (i.e. apparent grouping in the observed sample) of pericenter arguments ω near $0°$ for all of the known TNOs having $a > 150$ au and $q > 30$ au. There are known detection biases for discovering objects at their pericenters and in the ecliptic plane, which could explain an enhancement of detections of objects with $\omega = 180°$ versus $\omega = 0°$, however there have been no TNOs detected with ω near $180°$. As of this writing, there has been no published demonstrations that the lack of $\omega = 180°$ TNOs results from an observation bias, nor has there been a demonstration that these detections should be free from such an observation bias. Trujillo & Sheppard (2014) suggest that the clustering of TNOs with $\omega = 0°$ might be explainable through a dynamical interaction with a massive perturber on a 250 au orbit (required to maintain the observed clustering over time); they posit the existence of a 9th planet of super-Earth-mass size in the outer Solar System as the cause of the observed ω clustering, but do not demonstrate a particular dynamical pathway to cause clustering around $\omega = 0$ lasting until the present day.

In 2016, Batygin & Brown (2016a) re-examined the $a > 150$ au TNOs, reporting that the large-a TNOs that are not dynamically interacting with Neptune show clustering not only in ω but also in longitude of the ascending node Ω and thus also in longitude of pericenter, $\varpi = \omega + \Omega$ (see Figure 5.1). A 9th planet (henceforth P9) with $a = 700$ au, eccentricity $e = 0.6$, inclination $i = 30°$ and a mass of at least 10 Earth-masses [1] is proposed as the cause of the observed confinement in ϖ. They demonstrate analytically and with numerical simulations that their proposed P9 can produce ϖ confinement for the age of the Solar System in test particles with $a > 250$ au and ω and Ω confinement for test particles with $a > 500$ au. They also find that an inclined P9 produces highly inclined distant TNOs and propose that such a planet could explain the origin of the known large-a TNOs with i between $60°$ and $150°$ (e.g. Drac 2008 KV_{42}, Gladman et al. (2009b)) whose formation was not securely identified (Elliot et al., 2005; Gladman et al., 2009b; Chen et al., 2016),

---

[1] Any distant planet that is interior to the Oort Cloud must have a mass less than M_{Saturn} to be consistent with a non-detection in the all-sky WISE survey(Luhman, 2014)

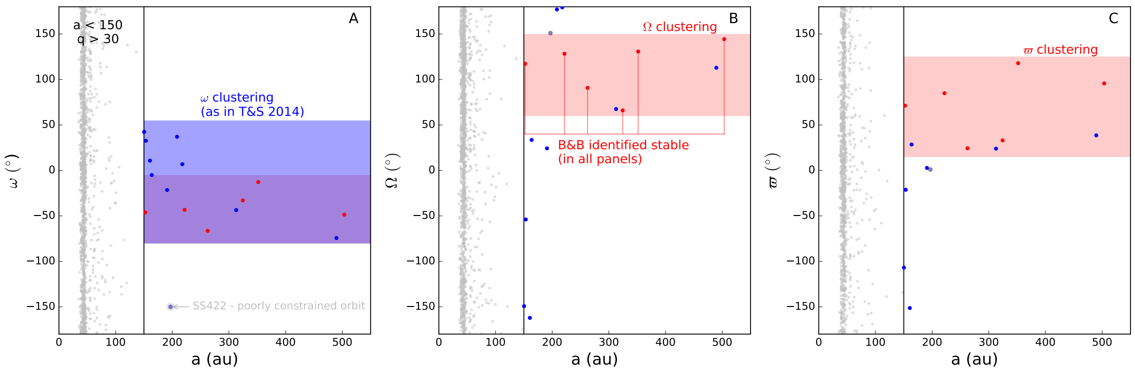

Figure 5.1: All TNOs with $q > 30$ from the Minor Planet Center (MPC) database as of 2016 May 3. TNOs with $a < 150$ au are plotted in grey, the Batygin & Brown (2016a) identified stable TNOs are plotted in red (Table 5.3), and the remaining $a > 150$ au TNOs are plotted in blue (Table 5.1). Panel **A** plots argument of pericenter ω vs semi-major axis a, panel **B** plots longitude of the ascending node Ω vs semi-major axis a, and panel **C** plots longitude of perihelion ϖ vs semi-major axis a. Panel **A** highlights a clustering in ω as first reported in Trujillo & Sheppard (2014), where panels **B** and **C** show Ω and ϖ clustering as reported in Batygin & Brown (2016a). The red and blue bands guide the eye to regions of clustering. 2003 SS_{422} was not included in the analyses of Trujillo & Sheppard (2014) or Batygin & Brown (2016a), possibly due to its large a uncertainty ($\Delta a \sim 50$ au); 2003 SS_{422} is plotted in light blue in all panels and indicated in panel **A**.

but has been explained by a distant planet (Gomes et al., 2015). These arguments launched a flurry of discussions and studies on the origins, location and implications of a ninth planet. The studies have covered formation and capture scenarios (Bromley & Kenyon, 2016; Cowan et al., 2016; Kenyon & Bromley, 2016; Li & Adams, 2016; Mustill et al., 2016), constraints on the location, detectability and physical properties of P9 (Brown & Batygin, 2016; de la Fuente Marcos & de la Fuente Marcos, 2016a,b; Fienga et al., 2016; Fortney et al., 2016; Ginzburg et al., 2016; Holman & Payne, 2016b,a; Linder & Mordasini, 2016; Philippov & Chobanu, 2016; Toth, 2016; Veras, 2016), the dynamical implications of P9 in the Solar System (de la Fuente Marcos et al., 2016; Lawler et al., 2016), P9 producing inclined TNOs (Batygin & Brown, 2016b), resonances and P9 (Beust, 2016; Malhotra et al., 2016), a dark matter P9 (Sivaram et al., 2016), and impacts of P9 on the Sun's obliquity (Bailey et al., 2016; Lai, 2016).

The studies to date have primarily focused on the formation and detection of P9, with few publications examining the impact on the observed TNO populations of a massive perturber in the distant Solar System. Lawler et al. (2016) model the emplacement of the scattering and detached TNO populations in the presence of a super-earth planet beyond 200 au. They find that such a planet sculpts distinctly different e and i distributions within the scattered and detached TNOs, but that this effect is not detectable in well-characterized, published surveys to date due to the strong flux bias at those distances. de la Fuente Marcos et al. (2016) performed numerical integrations of the six known $a > 250$ au TNOs (see Table 5.3) in the presence of the four giant planets and the Batygin & Brown (2016a) P9. Integrating these TNOs for 200 Myr, de la Fuente Marcos et al. (2016) find that P9 may destabilize the orbits of several of these TNOs on timescales of dozens of Myr and can result in their ejection from the Solar System. These two works are the first to study the implications of P9 on observed TNO populations, but to date there has been no work examining the implications on the detectability of the large-a TNOs that were used to infer the existence of P9.

In this work we study the dynamical impact of P9 on the known large-a, large-q TNOs (Table 5.1). Performing a set of n-body simulations, we examine the implications for the detectability of these TNOs and the evolution of their ω, Ω, and ϖ angles to assess whether the proposed P9 reproduces the original observed clustering signal used to infer its existence.

5.3 Methods

We test the P9 hypothesis by supposing the existence of such a planet in the Solar System today and exploring the implications for the large-a TNOs. We perform a set of n-body integrations of the large-a TNOs (see Figure 5.1, Table 5.1) in the presence of the giant planets and a candidate P9, examining the implications of the presence of a massive perturber through the orbital evolution of the TNOs. Batygin & Brown (2016a) report possible a, e, i, ω, and Ω values for P9 (see Table 5.4) and assume a mass of around 10 Earth-masses. The mean anomaly $\mathcal{M}$ of P9 is not well-constrained by observations. A more distant P9 (i.e. $\mathcal{M}$ near 180°) is more difficult to detect, and thus more consistent with the current non-detection. Resonance confinement is not the proposed mechanism for ϖ shepherding between P9 and the large-a TNOs and thus the choice of $\mathcal{M}$ does not affect the confinement; we therefore assign P9 $\mathcal{M} = 180°$. Batygin & Brown (2016a) propose an $i = 30°$ for P9, motivated by this configuration's ability to produce highly inclined TNOs. We test the sensitivity of our analysis to this choice of inclination by also examining scenarios with P9 at lower inclinations of 15° and 0°. Table 5.4 lists the orbital elements and mass for the three P9 configurations examined in this work; these parameters are consistent with current studies on the observable constraints (Brown & Batygin, 2016; Fienga et al., 2016; Holman & Payne, 2016b,a). We also perform a control simulation without a P9.

Trujillo & Sheppard (2014) note an ω-clustering for TNOs with $a > 150$ au and $q > 30$ au and Batygin & Brown (2016a) note that a subset of these ($a > 250$ au and $q > 30$ au) cluster in Ω and ϖ. The choice of a semi-major axis boundary at 150 au has not been given any physical motivation, however there is an apparent clustering of ω beyond this $a > 150$ au threshold (Figure 5.1 panel A) and so we continue this approach and select all of the TNOs satisfying $a > 150$ au and $q > 30$ au as the sample for this study[2] for consistency and reproducibility with prior studies (Trujillo & Sheppard, 2014; Batygin & Brown, 2016a). Table 5.1 lists this set of TNOs with their orbital elements and absolute magnitudes H as reported by the MPC.

We perform n-body simulations with the MERCURY6 (Chambers, 1999) suite. The hybrid symplectic/Bulirsch-Stoer algorithm, which balances integration speed with modeling close encounters, was used with a base time step of 0.5 years [3] and all simulations were run for 4 Gyr [4]. An ejection distance of 10 000 au is used. While TNOs that go beyond $a = 10\ 000$ au can survive in the Oort Cloud, once they go beyond this distance in our simulation, they are no longer pertinent to the discussions in this work and so are removed for computational expediency. Galactic tides[5] and stellar flybys are not included in the simulation.

The giant planets and TNOs in Table 5.1 were added to the simulation with orbital elements taken from the NASA Horizons database[6] for the date of 2016 January 1 (JD 2457388.5). As N-body dynamics are inherently chaotic, we examine the evolution of each TNO through the evolution of a set of 60 clones created by sampling each object's orbit uncertainties. Orbit uncertainties for each TNO were taken from the JPL Small-body Database[7] (Table 5.2) and clones were generated in one of two ways:

---

[2] The sample was selected in May 2016.

[3] 0.5 years is less than $\frac{1}{20}$th of Jupiter's orbital period that sets the shortest dynamical timescale in the simulation.

[4] An accuracy parameter of 1E-12 was used. Simulations consistently had a fractional energy change due to the integrator of order 3E-07 and a fractional angular momentum change of 9E-10.

[5] While tides can affect the eccentricity of TNOs on Sedna-like orbits by a few percent (Veras & Evans, 2013), the effects of a giant planet in this TNO region can change eccentricities by tens of percent.

[6] http://ssd.jpl.nasa.gov/horizons.cgi

[7] http://ssd.jpl.nasa.gov/sbdb.cgi

MPC Designation	a **(au)**	e	q **(au)**	i **(°)**	ω (°)	Ω (°)	M **(°)**	H_v
Sedna	499.08	0.85	76.04	11.9	311.5	144.5	358.1	1.6
2007 TG_{422}	482.4	0.93	35.57	18.6	285.8	112.9	0.4	6.2
2010 GB_{174}	369.73	0.87	48.76	21.5	347.8	130.6	3.3	6.5
2013 RF_{98}	325.1	0.89	36.29	29.6	316.5	67.6	0.1	8.6
2004 VN_{112}	317.71	0.85	47.32	25.6	327.1	66.0	0.4	6.4
2012 VP_{113}	260.81	0.69	80.27	24.1	292.8	90.8	3.3	4.0
2001 FP_{185}	226.86	0.85	34.26	30.8	7.0	179.3	1.3	6.2
2000 CR_{105}	226.14	0.8	44.29	22.7	317.2	128.3	5.4	6.3
2002 GB_{32}	217.9	0.84	35.34	14.2	37.0	177.0	0.3	7.8
2003 SS_{422}	196.44	0.8	39.37	16.8	210.8	151.1	359.2	7.1
2007 VJ_{305}	187.74	0.81	35.18	12.0	338.3	24.4	1.5	6.6
2003 HB_{57}	165.36	0.77	38.1	15.5	10.9	197.8	1.3	7.4
2015 SO_{20}	162.02	0.8	33.16	23.4	354.9	33.6	359.8	6.4
2013 GP_{136}	153.33	0.73	41.11	33.5	42.2	210.7	356.2	6.6
2010 VZ_{98}	151.89	0.77	34.32	4.5	313.9	117.4	357.8	5.1
2005 RH_{52}	151.21	0.74	38.98	20.5	32.3	306.1	2.6	7.8

Table 5.1: All TNOs with $a > 150$ au and $q > 30$ au in the MPC database. Data downloaded on 2016 May 3. J2000 heliocentric orbital elements and absolute magnitudes are as reported by the MPC.

a) if the a uncertainty was small ($\Delta\, a < 0.5$ au), 60 orbits within the a, e, i, ω, Ω and true anomaly uncertainties were randomly and uniformly sampled; **b)** if $\Delta a > 0.5$ au, three clusters of orbits were generated - one cluster of 20 orbits at each of the a, q extremes and one cluster of 20 orbits around the nominal orbit. For clarity we emphasize that in our simulation all TNO and planet orbits and uncertainties are taken from the NASA Horizons database and not the MPC; Table 5.1 lists the Minor Planet Center (MPC) elements and magnitudes as a convenient reference. We test three cases of P9 inclinations (Table 5.4) and one control simulation with the 4 giant planets. Each of our simulations thus includes 4 or 5 planets and 960 test particles; each was integrated for the 4 Gyr age of the Solar System [8].

---

[8] Throughout, by "age of the Solar System" we mean that we conduct a 4 Gyr integration, which demonstrates the behavior of the system for a length of time approximately equivalent to the age of the Solar System.

MPC Designation	Δ a **(au)**	Δ e	Δ i (°)	Δ ω (°)	Δ Ω (°)
Sedna	0.78	2.39e-4	3.0416e-05	1.34e-2	1.60e-3
2007 TG_{422}	3.45	5.24e-4	2.45e-4	2.93e-2	1.74e-3
2010 GB_{174}	28.30	1.10e-2	5.42e-3	3.79e-1	2.09e-2
2013 RF_{98}	36.67	1.46e-2	7.77e-2	5.54	1.26e-1
2004 VN_{112}	1.07	4.85e-4	3.69e-4	1.04e-2	6.79e-4
2012 VP_{113}	7.13	1.08e-2	4.15e-3	2.40	9.96e-3
2001 FP_{185}	0.32	2.10e-4	4.74e-4	1.19e-2	1.05e-4
2000 CR_{105}	0.53	4.54e-4	4.01e-4	9.88e-3	2.16e-4
2002 GB_{32}	0.68	4.92e-4	2.27e-4	3.82e-3	3.53e-4
2003 SS_{422}	47.83	5.56e-2	5.89e-2	17.18	6.98e-2
2007 VJ_{305}	0.55	5.25e-4	8.47e-4	4.58e-2	1.31e-3
2003 HB_{57}	0.58	7.73e-4	9.66e-4	5.48e-2	3.96e-4
2015 SO_{20}	0.13	1.62e-4	6.24e-4	2.18e-2	2.84e-4
2013 GP_{136}	0.57	1.17e-3	1.30e-3	1.14e-1	1.61e-4
2010 VZ_{98}	0.15	2.10e-4	6.11e-05	7.58e-3	3.57e-3
2005 RH_{52}	0.19	2.91e-4	5.90e-4	6.84e-2	1.48e-3

Table 5.2: Uncertainties in orbital parameters for all TNOs in Table 5.1. 1-σ uncertainties taken from the JPL small-body database(http://ssd.jpl.nasa.gov/sbdb.cgi). All values are J2000 heliocentric, generated for the JD 2457600.5 (2016 Jul 31)

$a > 250$ au	Sedna	2010 GB_{174}	2004 VN_{112}	2012 VP_{113}	2007 TG_{422}	2013 RF_{98}
Batygin & Brown (2016a) identified stable	Sedna	2010 GB_{174}	2004 VN_{112}	2012 VP_{113}	2000 CR_{105}	2010 VZ_{98}

Table 5.3: Examined TNO groups .

P9	a **(au)**	e	q **(au)**	i (°)	ω (°)	Ω (°)	M (°)	**Mass**
P9 (Batygin & Brown, 2016a)	700	0.6	280	30	150	100	180	10 $M_\oplus$
P9 (moderate i)	700	0.6	280	15	150	100	180	10 $M_\oplus$
P9 (low i)	700	0.6	280	0	-	-	180	10 $M_\oplus$

Table 5.4: P9 configurations tested. With an inclination of 0°, ω and Ω become undefined, but ϖ remains 150°.

5.4 Results

5.4.1 Signal in Angle Clustering

P9 was proposed to explain the apparent clustering of one or more of the angles that determine an orbit's orientation. Here we examine the shepherding of ω, Ω, and ϖ through our dynamical simulations of the large-a TNOs. We focus our discussion of the results on the nominal P9 case with an inclination of 30°, checking that our results hold for different choices of P9 inclination (see below).

Here we examine the evolution of two of the TNOs in the sample as examples of the evolutions seen in our simulations[9]. Figure 5.2 shows the orbital evolution for all of the clones of Sedna. The majority of Sedna clones undergo ϖ *shepherding* (i.e. driven confinement in a band) throughout the 4 Gyr simulation (Figure 5.2 panel G), remaining in the region of the detected sample (red band). The orbital evolution of 2010 GB_{174} is plotted in Figure 5.3, showing that 2010 GB_{174} undergoes similar ϖ shepherding. Of the 16 TNOs in the sample (Table 5.1), only six TNOs undergo ϖ shepherding. These confinements last for periods ranging from hundreds of Myr to 4 Gyr (e.g. see Figures 5.2 and 5.3 panel **G**). We find that only TNOs with $a > 250$ au (see Table 5.3) undergo ϖ shepherding. The analysis of Batygin & Brown (2016a) highlights both the set of $a > 250$ au TNOs and six stable TNOs (see Table 5.3). We find that for TNOs with q beyond Neptune, a large semi-major axis is the determining factor in ϖ shepherding; all of the clones of the $a > 250$ au TNOs experience shepherding, however we find that two of the Batygin & Brown (2016a) identified stable TNOs do not undergo this shepherding. A massive, eccentric, external perturber generically drives q down to Neptune coupling (Figures 5.2 and 5.3 panel C), which then shuts off ϖ shepherding.

As a necessary implicit condition of ϖ shepherding, P9 also drives the evolution of ω and Ω (Figures 5.2 and 5.3 panels E and F). Clones for all six of the $a > 250$ au TNOs (Table 5.3) undergo ϖ shepherding, and thus experience correlated ω and Ω evolution, but only two (VP_{113} & GB_{174}) experience shepherding of ω and Ω, while the rest drift in a pattern that is mostly consistent with long-term circulation at a rate unique to each TNO. Whether their ω and Ω are shepherded or circulating, the clones experience ϖ confinement in the same region.

Figure 5.4 explores the implication of this evolution on the initial signal used

---

[9] For plots of all TNOs across all simulations, see DOI: https://doi.org/10.5281/zenodo.168604

to infer the existence of P9: simultaneous ω, Ω, and ϖ clustering. The clones in Figure 5.4 are color coded red if they are in the region of ϖ confinement at 2 Gyr [10] into the simulation (panel C) and blue otherwise. Panels A and B show that clones in the ϖ confinement band can occupy all values in ω and Ω. This is consistent with the result that the explored distant massive planets do not shepherd ω nor Ω in the region of the observed TNOs (Batygin & Brown, 2016a; Lawler et al., 2016). Panel C shows that while some clones experience ϖ shepherding (Figures 5.2 and 5.3)), the influence of P9 does not sculpt a dominant band of confined ϖ values. Figure 5.5 presents an alternative visualization of these results. The lack of sculpting implies that there should be a large number of detectable TNOs at all values of ω, Ω and ϖ.

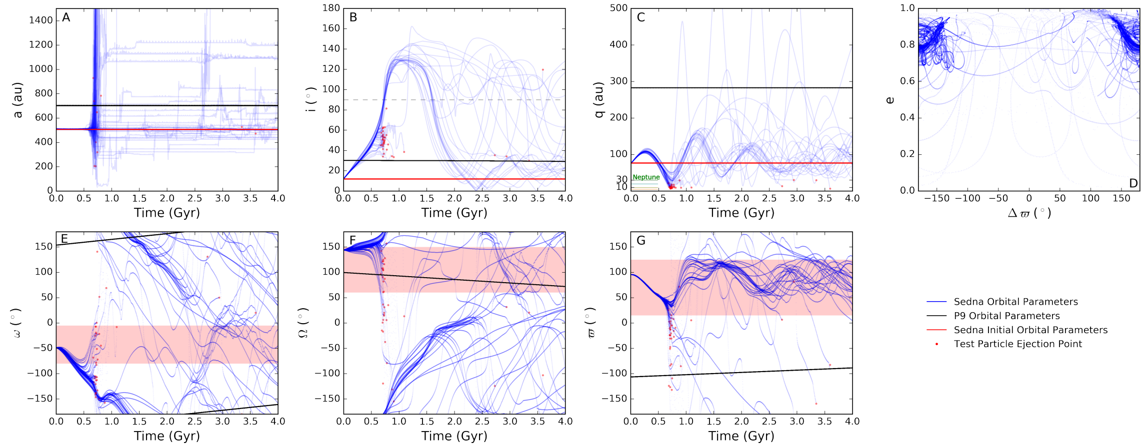

Figure 5.2: The orbital evolution for the barycentric orbital elements of the 60 clones of Sedna across the 4 Gyr simulation. The time evolution of clones are plotted in blue in all panels. Panel **D** plots the $\varpi_{\rm P9} - \varpi_{\rm clone}$ vs e, which shows the secular interaction between the clones and P9. The red horizontal line in panels **A**, **B**, and **C** mark the present-day observed values for Sedna's orbital elements plotted in those panels. The black line plots the orbital evolution of P9. Red circles mark the ejection point of a clone from the simulation ($a >$ 10 000 au or collision with the Sun). The red bands in panels **E**, **F**, and **G** mark the region of confinement in the real TNOs for ω, Ω, and ϖ, respectively (as in Figure 5.1). The dashed gray line in panel **B** indicates an inclination of 90°. The orbits of the giant planets are plotted in Panel **C**, showing when clones are driven into giant planet crossing orbits. The feature in panel **A** near 0.75 Gyr results from strong scattering encounters between the test particles and the giant planets, which can be seen in panel **C**.

---

[10] 2 Gyrs is taken as a representative snapshot for visualization, but the results does not depend on epoch choice.

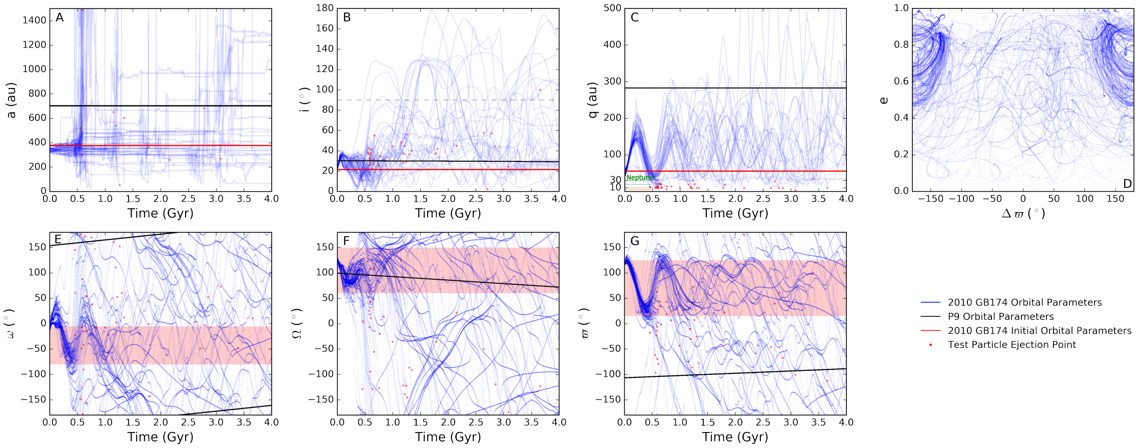

Figure 5.3: The orbital evolution for the 60 clones of 2010 GB$_{174}$ across the 4 Gyr simulation. Line styles and panels are as described in Figure 5.2.

5.4.2 Orbital Evolution

A 10 M$_\oplus$ planet with its q at 280 au has a significant effect on the orbital evolution of the TNOs in our sample. In their explorations of the $a > 250$ au TNOs, de la Fuente Marcos et al. (2016) demonstrate that P9 can destabilize the orbit of these TNOs on short timescales ($<$ 200 Myr); we extend the sample to include all TNOs with $a > 150$ au and $q > 30$ au, and we also extend simulations to the age of the Solar System, revealing important structure in the i and q evolution of these TNOs.

Perihelia Cycling

Gravitational interactions with P9 raise and lower the pericentres of all of the clones in the sample, lowering some clones down into Neptune, or even Jupiter, crossing orbits or raising them out to hundreds of au (e.g. see Figures 5.2, 5.3). All of the ϖ-shepherded clones undergo q oscillations, which occur on roughly the same timescale as their ϖ oscillations (see Figures 5.2 and 5.3 panel C). With q cycled between hundreds of au and tens of au, the idea of a gap in overall distribution of TNO perihelia in the 50 - 70 au range (Trujillo & Sheppard, 2014) is incompatible with the P9 hypothesis. The cycling q affects the stability of the clones as they are pushed into planet-crossing orbits, and thus affects their survivability on Gyr timescales. This increases the likelihood of ejection for the clones of TNOs that already currently interact with Neptune, and introduces instability for those which are presently on Neptune decoupled orbits (e.g. Sedna, 2012 VP113). Table 5.5 gives the fraction of

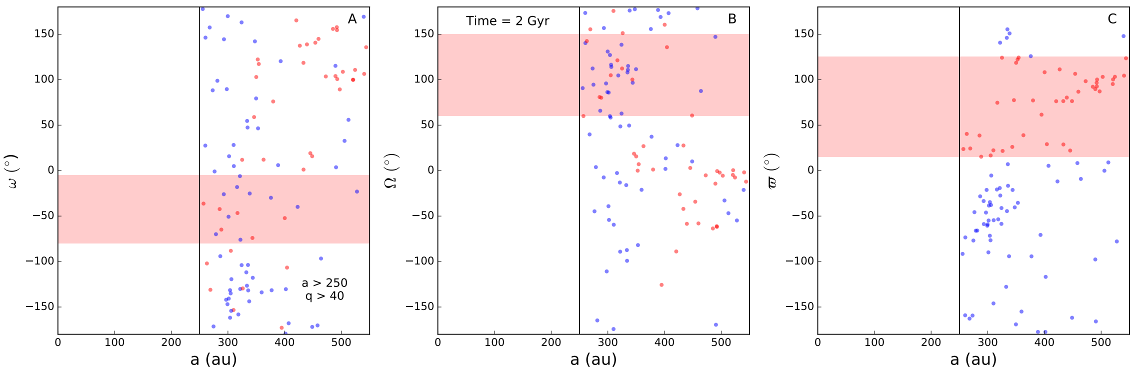

Figure 5.4: ω, Ω, and ϖ vs a for all clones not strongly interacting with Neptune ($q > 40$) and with a semi-major axis in the region of ϖ shepherding ($a > 250$ au) at 2 Gyr into the simulation (choice of epoch does not affect the result). Clones with ϖ values that are in the observed TNO ϖ clustering band are colored red in all panels, otherwise clones are plotted in blue. Panels **A**, **B**, and **C** demonstrate that P9 does not sculpt ω, Ω nor ϖ in a restricted range as seen in the observed sample (Figure 5.1). Panels **A** and **B** demonstrate that for ϖ shepherded clones, P9 does not simultaneously shepherd ω and Ω - this is also visible by comparison of panels E and F in Figures 5.2 and 5.3.

	% Ejected			
Designation	**30°**	**15°**	**0°**	**no P9**
Sedna	63	37	7	0
2007 TG_{422}	67	95	82	88
2010 GB_{174}	63	60	53	8
2013 RF_{98}	93	93	90	52
2004 VN_{112}	47	62	62	0
2012 VP_{113}	77	52	75	0
2001 FP_{185}	90	82	78	63
2000 CR_{105}	75	63	53	0
2002 GB_{32}	88	85	83	82
2003 SS_{422}	82	83	77	42
2007 VJ_{305}	82	88	88	73
2003 HB_{57}	70	62	65	28
2015 SO_{20}	75	82	85	88
2013 GP_{136}	33	25	10	10
2010 VZ_{98}	68	93	90	93
2005 RH_{52}	63	40	38	17

Table 5.5: Fraction of clones ejected during the simulation for the different P9 inclinations tested. The clones sample the range around plausible orbits for each TNO, but are not constructed to represent the possible orbits given the ephemerides. For this reason, this table should not be interpreted as giving the stability for the actual orbit of the TNOs in the sample.

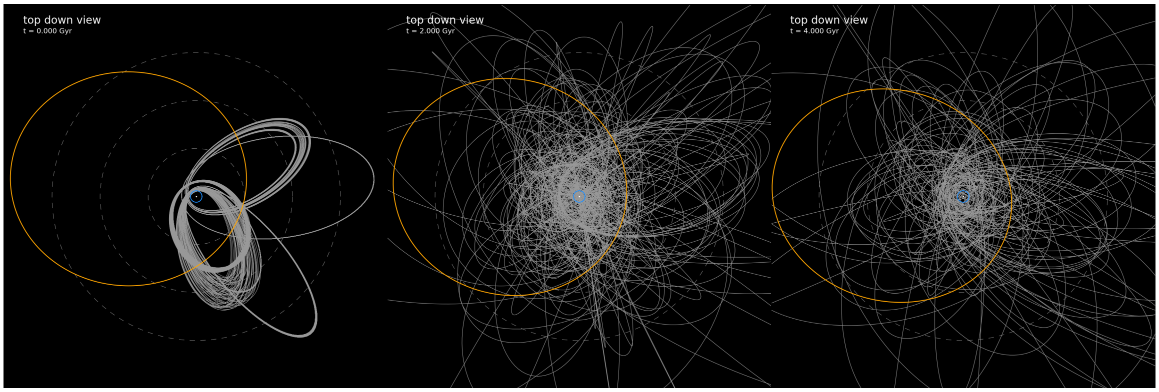

Figure 5.5: This figure is available online as an animation. The 4 Gyr simulation is displayed in a 49 second animation that shows how the orbits of the clones for the $a >$ 250 au TNOs (Table 5.3) evolve throughout the simulation. The print publication shows three image stills representing the start (0 Gyr), middle (2 Gyr), and end (4 Gyr) of the simulation. The dashed grey circles indicate distances of 250 au, 500 au, and 750 au. The blue circle marks the orbit of Neptune, the orange ellipse marks the orbit of the proposed distant massive planet, and the light grey ellipses show the orbits of the 60 clones for each of the six $a >$ 250 au TNOs. At the start of the simulation, all of the TNO orbits are clustered in physical space. As the simulation progresses, the orbits shear out and cover all angles. This provides a visual representation of the result we find - that P9 does not sculpt a confined alignment of orbits, even with the alignment present in the starting conditions.

clones ejected for each TNO in our sample across the four simulations performed. In contrast, the cycling to high values reduces the detectability of the clones. This then requires a larger than previously expected reservoir of large-a TNOs to explain the detection of the presently observed sample.

Sedna Population Estimate

We examine the implications for the detection of Sedna (the most massive of the known $a > 150$ au TNOs) in detail as an example of the effects P9 induces on q and i evolution on the large-a TNOs. Of the 60 clones of Sedna, 63% of the clones are ejected during the simulation (see Table 5.5). For the clones of Sedna that were not ejected, each spent on average $\sim$ 45% of the 4 Gyr simulation with q beyond the limit of detectability (of Sedna's discovery survey) due to q raising, implying a large population of undetectable large-a Sedna-like TNOs. As Sedna clones spend on average $\sim$ 45% of the simulation with q beyond the detection limit, roughly one half of the population must be on completely undetectable orbits today.

The shape of an orbit, which sets the fraction of the orbit inside the detectable volume of surveys, affects the expected number of TNOs in the population that are required to explain the detected sample. The detection of a TNO like Sedna which is on such large-a orbit, where most of the orbit lies beyond a detection threshold, implies that there must be many TNOs on similar orbits in order for it to be probable to have detected Sedna near its pericenter. Estimates of the size of these populations are regularly computed by asking what fraction of the time each TNO spends in an observable part of its orbit, which then gives the number of TNOs required for the expected detection of one object (as was done for Sedna in Brown et al. (2004); Schwamb et al. (2009)). We examine all of the clones of Sedna, at all time points in the simulation, and compute the population estimate required for the detection of those clones that have q within the detection threshold. While detectable, the Sedna clones require a population of TNOs on their orbit ranging from tens to, at times, the high thousands. We find a mean population estimate of $\sim$ 80 Sedna-sized objects (across all clones and all time steps) are required for the detection of Sedna. This estimate is double the best estimate for the Sedna population (Schwamb et al., 2009) but within the 1 σ upper limit for their size of the Sedna population. We combine our mean population estimate (80) with our findings that less than half of the clones of Sedna survive, and that surviving clones are only visible during half of the 4 Gyr simulation. In the P9 scenario, the single detection of Sedna today requires a mass of 6-24 $M_\oplus$ from the ensemble of Sedna-like TNOs (down to absolute magnitude[11] $H_r = 8$). This is more then an order of magnitude greater than the mass estimate required for the case of no P9.

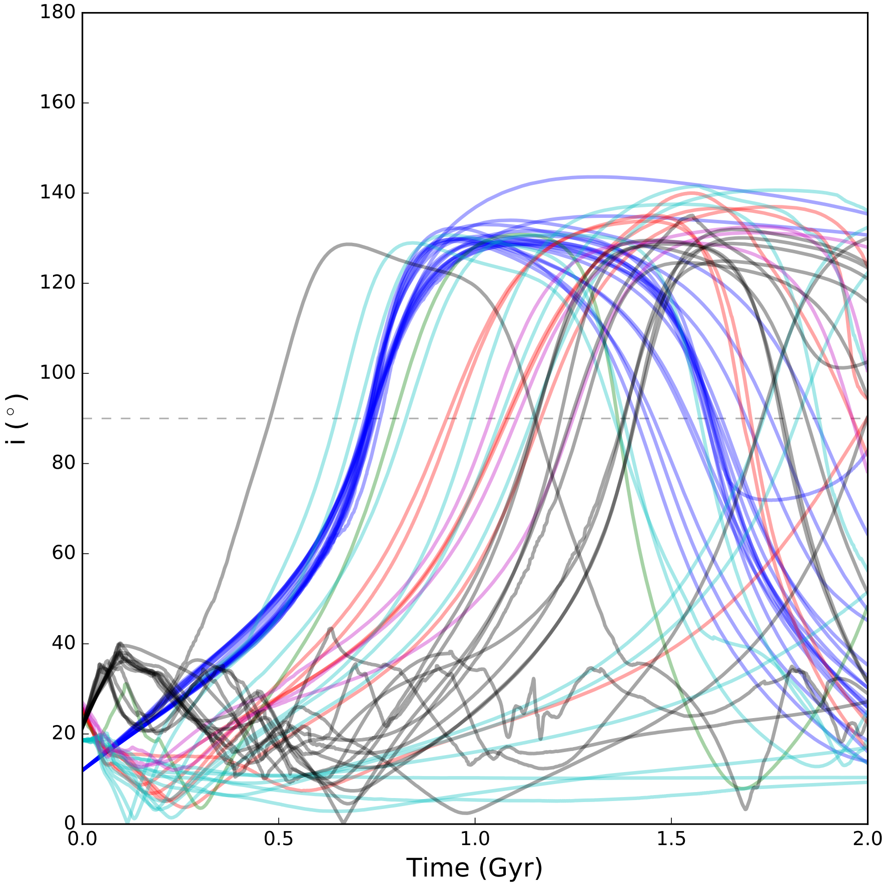

Figure 5.6: The i-evolution for all clones in our simulation that undergo ϖ shepherding for the first 2 Gyr. Each color represents clones from one of the six $a > 250$ au TNOs (Table 5.3). A dashed grey line marks $i = 90°$. The color coding serves to demonstrate that clones of each TNO undergo the same generic evolution of i cycling, which goes through extreme and retrograde values. Raising inclinations through retrograde values is a generic feature of the dynamical mechanism that causes ϖ shepherding.

---

[11] The absolute magnitude, H, distribution transitions to a different form faint of $H_r = 8$, which is diameter $D = 60$ km for 16% albedo. A single slope absolute magnitude distribution with a slopes of 0.8 and 0.9 were used to determine the range of mass estimates. These slopes are consistent with the measurements of other TNO populations and the TAOS limit on the Sedna population (Wang et al., 2009) An albedo of 16% and density of 1 g/cm^3 were used for the mass estimates.

Inclination Raising

Perturbations from P9 raise and lower the inclinations of all TNOs in the sample. Figures 5.2 and 5.3 panel B show that, on Gyr timescales, P9 raises the inclination, even into the retrograde state, before cycling them back to lower inclination. Examining only the clones that undergo ϖ shepherding, we find that this i flipping is a characteristic feature from the secular interactions (see Figure 5.6). The P9 hypothesis implies the existence of an undetected, but potentially detectable, population of high-i and retrograde large-a TNOs. Clones spend over half of the time with $i > 30°$ suggesting that for each detected TNO there should be at least one undetected TNO at a higher inclination. This implies that in a P9 Solar System, the mass estimates above should be factors of several larger.

We test the sensitivity of our results to the choice of P9 inclination. In all simulations, we find that ϖ shepherding is only induced for $a > 250$ au clones. Figure 5.7 panel B shows that the q oscillations occur across all choices of P9 i for ϖ shepherded clones. Inclination raising and flipping occurs for both P9 simulations with a non-zero i perturber and takes the same form of raising inclinations through extreme and retrograde values that then cycle back to small values (Figure 5.7 panel A). The results in this work are independent of the choice of P9 inclination, with the exception that a zero degree inclination for P9 does not induce the same raising and flipping of inclinations in the clones of ϖ shepherded TNOs.

5.5 Summary and Discussion

1. The P9 scenarios explored do not generically induce ω shepherding for the region of the observed TNOs ($a < 500$ au), a fact already noted in Batygin & Brown (2016a). This holds true even for TNOs that exhibit ϖ shepherding. The apparent clustering of ω is the initial signal that motivated the current incarnation of the hypothesis of a distant planet in the Solar System. The P9 scenarios explored in this work do not reproduce the observed signal of simultaneous clustering in ω, Ω, and ϖ in the region of the detections (Figure 5.1).

2. Clones that undergo ϖ shepherding have their inclinations lifted to retrograde values. If there is a massive distant 9th planet, then there should be a significant number of lower-q, large-a, large-i (or even retrograde) TNOs; only two retrograde TNOs (2008 KV_{42} or Drac, Gladman et al. (2009b), and 2011 KT_{19} or Niku, Chen et al.

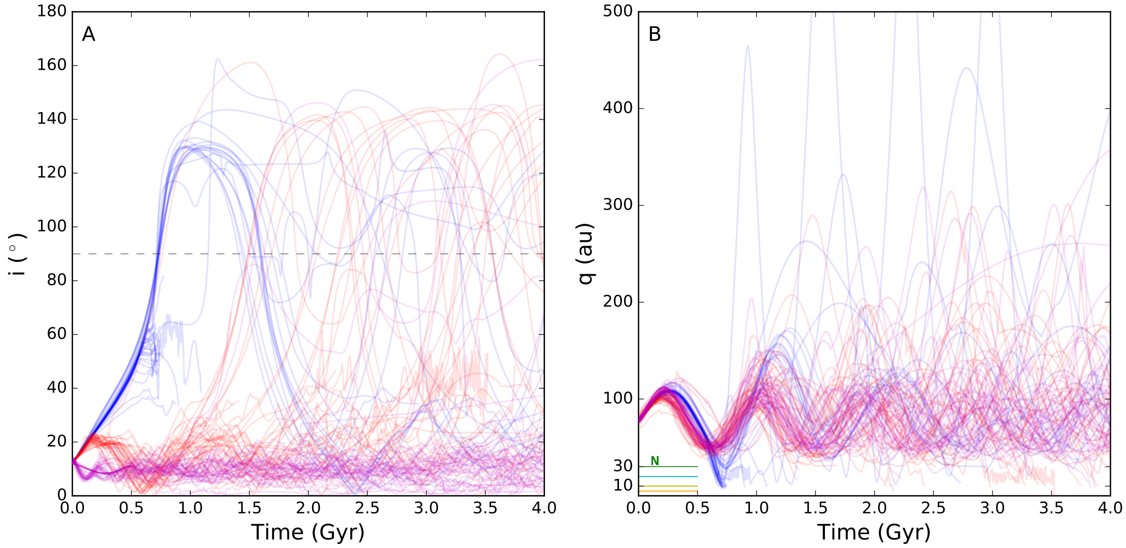

Figure 5.7: The i, q evolution of the Sedna clones for the various P9 configurations. Clones from the simulation with $i = 30°$ are shown in blue, P9 $i = 15°$ in red and P9 $i = 0°$ in magenta. A dashed grey line marks $i = 90°$ in Panel **A**. Panel **A** shows that the same i raising and flipping is induced for ϖ shepherded clones in both the P9 $i = 30°$ and P9 $i = 15°$ cases. Panel **B** shows that large q oscillations occur for ϖ-shepherded clones in all simulations. The cycling of q is a generic feature of a massive external perturber, regardless of the perturber's inclination. Inclination raising occurs generically for ϖ shepherded clones in the simulations with high (30°) and more moderate (15°) perturber inclinations.

(2016)) are known today, both of which have small semi-major axes. Additionally, clones of TNOs that undergo ϖ shepherding (i.e. those with $a > 250$ au) spend a significant portion of the age of the Solar System with large inclinations, but all of the large-a TNOs were detected with $i < 30°$. While there is a bias towards detection at low-i, Sedna was detected in an all-sky survey with sensitivity to high-i and other surveys have looked at high latitudes (e.g. Schwamb et al. (2009), NGVS Chen et al. (2013), CFEPS Petit et al. (2016)) but none have found any large-a (> 100 au), high-i TNOs. The lack of detections of highly inclined TNOs poses a challenge for the inclined P9 scenario.

3. During their orbital evolutions, ϖ-shepherded clones evolve through $q > 80$ au orbits where they would not be detected. The existence of a few $q \sim 40 - 80$ au detections implies a very massive (tens of $M_\oplus$) distant-q reservoir and thus an efficient mechanism for delivery of material into this distant zone of the Solar System. Implanting $\gtrsim 10 M_\oplus$ of solids on large-a, large-q orbits with a high efficiency in the range of 10% to 1% would requires an implausibly large initial planetesimal disk with, respectively, hundreds to thousands of $M_\oplus$ of solids.

4. The existence of a distant massive planet destabilizes the orbits of the large-a TNOs, like 2000 CR_{105}, 2004 VN_{112}, and 2012 VP_{113}, that would otherwise remain stable for the age of the Solar System. Such a scenario thus requires an active supply reservoir and mechanism to deliver objects onto these orbits. The perturber itself may act as the supply for this region, but this avenue was not explorable with these simulations. The pericenter raising of a distant massive perturber will necessarily populate orbits with q between 50 - 70 au, and therefore the scenario is inconsistent with the suggestion of a gap in the q distribution proposed in Trujillo & Sheppard (2014).

5. As has been recently noted by Sheppard & Trujillo (2016), some of the observed clustering in Ω may, in fact, be the result of observing bias. Given that the observed TNOs cluster in ω near 0, and given a strong bias to detecting the TNO at pericenter, the Ω detected is determined by the direction of the survey pointing. The location of survey pointings is determined by galactic plane avoidance and local weather conditions that are season dependent. These biases may be able to explain the apparent clustering in Ω of the detected sample; future work is required to examine the effects of this bias in detail. While this manuscript was in preparation, Sheppard & Trujillo (2016) report the discovery of several new large-a TNOs that would fall within the sample explored here. Two of these TNOs have Ω values that broaden the range in the observed sample, which suggests that this apparent clustering will be eroded with future detections.

A bias in Ω, given the clustering in ω, would cause apparent ϖ clustering. In order to explain the observed sample, the successful theory must be able to explain either the observational bias or the dynamical pathway to shepherding ω that results in the apparent clustering of ω in the observed sample.

6. A massive external peturber generically causes cyclic pericenter oscillations that drive TNOs into Neptune or even Jupiter crossing orbits. This process decouples TNOs from any shepherding influence of the external perturber and results in the randomization of ω and Ω in the large-a TNOs due to precession. TNOs interacting with Neptune and the external perturber can become distributed in the large-a region with random ω and Ω angles and should be part of the detected sample. The observed clustering of ω and Ω (Figure 5.1) are not produced in the P9 scenario.

7. In exoplanet and debris disk systems with a massive external perturber, ϖ

shepherding may have implications for dust production. The induced shepherding of ϖ aligns orbits in physical space and will bring particles to pericenter in the same angular region, which may enhance the collisional probability and thus dust production for this location. This may prove an interesting avenue to explore for systems with massive eccentric exoplanets beyond the debris disk and could possibly contribute to a pericenter glow (Wyatt et al., 1999).

5.6 Conclusion

In this work we have integrated clones of the $a > 150$ au, $q > 30$ au TNOs for 4 Gyr in the presence of a candidate P9 perturber, examining the consequences of a distant massive perturber on the TNOs used to infer the planet's existence. We find that P9 shepherds ϖ for clones with $a > 250$ au, driving this confinement for hundreds of Myr to 4 Gyr. Clones that experience ϖ shepherding also undergo q oscillations and i flipping, which suggests the presence of a very massive (tens of $M_\oplus$) reservoir of large-a TNOs. The P9 scenario produces a larger reservoir of potentially detectable yet unseen high-i TNOs with shepherded ϖ values, suggesting there is a currently missing or unseen signature of P9. The P9 scenario does not produce the observed simultaneous clustering in the angles ω, Ω, and ϖ that is seen in the detected sample. Taken alone, each of the consequences poses a challenge for the P9 scenario. Taken together, these consequences suggest that the existence of the proposed distant massive perturber is unlikely.

A distant massive perturber produces a set of very interesting signatures on a set of large-a planetesimals, but the signature that has driven the newest incarnation of the distant planet hypothesis, namely the clustering of ω, Ω, and ϖ, is not produced by this scenario. Ongoing surveys (like the Outer Solar Systems Origins Survey (Bannister et al., 2016) and that of Trujillo & Sheppard (2014); Sheppard & Trujillo (2016)) will hopefully provide the detections and proper survey characterizations needed to examine the underlying impetus for the P9 scenario: the apparent clustering in ω, Ω, and ϖ of the large-a TNOs.

Acknowledgements

This project was funded by the National Science and Engineering Research Council and the National Research Council of Canada. This research used the facilities of the Canadian Astronomy Data Centre operated by the National Research Council of Canada with the support of the Canadian Space Agency. CS gratefully acknowledges support from the NSERC CGS Fellowship. SML gratefully acknowledges support from the NRC Canada Plaskett Fellowship.

Chapter 6

OSSOS VI. Striking Biases in the detection of large semimajor axis Trans-Neptunian Objects

Published as C. Shankman, JJ. Kavelaars, M. Bannister, B. Gladman, S. Lawler, Y.T. Chen, M. Jakubik, N. Kaib, M. Alexandersen, S. Gwyn, J.M. Petit and K. Volk 2017 *AJ* 154 50

Available online here: http://iopscience.iop.org/article/10.3847/1538-3881/aa7aed/meta

6.1 Abstract

The accumulating, but small, set of large semi-major axis trans-Neptunian objects (TNOs) shows an apparent clustering in the orientations of their orbits. This clustering must either be representative of the intrinsic distribution of these TNOs, or else arise as a result of observation biases and/or statistically expected variations for such a small set of detected objects. The clustered TNOs were detected across different and independent surveys, which has led to claims that the detections are therefore free of observational bias. This apparent clustering has led to the so-called "Planet 9" hypothesis that a super-Earth currently resides in the distant solar system and causes this clustering. The Outer Solar System Origins Survey (OSSOS) is a large program that ran on the Canada-France-Hawaii Telescope from 2013–2017, discovering more than 800 new TNOs. One of the primary design goals of OSSOS was the careful determination of observational biases that would manifest within the detected sample.

We demonstrate the striking and non-intuitive biases that exist for the detection of TNOs with large semi-major axes. The eight large semi-major axis OSSOS detections are an independent dataset, of comparable size to the conglomerate samples used in previous studies. We conclude that the orbital distribution of the OSSOS sample is consistent with being detected from a uniform underlying angular distribution.

6.2 Introduction

Examining the TNOs in the Minor Planet Center (MPC) database, Trujillo & Sheppard (2014) noted that the then-known TNOs on orbits with semi-major axis, a, beyond 150 au and pericenter, q, beyond 30 au have arguments of pericenter, ω, clustered around 0° (Trujillo & Sheppard, 2014). Many surveys are conducted near the ecliptic plane, and this results in a known bias favoring the detection of TNOs that come to pericenter near the ecliptic plane and thus have ω near 0° or 180°. There has been no demonstrated bias that would favor detections of TNOs with ω near 0° versus those at 180°. Batygin & Brown (2016a) noted that the MPC TNOs with $a > 250$ au also have clustered longitude of ascending node, Ω, and longitude of pericenter, $\varpi \equiv \omega + \Omega$. Absent additional stabilizing mechanisms, gravitational perturbations from Neptune would randomize these orbital angles on relatively short timescales. If the observed clustering of orbital angles is reflective of the intrinsic TNO distribution, there must be some dynamical mechanism forcing these orbital angles to be confined to the present day. This line of reasoning has led some to hypothesize the existence of an as yet unseen giant planet in the distant solar system to explain the apparent orbital angle clustering (Trujillo & Sheppard, 2014; Batygin & Brown, 2016a). The idea that an unseen planet shapes the distant TNO region is not new and has been invoked to explain the formation of high-perihelion TNOs like (148209) 2000 CR_{105} and (90377) Sedna (Gladman et al., 2002; Brown et al., 2004; Gomes et al., 2006; Soares & Gomes, 2013) and the possible resonant period ratios of large-a TNOs (Malhotra et al., 2016).

A key premise of the most recent distant planet hypothesis, which has not yet been independently tested, is that the apparent clustering of orbital angles does not result from observing bias. It has been argued that the MPC sample is from independent surveys, thus their biases should be uncorrelated and the observed sample distribution should therefore not have strong biases for the detection of ω and Ω (Batygin & Brown, 2016a). Unfortunately, most of the TNOs in the MPC are from surveys where the discovery circumstances and survey characteristics remain unpublished, making it impossible to fully account for the observing biases in the full MPC sample.

OSSOS provides a completely independent, single-survey, sample of newly discovered large-a TNOs that is comparable in size to those samples used previously. OSSOS is a large program on the Canada-France Hawaii Telescope that surveyed 170 deg^2 over a range of heliocentric longitudes near the ecliptic in 2013–2017. The details of the observing strategy and processing can be found in Bannister et al. (2016). The OSSOS discoveries exceed 830 TNOs with exceptionally well-determined orbits; the high-precision OSSOS astrometry allows rapid orbit determination for classification. All OSSOS discoveries brighter than the survey flux threshold were carefully and thoroughly tracked to avoid ephemeris biases (Jones et al., 2010). The sensitivity (as a function of flux and motion rate) for each OSSOS observation block is accurately determined, allowing detailed modelling of the sensitivity of OSSOS to TNO orbit distributions.

The OSSOS large-a TNOs (Table 6.1) were all detected comparatively close to their perihelia, an expected discovery bias for large-a TNOs. OSSOS detected 8 TNOs with $a > 150$ au, $q > 30$ au versus the 12 TNOs from unpublished surveys contained in the MPC used in Trujillo & Sheppard (2014), and OSSOS detected 4 TNOs with $a > 250$ au, $q > 30$ au versus the sample of 6 MPC TNOs used in Batygin & Brown (2016a). The OSSOS sample provides an analogue to the MPC sample while, crucially, also providing the detailed characterization necessary to model the observing biases affecting the detection of our discoveries.

This analysis addresses the following questions:

1. what are the observing biases, particularly those related to the orbital angles ω, Ω, and ϖ, in OSSOS for the $a > 150$ au, $q > 30$ au TNO region?

2. is there evidence in the OSSOS sample, as has been argued for in the MPC sample of TNOs, of clustering in ω (for $a > 150$ au), Ω ($a > 250$ au) or ϖ ($a > 250$ au)?

3. can we reject the null hypothesis that the intrinsic distributions of ω, Ω, and ϖ are all uniform?

MPC Desig.	**OSSOS Desig.**	a **(au)**	e	q **(au)**	i **(°)**	Ω **(°)**	ω **(°)**	ϖ **(°)**	r **(au)**	m_r	H_r	$\mathbf{T_{peri}}$ **(JD)**	**No. obs.**	**Arc (days)**
2013 GP_{136}	o3e39	150.2 ± 0.1	0.727	41.0	33.5	-149.3	45.4	-106.8	45.5	23.1	6.4	2465012	31	1566
	o5m85	153.0 ± 0.3	0.739	39.9	27.1	67.6	-129.2	-61.6	51.7	24.7	7.6	2471713	36	1087
	o3l83	200 ± 1	0.780	43.9	10.7	-168.0	-107.9	84.1	61.2	24.1	6.2	2476001	36	1278
	o5s13	226 ± 3	0.861	31.4	6.0	-18.5	-5.5	-24.0	34.3	24.6	9.1	2452363	27	538
	o5p060	312 ± 2	0.877	38.4	8.8	46.1	129.0	175.1	41.0	24.5	8.3	2451593	34	824
	o5t52	430 ± 20	0.894	45.5	12.1	8.6	65.2	73.8	62.4	24.1	6.1	2475606	33	587
	o5m52	680 ± 2	0.940	40.5	14.0	-140.9	32.1	-108.8	41.1	24.3	8.1	2459752	29	739
2013 SY_{99}	uo3l91	735 ± 15	0.932	50.0	4.2	29.5	32.2	61.7	60.9	24.8	6.8	2471634	33	1156

Table 6.1: Ordered by semimajor axis, we provide barycentric J2000 ecliptic orbital elements, from the best fit using the method of Bernstein & Khushalani (2000) to CFHT astrometry listed at the Minor Planet Center as of the time of publication. The observed r-band magnitude m_r, absolute magnitude H_r, time of pericenter passage T_{peri}, number of observations and length of observed arc are given, along with the barycenter distance r at discovery. The 1σ uncertainty from the orbital fit's covariance matrix are listed for a; precisions are 0.001 for e and to 0.1° for the angular elements. All digits presented are significant.

6.3 Observations and Methods

6.3.1 OSSOS Observed Sample of large-a TNOs

To be consistent with Trujillo & Sheppard (2014) and Batygin & Brown (2016a), we use the following criteria to define our sample of TNOs: $a > 150$ au and $q > 30$ au. OSSOS detected 8 TNOs satisfying the above criteria, 4 of which have $a > 250$ au. The discovery circumstances for two of these TNOs are described elsewhere: o3e39 (Bannister et al., 2016, 2013 GP_{136}) and uo3l91 (Bannister et al., 2017, 2013 SY_{99}). The six new TNOs we present here were found during the rest of the survey: all are characterized discoveries with well-quantified detection efficiencies. The discoveries have a ranging from 150 au to 735 au, and all but one have $q > 37$ au (Table 6.1).

6.3.2 A Note On q Selection Criteria

One might be tempted to impose a q cut higher than 30 au on the sample to select only TNOs that do not have strong gravitational interactions with Neptune (found to be those with $q \lesssim 37$ au by Lykawka & Mukai (2007b)). The argument being that TNOs with q sufficiently close to Neptune will undergo evolution in a and orbital orientation angles on short timescales and so should be removed from the sample. Embedded in this argument is the assumption that the observed clustering for the sample described above does not result from observation bias. This work seeks to test that assumption, and so we employ a q lower limit of 30 au to be consistent with prior studies and the region where the MPC TNOs show clustering in orbital angles.

It has also been suggested that only TNOs presently dynamically stable with respect to Neptune should be used to define the sample that is examined for clustering (Batygin & Brown, 2016a). The idea being that the TNOs under consideration should be stable to perturbations from Neptune if one is to invoke an additional planet to explain their apparent clustering. If there is a massive planet in the distant solar system, the region between this planet and Neptune would be, in general, unstable. Such a planet would cause pericenter cycling and give dynamical kicks to these large-a TNOs, creating a population analogous to the centaurs, which is seen in multiple simulations with a variety of additional planet candidates (Batygin & Brown, 2016b; Lawler et al., 2016; Shankman et al., 2017). TNOs beyond Neptune that are "presently" stable would not necessarily be stable in the case of an additional massive planet beyond Neptune.

In any case, if the q threshold is set to a higher limit, one *must* still be able to explain why TNOs with q further in, that should be less stable, appear clustered in the MPC sample. To reiterate, this analysis examines observational biases and looks for evidence of clustering in the OSSOS sample. Thus we select our sample using the same orbital element ranges for which arguments of clustering have been made.

6.3.3 Survey Simulation of the Observability of Large-a TNOs

OSSOS is a characterized survey with measured and reported biases. The pointing directions of the survey itself (Table 1, Bannister et al. (2016)) are of key importance for the observing biases in orbital angles, as we will demonstrate. For the purposes of this analysis, we provide the relevant OSSOS TNOs (Table 6.1) and a full implementation of the survey simulator including an example model distribution is available by request.

We perform simulated surveys on a set of distributions of orbits with $a > 150$ au, $q > 30$ au to probe the effects of the OSSOS observing biases on the detectability of TNOs in the phase space of interest. A detailed description of this established survey simulation suite can be found in Jones et al. (2006) and Petit et al. (2011), and recent examples of the use of the survey simulator in TNO studies can be found here: Nesvorný (2015); Alexandersen et al. (2016); Shankman et al. (2016); Pike et al.

(2017).

We construct test distributions that fully cover ranges of orbital phase space that include the detected large-a TNOs. The models tested are not intended to reproduce the observed distributions. They were designed to probe a variety of forms of distributions to test the sensitivity of the analysis to the specific choice of distribution. The models tested are combinations of distributions covering the following parameter spaces and forms:

- a: distributions spanned 150 au to 1000 au. Distributions were either uniform in a or $\propto a^x$, with exponents x spanning 0.5 to 1. Distributions with an upper limit of 800 au were also tried to test for sensitivity to the a cut off.
- eccentricity, e: uniform from 0.7 to 0.95. A q lower limit was imposed at 30 au.
- inclination, i: Two forms were tested. **1** a uniform distribution from 0° that extends up to 55° (the range of the observed OSSOS sample) and **2** a distribution that scales as $\sin(i) \times$gaussian (as in Brown, 2001). A variety of gaussian centers (between 0°, and 20°) and gaussian widths (between 5° and 15°) including different combinations of centres and widths were used.
- absolute magnitude, H: single slope from H_r of 6 to 9.5 with a slope of 0.9. Divot and knee distributions as in Fraser et al. (2014) and Shankman et al. (2016) were also tested.
- ω, and Ω uniform from 0° to 360°, making ϖ uniform as well.

With each distribution, we conducted an OSSOS survey simulation that "detected" 10 000 simulated TNOs. These survey simulations reveal the observing biases present in the survey and show any gaps or preferences in the sensitivity to certain orbits. We find that the choice of model does not affect the conclusions about the intrinsic orbit angle distribution (see Appendix Figure 6.6).

6.4 Results

6.4.1 Observing Bias

Figure 6.1 plots the results of the survey simulation. Our simulations find OSSOS has a range of sensitivities to and biases in different orbital parameters of TNOs. We discuss in turn our sensitivity to each angle of TNO orbit orientation. All discussions of panels in this section refer to panels in Figure 6.1. Panels **A**, **B**, and **C** plot the orbital angles versus a with histograms of the simulated detections for these angles. All statements of the sensitivity in OSSOS are made exclusively with respect to the TNO model constraints as outlined above.

ω **sensitivity:** OSSOS has some sensitivity to all argument of pericenter ω values, which can be seen in panels **A**. Panel **A** shows that the TNOs on orbits with ω values near 0° or 180° are more likely to be detected. This effect arises in near-ecliptic surveys when TNOs are detected near their pericenter. The OSSOS pointings were not centered exactly around the ecliptic, with almost all the off-ecliptic coverage being North of the ecliptic. Blocks that are off ecliptic no longer have symmetric sensitivity with 0° and 180° favored, but instead have only one area of reduced sensitivity, as also discussed in Sheppard & Trujillo (2016). This lack of sensitivity is caused by the fact that some pericenter locations are not possible to detect for a survey off ecliptic. For example, a survey that points above the ecliptic is unable to see any sky points below the ecliptic and thus has a lower sensitivity to detecting orbits that come to pericenter below the ecliptic. This effect results in less OSSOS sensitivity to TNOs with ω near $-90°$ than near 90°. OSSOS still has some sensitivity to TNOs away from their pericenter due to its deep limiting magnitudes, resulting in some sensitivity to TNOs with ω near $-90°$, as seen in panel **A**.

Ω **sensitivity:** There exists clear and initially non-intuitive structure in the OSSOS observing bias in longitude of the ascending node Ω. Panel **B** shows that there is a large and substantial gap in Ω sensitivity in the -120° to -20° range. OSSOS, due to its avoidance of the galactic plane and northern hemisphere winter, has virtually no capability for detecting large-a TNOs with Ω between -120° to -20°. Figure 6.2 shows that this structure arises from a coupling of sensitivity in Ω and i. This striking effect is a simple result of geometry. The Ω and i angles define the plane of the TNO's orbit. In order for the TNO to be detectable by a survey, its plane must intersect the area of sky being observed. For inclined orbits to have a high chance of being detectable in an ecliptic survey, the ascending or descending node must be in the same direction as the survey's pointing. Each of the horizontal spikes in Figure 6.2 indicates the location of an ascending or descending node that is aligned with one of the OSSOS pointings. The bias structure curves horizontally as inclinations go towards 0°, when orbits become ecliptic grazing, and can thus be seen at more points across their orbit in ecliptic surveys. We plot the OSSOS detections in Table 6.1 in panel Figure 6.2 to show that they follow this bias-induced distribution of Ω and i.

ϖ sensitivity: The sensitivity to detecting longitude of pericentre ϖ is a combination of the sensitivities to detecting Ω and ω. The sensitivity is a double peaked distribution, with less sensitivity to ϖ in the range of 110° to 160° (see Panel **C**). OSSOS has some sensitivity to all ϖ values and there is no striking structure in the ϖ sensitivity other than the two broad peaks roughly separated by 180° of longitude.

We examined the three above biases for both the $a > 150$ au and $a > 250$ au regions to explore if the sensitivity changes with a. We find that the observing biases are the same for the two regions, which can be seen by comparison of the blue and grey histograms in Figure 6.1. Once a TNO has a sufficiently large orbit, it is only detectable near pericenter. This bias strongly affects the expected detection of orbital angles as we have shown. The bias structure does not change as a function of increasing a because the bias is a result of the fact that the TNOs are only detectable near pericenter.

Although the biases we demonstrate are specific to OSSOS, all TNO surveys will have complicated detection biases like those shown in this work. Without publishing characterizations of the survey pointings, these complex and often non-intuitive biases cannot be accounted for, and may lead to incorrect assumptions about the intrinsic population.

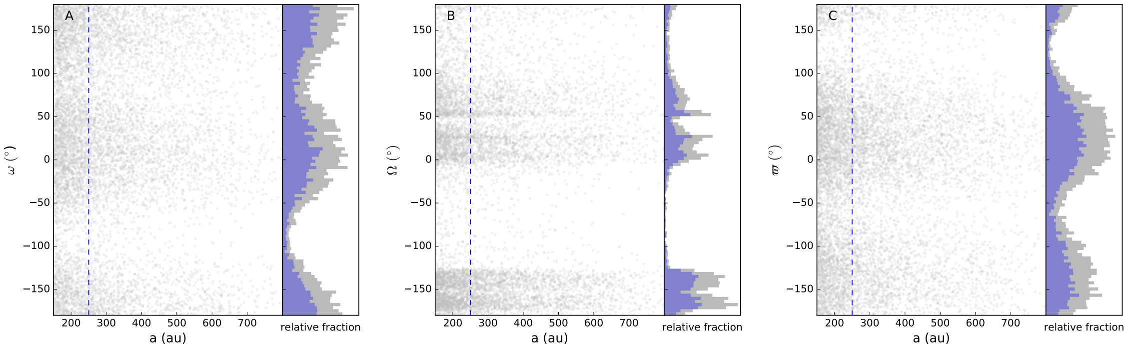

Figure 6.1: Visualization of the detection bias for large-a TNOs in OSSOS. Simulated detections drawn from a uniform intrinsic distribution are plotted in transparent grey points. Blue dashed lines in Panels **A**–**C** demarcate $a = 250$ au. The side panels show histograms of the ω, Ω, and ϖ of the orbits of simulated detections. The grey histograms show the simulated detections of a model with uniform orbit angles. Blue histograms show the subset of those simulated detections with $a > 250$ au orbits. Appendix Figure 6.7 shows that the biases do not vary as a function of q.

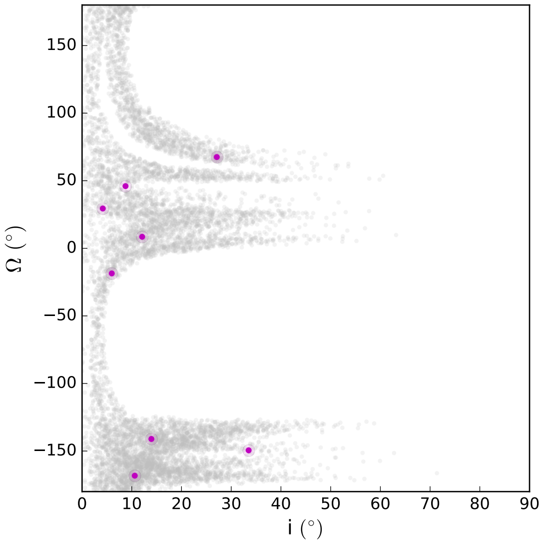

Figure 6.2: The Ω / i sensitivity of the OSSOS project. The grey dots are the same simulated detections in Figure 6.1, having $a > 150$ au, $q > 30$ au. The OSSOS TNOs have been overplotted in magenta to show how the observed sample is affected by these strong biases.

6.4.2 Angle Clustering in the OSSOS Sample

Having examined the biases of OSSOS, we now examine the detected OSSOS sample (Table 6.1) for evidence of a clustering in the orbital angles for the large-a TNOs, as first noted in the MPC dataset by Trujillo & Sheppard (2014) and Brown & Batygin (2016). We consider the OSSOS sample independently, examining the distributions of the OSSOS TNOs with no *a priori* expectations about clustering.

A visual examination of the orbital distribution (see Figure 6.3) shows relatively little evidence of clustering of ω, even in the observationally biased $a > 150$ au OSSOS sample. The eight OSSOS TNOs are found distributed across the full range of ω values (Figure 6.3 panel **A**). We demonstrated in Section 6.4.1 that OSSOS has some sensitivity to all ω values; this sensitivity is reflected in the broad distribution of detected ω values. For each orbital angle, we test the hypothesis that the OSSOS sample can be detected from a uniform intrinsic distribution. To do this, we compare the observed distributions to the survey simulator biased models described above (Figure 6.1). We test the null hypothesis using Kuiper's test (e.g. see Fisher, 1995; Pewsey et al., 2013), which is closely related to the Kolmogorov-Smirnov test, but is invariant to cyclic transformations of the test variable. The test is thus well suited to problems with cyclic variables, as is the case for angles like ω, Ω, and ϖ. The eight TNOs are statistically consistent (i.e. 53% of bootstrapped model subsamples have a larger Kuiper's test distance than the observed sample to the parent model: the hypothesis is rejectable at 47%, i.e. not rejectable) with being detected from an intrinsic uniform distribution of ω values. Our results hold for all tested intrinsic models described in Section 6.3.3.

We now examine the Ω and ϖ distributions for the OSSOS TNOs with $a > 250$ au. We find that the Ω values for three of the TNOs are distributed near 25° with the fourth isolated (Figure 6.3 panel **B**). OSSOS had effectively no sensitivity to TNOs with Ω between -120° and -20°, and had poor sensitivity to TNOs with Ω between 115° and 165° (see Figure 6.3 panel B histogram). Unsurprisingly, OSSOS did not detect TNOs in regions of limited or no sensitivity. Using Kuiper's test, we find that the OSSOS detections are statistically consistent (rejectable at 61%, i.e. not rejectable) with being detected from an intrinsic uniform distribution of Ω values. We find that the ϖ values cover a large range, with only two values near each other. As with ω and Ω, the OSSOS TNO ϖ values are consistent (rejectable at 62%, i.e. not rejectable) with being detected from an intrinsic uniform distribution of ϖ values.

We conclude that the independent OSSOS sample shows no evidence for intrinsic clustering in the ω, Ω or ϖ distributions of TNOs.

6.4.3 OSSOS and MPC Sample Comparison

We now compare the OSSOS sample (known biases) to the MPC sample (unknown biases) to examine the broader question of clustering in the known TNOs. Figure 6.4 plots the eight OSSOS TNOs and the MPC TNOs satisfying $a > 150$ au and $q > 30$ au as reported by the MPC in April 2017.

Figure 6.4 panel **A** shows clearly that the apparent clustering in ω that has been noted in the MPC sample is not present in the OSSOS sample, despite the OSSOS survey biases against $\omega = \pm 90°$. Where the MPC sample is contained within roughly 50° of 0°, the OSSOS sample spans all values and has as many TNOs inside the apparent clustering region (grey shading of Figure 6.4 panel **A**) as outside. The OSSOS TNOs that are outside the apparent clustering region have a variety of semi-major axes and all have $q > 37$ au. With the addition of the OSSOS sample and a few recently discovered TNOs in the MPC sample, the argument for a clustering of ω in the detected TNOs has been substantially weakened.

There is no overlap between the OSSOS sample and the Ω clustering region of TNOs with $a > 250$ au noted in Batygin & Brown (2016a), with all four OSSOS detections outside the clustered band. The four $a > 250$ au OSSOS detections span a range of a values and all have $q > 37$ au. If one were to consider the three OSSOS detections with Ω between 0° and 50° to be part of the clustered grouping, the clustering would then span approximately 150°. Sheppard & Trujillo (2016) noted that their recent discoveries began to erode the signal of clustered Ω in the large-a TNOs; the four OSSOS detections outside the previously reported band continue this trend of eroding the signal. This would be expected if the original signal results from a combination of small number statistics and observing bias.

Two of the OSSOS $a > 250$ au TNOs with ϖ near 70° are within the Batygin & Brown (2016a) proposed "anti-aligned" cluster. The third, o5m52 with a ϖ of $-110°$ is approximately 180° away, and would fall in the subsequently postulated "aligned" cluster (Brown & Batygin, 2016; Sheppard & Trujillo, 2016). Discoveries at these values of ϖ is unsurprising in OSSOS as the observing bias favors detections with ϖ at these longitudes (Figure 6.1 panel **C**). The final OSSOS detection, o5p060, however, is approximately 90° away from each of these proposed clustering regions.

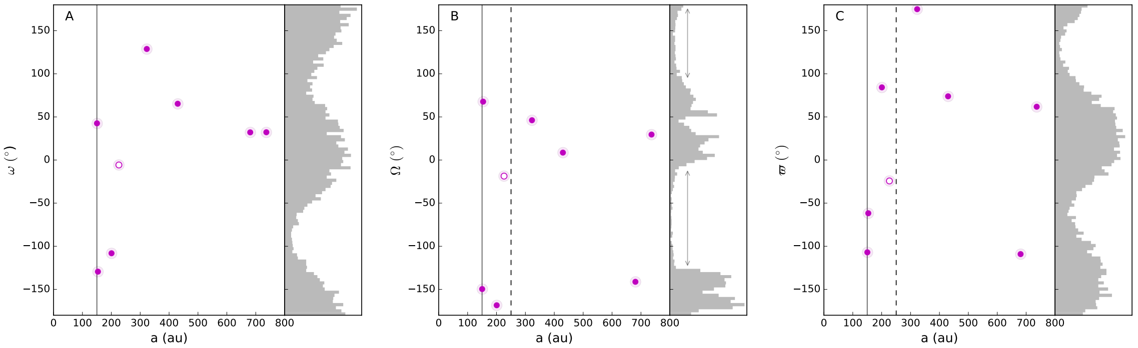

Figure 6.3: The OSSOS detections satisfying $a > 150$ au and $q > 30$ au are shown with magenta points. Open circles indicate TNOs with $q < 37$ au - a threshold cited to demarcate the region of stability from Neptune perturbations (Lykawka & Mukai, 2007b). Solid vertical lines mark 150 au and dashed lines mark 250 au. Histograms repeat the OSSOS sensitivity in each parameter as in Figure 6.1. Double sided arrows in the Panel B histogram mark the Ω ranges where OSSOS has low sensitivity due to the survey's bias, and thus detections are unlikely.

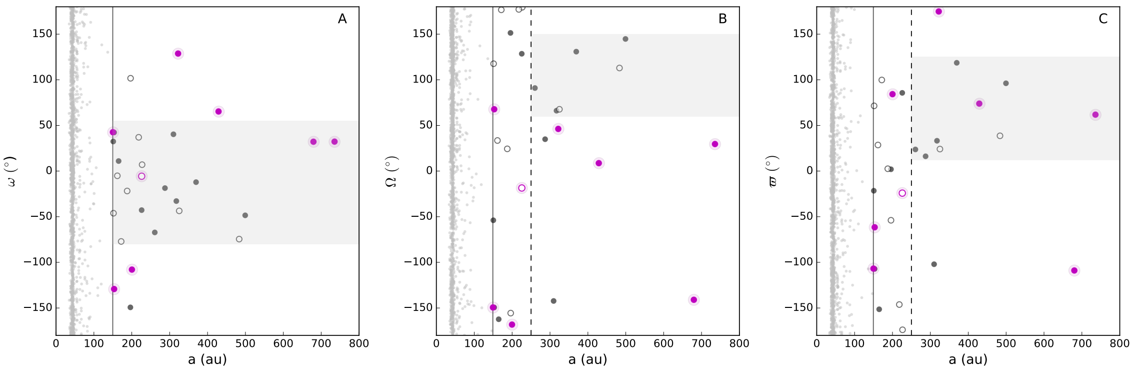

Figure 6.4: Plots of the orbits of the OSSOS and MPC samples for ω, Ω and ϖ versus a. The MPC sample has been selected with $q > 30$ au. OSSOS detections are shown in magenta points. MPC TNOs are plotted in transparent grey points, which are larger for $a > 150$ TNOs. There are no OSSOS discoveries in the $a > 150$ au MPC grey points. Solid vertical lines mark 150 au and dashed lines mark 250 au. The grey shaded regions indicate the regions of apparent clustering in the MPC sample proposed by previous authors. As in Figure 6.3, open circles indicate TNOs with $q < 37$ au, showing how a stability argument might affect the argument for clustering. It is clear from this view that the MPC TNOs with q between 30 au and 37 au still appear to cluster in ω (for $a > 150$ au) and Ω and ϖ (for $a > 250$ au), despite the fact that interactions with Neptune would prevent shepherding by an external planet. Note: 2014 FE$_{72}$ with $a = 2155$ au, $q = 36$ au, $i = 20°$, $\omega = 134°$, and $\Omega = -23°$ has been excluded from these plots because it interacts with galactic tides (Sheppard & Trujillo, 2016)

6.5 Discussion and Summary

We find no evidence in the OSSOS sample for the ω clustering that was the impetus for the current additional planet hypothesis (Trujillo & Sheppard, 2014). The OSSOS ω distribution cannot reject the null hypothesis that the underlying distribution is random, once the biases are taken into account. Our analysis of the OSSOS survey bias and our detections do not directly address the question of why the majority of presently known MPC TNOs are clustered around ω of 0°. We suggest that this clustering is the result of a combination of observing bias and small number statistics, though we cannot test this without published characterizations of the surveys that detected these TNOs. It must be the case that OSSOS and the other surveys that compose the MPC sample have observed the same intrinsic distribution. OSSOS found TNOs across all values despite being most sensitive to TNOs in the clustering band (near 0°). The OSSOS detections go beyond the relatively tight clustering seen

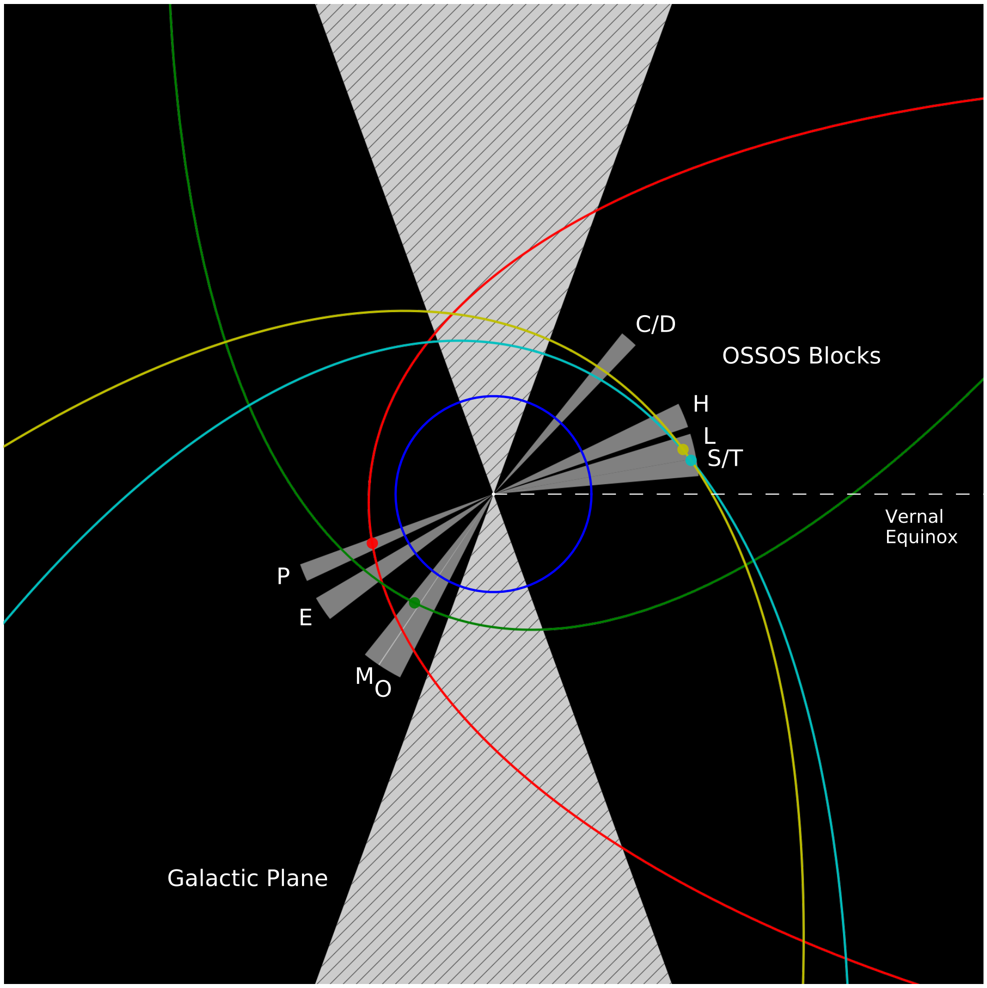

Figure 6.5: A top-down view of the Solar System including Neptune, a schematic for the OSSOS pointings and the four $a > 250$ au OSSOS TNOs. Neptune's orbit is plotted with a blue circle. The OSSOS TNOS are plotted in the following colours: o5p060 red, o5m52 green, o5t52 cyan, uo3l91 yellow. The discovery location of each TNO is indicated by a point of the appropriate colour. The eight OSSOS blocks (Bannister et al., 2016, Table 1) are plotted in grey and labelled (note that detection sensitivity continues radially beyond the wedge boundaries). The rough location of the galactic plane is plotted in hatched wedges. A dashed line indicates the direction of the vernal equinox, and therefore the upper right quadrant is the September to November opposition direction.

in the observed sample, and the OSSOS distribution is consistent with a uniform intrinsic ω distribution. This result calls into question the idea of a clustering of ω around 0° in the intrinsic distribution of $a > 150$ au $q > 30$ au TNOs.

We have demonstrated that Ω biases are strong and very present in surveys such as

OSSOS. These complex biases must also exist in the surveys that compose the MPC sample; it is not sufficient to state that the surveys are independent and therefore the biases must have averaged out. There have been only a handful of surveys that have detected such large-a TNOs, and the biases from these surveys have shaped the MPC sample in unknown ways. There is a large gap in the known TNO Ω distribution for both OSSOS and MPC samples. This gap occurs precisely where OSSOS has no sensitivity due to the survey's construction. In OSSOS, this gap is driven by weather patterns at the Canada-France-Hawaii Telescope and pointing choices that avoid the dense star fields of the galactic plane. Figure 6.5 provides a visual representation that demonstrates the nature of these biases. OSSOS observed in the northern spring (April–May) and fall (September–November), and has virtually no sensitivity to orbits that intersect the ecliptic at other times of the year. TNO surveys have been conducted from a limited number of locations and are subject to similar constraints as OSSOS. In particular, the best conditions (and thus deepest coverage) is in these months. It is therefore possible that the surveys which detected the MPC sample contain these same biases and therefore the gap in the detected Ω distribution may result simply from pointing constraints.

It has been argued that no ω or ϖ biases are seen in the close-in TNOs in the MPC sample and thus there should be no biases in the large-a sample. Unique biases arise from the fact that the large-a TNOs are only detected near their pericenters. The lack of observed clustering in the close-in TNOs cannot simply be extended to conclude that the large-a TNOs lack bias. To verify this via simulation, we examined the OSSOS sensitivity to close-in TNOs, as in § 6.3.3. OSSOS has equal sensitivity for all values of ω and ϖ, in contrast to the striking biases observed for the large-a TNOs (see Appendix Figure 6.8).

Much attention has been given to the appearance of clustering of "aligned" and "anti-aligned" orbits in physical space (apparent clustering of ϖ), which is founded on the assertion that there is no bias in the detection of ϖ. However, we have shown that for TNOs detected near pericenter, the detection of ϖ is also driven strongly by where one looks in the sky. Historical surveys will also show bias favoring detections in the aligned and anti-aligned directions due to the prevalence of large-scale surveys occurring (and having the best weather) in the spring and fall. In order to efficiently detect large-a TNOs outside the aligned and anti-aligned clusters, one would need large survey coverage during June–August and December–February. We posit that two clusters 180° apart are the natural outcome of seasonal weather biases when observing a highly eccentric population for which detection is only possible close to pericenter. The observed TNOs therefore do not require the existence of a non-uniform intrinsic distribution (the impetus of the additional planet hypothesis). Additionally, the MPC sample's ω values are all near 0° and as we have shown, the detected Ω distribution is strongly set by the geometry of the pointing directions. The clustering seen in ϖ in the MPC sample, therefore likely results from adding numbers near 0° to strong observing biases present in the Ω distribution. The apparent ϖ clustering seen in the MPC sample thus cannot be taken to be independent of bias.

While OSSOS was primarily sensitive to orbits with ϖ near the region of the MPC sample clustering (see Figure 6.1), it still found one quarter of its sample away from this region where the sensitivity is low. Despite the reduced sensitivity to such orbits, OSSOS detected o5p060 with a ϖ that produces an orbit orthogonal to the suggested clustering axis. This suggest that there must be a large population of TNOs on similar orbits (of order ten thousand[1]), or that the detection of o5p060 was anomalous. In either case, the existence of o5p060 with a of 314 au, q of 38 au, and ϖ 90° away from the clustering region provides evidence of a population that would refute a simplistic interpretation of the extra-planet hypothesis (Brown & Batygin, 2016) in which *only* anti-aligned orbits can survive.

One might be tempted to choose a different pericenter sample cut, pushing the limit away from 30 au. Setting a limit of 40 au would remove two of the six TNOs noted by Batygin & Brown (2016a) to cluster and one of the four in the OSSOS sample. If one is to argue that a dynamical effect causes the clustering of only the TNOs with q greater than a limit of 40 au (or any other choice), *it must then be explained* why the MPC sample of TNOs with $40 < q < 30$ au also appear to cluster, if the effect is not caused by observing bias.

We have shown that there are strong and striking biases in the detection of the orbital angles present in OSSOS. There is no evidence for clustering in the OSSOS sample when considered alone, and when OSSOS is folded into the MPC sample the arguments for clustering in the detected TNOs erodes. The first large independent sample shows no evidence for the hypothesized intrinsic clustering. While the idea of there being a larger-than-dwarf-scale planet in the outer solar system as a mechanism to create the q-detached TNOs is still plausible, the evidence that there is currently a super-Earth or larger planet confining the large-a TNOs is in doubt.

---

[1] Survey simulations show that approximately 13,000 TNOs with $H_r < 9$ on orbits within the uncertainty of o5p060's orbit are required to explain the detection of o5p60 in OSSOS.

Acknowledgements

This project was funded by the National Science and Engineering Research Council and the National Research Council of Canada. This research used the facilities of the Canadian Astronomy Data Centre operated by the National Research Council of Canada with the support of the Canadian Space Agency. CJS gratefully acknowledges support from the NSERC CGS Fellowship. MTB appreciatively acknowledges support from UK STFC grant ST/L000709/1. SML gratefully acknowledges support from the NRC Canada Plaskett Fellowship. M.J. acknowledges the support from the Slovak Grant Agency for Science (grant No. 2/0031/14). The authors recognize and acknowledge the sacred nature of Maunakea, and appreciate the opportunity to use data observed from the mountain. We thank the dedicated staff of the Canada–France–Hawaii Telescope (CFHT). CFHT is operated by the National Research Council of Canada, the Institute National des Sciences de l'Univers of the Centre National de la Recherche Scientifique of France, and the University of Hawaii, with OSSOS receiving additional access due to contributions from the Institute of Astronomy and Astrophysics, Academia Sinica, Taiwan. Observations were obtained with MegaPrime/MegaCam, a joint project of CFHT and CEA/DAPNIA.

Appendix

Additional Figures

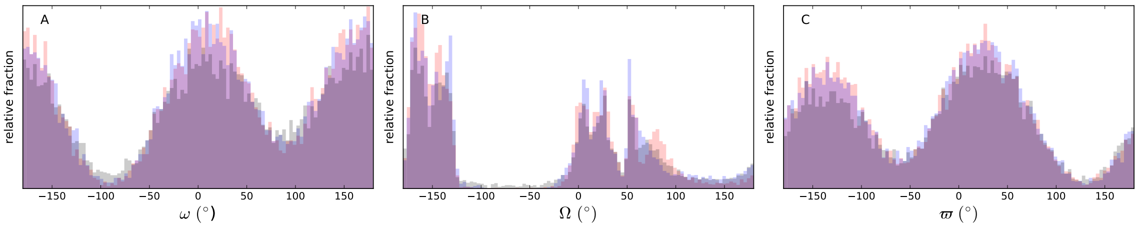

Figure 6.6: Histograms of the sensitivity of OSSOS, as in Figure 6.1, to three different models of orbit distributions (plotted with transparencies). These three models explore different a and i distributions. One model has flat a and i distributions with a spanning 150 au - 800 au and i up to 55°. The other two models have power-law a distributions and i distributions that are drawn from $\sin(i)\times$gaussian distributions with different centres and widths. This shows that the results hold in general across different choices of model distributions.

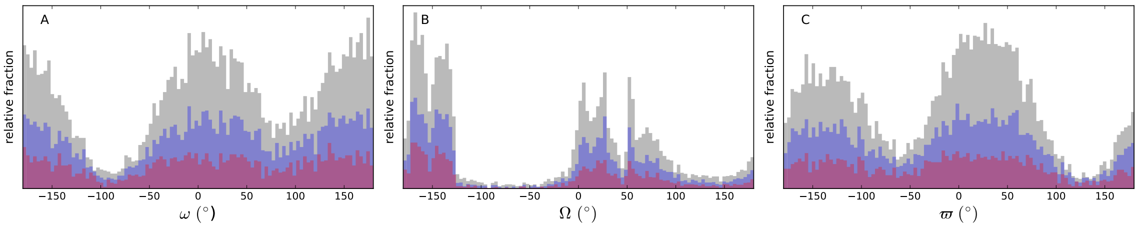

Figure 6.7: Histograms of the sensitivity of OSSOS as in Figure 6.1. The grey histogram shows all simulated detections, the blue histogram shows those with $q < 37$ au, and the magenta histogram shows TNOs with an even lower cutoff of $q < 34$ au. The form of the bias is the same for all q cuts, but the bias is more pronounced for the largest q TNOs.

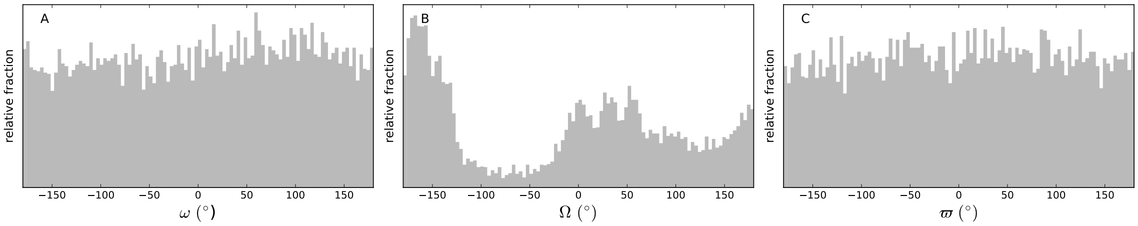

Figure 6.8: Plots of the OSSOS sensitivity to a model orbit distribution with close-in TNOs. The model has both a and q between 30 and 50 au. The strong biases observed in ω and ϖ for the large-a TNOs (Figure 6.2) are not present for this close-in population, which has near equal sensitivity to detecting TNOs with all ω and ϖ values. The biases seen in Figure 6.1 arise from detecting TNOs near pericenter, and thus are not present for close-in TNOs which can be detected at any point in their orbit. The biases in Ω arise from the geometry of orbits intersecting pointing locations, and so are still present in the close-in sample.

Chapter 7

Conclusion

In this thesis I measure the scattering TNO H-distribution and study the additional planet hypothesis from three perspectives. This study fills in a part of the broader TNO puzzle and reinforces the need to properly understand and characterize survey bias for TNO studies.

In Chapter 2 and Chapter 3 I measure the form of scattering TNO H-distribution with the detections in CFEPS, Alexandersen et al. (2016), and OSSOS. I find that the scattering TNO H-distribution cannot be a single slope and must transition and is consistent with both knee and divot H-distributions. I have argued that a divot H-distribution is uniquely able to simultaneously explain the observed H-distributions for several hot populations:

- the divot H-distribution provides the best match to the scattering TNO population
- there is a lack of observed small-sized Neptune Trojans that cannot be explained by a knee or single slope H-distribution, but can be explained by the sudden drop in a divot H-distribution
- applying the scattering TNO divot H-distribution to the Plutino population provides a better match to the observed H-distribution than a knee H-distribution
- the Jupiter Family Comets are not dynamically stable for the lifetime of the Solar System and thus require a source to supply them. A divot H-distribution produces the required number of 1 km scattering TNOs in order for the scattering TNOs to be the source of the JFCs, whereas a shallow knee H-distribution does not.

- a faint slope of $\alpha_f = 0.4$ is seen in the Pluto cratering history. For certain choices of break location, a knee to this slope is excluded and for others a knee is borderline acceptable. Divot distributions to $\alpha_f = 0.4$ provide better matches to the observed sample

I have also shown that the scattering TNOs do not preserve the history of planet migration and formation and that the scattering TNO analyses are not sensitive to the choice of colour distribution. If it can be demonstrated that there must be a divot H-distribution for the scattering TNOs, this discovery would provide the strongest observational evidence to date for a common origin of the hot populations in the outer Solar System and would have implications for the planetessimal formation process.

In Chapter 4 I model the effects that an additional planet has on the observed orbital distribution of the scattering and detached TNOs. I find that the presence from early times of a super-Earth mass planet in the distant Solar System produces a distinctly different scattering and detached TNO orbit distribution. This effect, however, would not be observable by our surveys as the affected TNOs have qs beyond the detection limit of CFEPS and OSSOS. I find that the mass of this high-q population would be three to ten times greater for the case of an additional planet, suggesting that there is a large reservoir of currently undetected TNOs in this scenario. I also conclude that our simulations show no evidence that an additional planet produces a clustering of orbital angles as proposed by Batygin & Brown (2016a).

In Chapter 5 I test the hypothesis that an additional planet can reproduce the observed orbital angle clustering by shepherding the angles over time. I integrate the orbits of the known TNOs in the known Solar System with the addition of the Batygin & Brown (2016a) proposed planet and find that the additional planet does shepherd ϖ for TNOs with $a > 250$ au for a span of time ranging from 100s of Myr to 4 Gyr. The planet does not, however, shepherd the other two orbital angles, ω and Ω. I find that, as a consequence of the process that shepherds ϖ, TNOs with $a > 250$ au undergo cycling of q and raising of i through retrograde values. The q cycling implies a very massive reservoir of distant-q objects with an efficient method of delivering material to this part of the Solar System. The i raising implies an unseen population of high inclination large q TNOs. I find that the proposed planet does not reproduce the observed signal of simultaneous clustering in ω, Ω, and ϖ, potentially hinting that biases play a role in the observations to date.

In Chapter 6 I demonstrate the striking biases extant in the detection of TNOs with large a. I find that the detection of TNOs at certain Ω values is strongly determined by when the observations were taken. I show further that detection of TNOs with certain ϖ values, which measures the orientation of an orbit, is also strongly dependent on the choice of observing direction. I posit that the observed clusterings are the result of seasonal effects at the handful of telescopes used to detect these large-a TNOs. I then analyze the OSSOS large-a TNOs for evidence of orbital angle clustering in this independent sample. I find that there is no evidence for clustering in the OSSOS sample and that when the OSSOS sample is added to the set of all known TNOs, the evidence for clustering of large-a TNOs is eroded.

With the three studies in Chapter 4, Chapter 5 and Chapter 6 taken together, I conclude that the evidence that there is no evidence of a planet in the distant Solar System causing a clustering of orbital elements for the large-a TNOs.

7.1 Looking Forward

Future work will constrain the location of the scattering TNO H-distribution break with the full OSSOS sample. Increasing detections of hot TNO populations, including the Plutinos, Neptune Trojans, and scattering TNOs will reveal if these populations share an H-distribution and thus potentially a formation history. If it can be demonstrated that the scattering TNO H-distribution has a divot, this might suggest that hot TNOs formed big and the small-size TNOs are the result of collisional grinding.

Future surveys could constrain the presence or absence of a planet by looking for high-q, large-i TNOs. Targeted high latitude wide field camera surveys done on existing telescopes can be used to search for large-i TNOs with large-q, a testable prediction of the additional planet hypothesis.

The Large Synoptic Survey Telescope (LSST) will come online in the early 2020s. LSST will will survey the whole sky to a magnitude limit matching or exceeding those of recent large-scale surveys, and has detecting Solar System objects as one its primary science goals (Ivezic et al., 2008). LSST will hopefully dramatically increase the known TNOs and the completeness of the observed sample. This new dataset will be able to answer many mysteries in the TNO populations, and will conclusively determine if there is a clustering in the orbital angles of large-a TNOs.

Whatever surveys are to come, it is clear that characterizing surveys not only provides a powerful analysis tool, but is essential for disentangling the effects of observational bias from signals in the data. It is my hope that future surveys will characterize their biases for the accuracy and health of the TNO field of study.

7.2 Personal Reflections

It has been an exciting time to study the distant Solar System. I was first attracted to Solar System studies because it's where we live. We've visited the Moon, sent robots to colonize Mars, and probes to the giant planets and beyond. It's the one area of Astronomy where we can take detailed resolved photos and imagine ourselves in the near future. During the course of my studies we've seen new and striking images of Enceladus' ice geysers, Jupiter's surface, Saturn's rings, and Pluto's surface. Just two years ago we saw, for the first time, the face of Pluto (Figure 7.1), revealing a strikingly beautiful and unexpected surface that is now part of public consciousness and the rote learning of young children. I've been fortunate to study a field of Astronomy that penetrates the lives of the broader public and where I can even see my own work show up in the Facebook =feed from acquaintances. I'm excited to find out what unexpected discoveries await us as we pull back the next horizons of the distant Solar System.

Figure 7.1: The striking surface of Pluto as imaged by the New Horizons spacecraft. Image courtesy of NASA, distributed without copyright.

Bibliography

Adams, E. R., Gulbis, A. A. S., Elliot, J. L., Benecchi, S. D., Buie, M. W., Trilling, D. E., & Wasserman, L. H. 2014, Astronomical Journal, 148, 55

Alexandersen, M., Gladman, B., Greenstreet, S., Kavelaars, J. J., Petit, J.-M., & Gwyn, S. 2013, Science, 341, 994

Alexandersen, M., Gladman, B., Kavelaars, J. J., Petit, J.-M., Gwyn, S., & Shankman, C. 2014, ArXiv e-prints

Alexandersen, M., Gladman, B., Kavelaars, J. J., Petit, J.-M., Gwyn, S. D. J., Shankman, C. J., & Pike, R. E. 2016, Astronomical Journal, 152, 111

Anderson, T. W. & Darling, D. A. 1954, Journal of the American Statistical Association, 49, 765

Bailey, E., Batygin, K., & Brown, M. E. 2016, Astronomical Journal, 152, 126

Bannister, M. T. et al. 2016, Astronomical Journal, 152, 70

— 2017, ArXiv e-prints

Barucci, M. A., Boehnhardt, H., Cruikshank, D. P., & Morbidelli, A. 2008, The Solar System Beyond Neptune: Overview and Perspectives, ed. M. A. Barucci, H. Boehnhardt, D. P. Cruikshank, A. Morbidelli, & R. Dotson, 3–10

Batygin, K. & Brown, M. E. 2010, Astrophysical Journal, 716, 1323

— 2016a, Astronomical Journal, 151, 22

— 2016b, Astrophysical Journal, Letters to the Editor, 833, L3

Becker, A. C. et al. 2008, Monthly Notices of the RAS, 386, 416

Benecchi, S. D. & Sheppard, S. S. 2013, Astronomical Journal, 145, 124

Bernstein, G. & Khushalani, B. 2000, Astronomical Journal, 120, 3323

Bernstein, G. M., Trilling, D. E., Allen, R. L., Brown, M. E., Holman, M., & Malhotra, R. 2004, Astronomical Journal, 128, 1364

Beust, H. 2016, Astronomy and Astrophysics, 590, L2

Bottke, W. F., Durda, D. D., Nesvorný, D., Jedicke, R., Morbidelli, A., Vokrouhlický, D., & Levison, H. 2005, Icarus, 175, 111

Brasser, R. & Schwamb, M. E. 2015, Monthly Notices of the RAS, 446, 3788

Bromley, B. C. & Kenyon, S. J. 2016, Astrophysical Journal, 826, 64

Brown, M. E. 2001, Astronomical Journal, 121, 2804

Brown, M. E. & Batygin, K. 2016, Astrophysical Journal, Letters to the Editor, 824, L23

Brown, M. E., Trujillo, C., & Rabinowitz, D. 2004, Astrophysical Journal, 617, 645

Campo Bagatin, A. & Benavidez, P. G. 2012, Monthly Notices of the RAS, 423, 1254

Chambers, J. E. 1999, Monthly Notices of the RAS, 304, 793

Chen, Y.-T. et al. 2013, Astrophysical Journal, Letters to the Editor, 775, L8

— 2016, Astrophysical Journal, Letters to the Editor, 827, L24

Cowan, N. B., Holder, G., & Kaib, N. A. 2016, Astrophysical Journal, Letters to the Editor, 822, L2

Davies, J. K., McFarland, J., Bailey, M. E., Marsden, B. G., & Ip, W. 2008, The Early Development of Ideas Concerning the Transneptunian Region, ed. Barucci, M. A., Boehnhardt, H., Cruikshank, D. P., & Morbidelli, A. , 11–23

Davis, D. R. & Farinella, P. 1997, Icarus, 125, 50

de la Fuente Marcos, C. & de la Fuente Marcos, R. 2016a, Monthly Notices of the RAS, 459, L66

— 2016b, Monthly Notices of the RAS, 462, 1972

de la Fuente Marcos, C., de la Fuente Marcos, R., & Aarseth, S. J. 2016, Monthly Notices of the RAS, 460, L123

Dohnanyi, J. S. 1969, J. Geophys. Res., 74, 2531

Dones, L., Weissman, P. R., Levison, H. F., & Duncan, M. J. 2004, Oort cloud formation and dynamics, ed. M. C. Festou, H. U. Keller, & H. A. Weaver, 153–174

Duffard, R. et al. 2014, Astronomy and Astrophysics, 564, A92

Duncan, M., Quinn, T., & Tremaine, S. 1987, Astronomical Journal, 94, 1330

Duncan, M. J. & Levison, H. F. 1997, Science, 276, 1670

Duncan, M. J., Levison, H. F., & Budd, S. M. 1995, Astronomical Journal, 110, 3073

Edgeworth, K. E. 1943, Journal of the British Astronomical Association, 53, 181

— 1949, Monthly Notices of the RAS, 109, 600

Einstein, A. 1916, Annalen der Physik, 354, 769

Elliot, J. L. et al. 2005, Astronomical Journal, 129, 1117

Fienga, A., Laskar, J., Manche, H., & Gastineau, M. 2016, Astronomy and Astrophysics, 587, L8

Fisher, N. I. 1995, Statistical Analysis of Circular Data (Cambridge University Press), 71

Fortney, J. J. et al. 2016, Astrophysical Journal, Letters to the Editor, 824, L25

Fraser, W. C. 2009, Astrophysical Journal, 706, 119

Fraser, W. C., Brown, M. E., Morbidelli, A., Parker, A., & Batygin, K. 2014, Astrophysical Journal, 782, 100

Fraser, W. C., Brown, M. E., & Schwamb, M. E. 2010, Icarus, 210, 944

Fraser, W. C. & Kavelaars, J. J. 2008, Icarus, 198, 452

— 2009, Astronomical Journal, 137, 72

Fuentes, C. I. & Holman, M. J. 2008, Astronomical Journal, 136, 83

Ginzburg, S., Sari, R., & Loeb, A. 2016, Astrophysical Journal, Letters to the Editor, 822, L11

Gladman, B. 2005, Science, 307, 71

Gladman, B. & Chan, C. 2006, Astrophysical Journal, Letters to the Editor, 643, L135

Gladman, B., Holman, M., Grav, T., Kavelaars, J., Nicholson, P., Aksnes, K., & Petit, J.-M. 2002, Icarus, 157, 269

Gladman, B. et al. 2009b, Astrophysical Journal, Letters to the Editor, 697, L91

Gladman, B. & Kavelaars, J. J. 1997, Astronomy and Astrophysics, 317, L35

Gladman, B., Kavelaars, J. J., Petit, J.-M., Morbidelli, A., Holman, M. J., & Loredo, T. 2001, Astronomical Journal, 122, 1051

Gladman, B. et al. 2012, Astronomical Journal, 144, 23

Gladman, B., Marsden, B. G., & Vanlaerhoven, C. 2008, Nomenclature in the Outer Solar System (The University of Arizona Press), 43–57

Gomes, R. S. 2003, Icarus, 161, 404

Gomes, R. S., Gallardo, T., Fernández, J. A., & Brunini, A. 2005, Celestial Mechanics and Dynamical Astronomy, 91, 109

Gomes, R. S., Matese, J. J., & Lissauer, J. J. 2006, Icarus, 184, 589

Gomes, R. S., Soares, J. S., & Brasser, R. 2015, Icarus, 258, 37

Holman, M. J. & Payne, M. J. 2016a, Astronomical Journal, 152, 80

— 2016b, Astronomical Journal, 152, 94

Ida, S., Larwood, J., & Burkert, A. 2000, Astrophysical Journal, 528, 351

Iorio, L. 2014, Monthly Notices of the RAS, 444, L78

Ivezic, Z. et al. 2008, Serbian Astronomical Journal, 176, 1

Jedicke, R., Larsen, J., & Spahr, T. 2002, Asteroids III, 71

Jewitt, D., Luu, J., & Marsden, B. G. 1992, IAU Circ., 5611

Jewitt, D., Luu, J., & Trujillo, C. 1998, Astronomical Journal, 115, 2125

Jones, R. L. et al. 2006, Icarus, 185, 508

Jones, R. L., Parker, J. W., Bieryla, A., Marsden, B. G., Gladman, B., Kavelaars, J., & Petit, J.-M. 2010, Astronomical Journal, 139, 2249

Kaib, N. A., Quinn, T., & Brasser, R. 2011a, Astronomical Journal, 141, 3

Kaib, N. A., Roškar, R., & Quinn, T. 2011b, Icarus, 215, 491

Kavelaars, J., Jones, L., Gladman, B., Parker, J. W., & Petit, J.-M. 2008, The Orbital and Spatial Distribution of the Kuiper Belt (The University of Arizona Press), 59–69

Kavelaars, J. J. et al. 2009, Astronomical Journal, 137, 4917

Kavelaars, J. J., Petit, J.-M., Gladman, B., Jone, R. L., Parker, J., & Taylor, M. 2011, in EPSC-DPS Joint Meeting 2011, 1318

Kenyon, S. J. & Bromley, B. C. 2004, Nature, 432, 598

— 2016, Astrophysical Journal, 825, 33

Kenyon, S. J. & Luu, J. X. 1998, Astronomical Journal, 115, 2136

Kuiper, G. P. 1951, in 50th Anniversary of the Yerkes Observatory and Half a Century of Progress in Astrophysics, ed. J. A. Hynek, 357

Lai, D. 2016, ArXiv e-prints

Lawler, S. M., Shankman, C., Kaib, N., Bannister, M. T., Gladman, B., & Kavelaars, J. J. 2016, ArXiv e-prints

Le Verrier, U. J. 1846, Astronomische Nachrichten, 25, 65

— 1859, Annales de l'Observatoire de Paris, 5

Leinhardt, Z. M., Stewart, S. T., & Schultz, P. H. 2008, Physical Effects of Collisions in the Kuiper Belt (The University of Arizona Press), 195–211

Levison, H. F. & Duncan, M. J. 1994, Icarus, 108, 18

Levison, H. F., Morbidelli, A., Van Laerhoven, C., Gomes, R., & Tsiganis, K. 2008, Icarus, 196, 258

Li, G. & Adams, F. C. 2016, Astrophysical Journal, Letters to the Editor, 823, L3

Linder, E. F. & Mordasini, C. 2016, Astronomy and Astrophysics, 589, A134

Luhman, K. L. 2014, Astrophysical Journal, 781, 4

Luu, J., Marsden, B. G., Jewitt, D., Trujillo, C. A., Hergenrother, C. W., Chen, J., & Offutt, W. B. 1997, Nature, 387, 573

Lykawka, P. S. & Mukai, T. 2007a, Icarus, 189, 213

— 2007b, Icarus, 192, 238

— 2008, Astronomical Journal, 135, 1161

Malhotra, R., Volk, K., & Wang, X. 2016, Astrophysical Journal, Letters to the Editor, 824, L22

Morbidelli, A., Bottke, W. F., Nesvorný, D., & Levison, H. F. 2009, Icarus, 204, 558

Morbidelli, A., Emel'yanenko, V. V., & Levison, H. F. 2004, Monthly Notices of the RAS, 355, 935

Morbidelli, A. & Levison, H. F. 2004, Astronomical Journal, 128, 2564

Mustill, A. J., Raymond, S. N., & Davies, M. B. 2016, Monthly Notices of the RAS, 460, L109

Nesvorný, D. 2015, Astronomical Journal, 150, 73

O'Brien, D. P. & Greenberg, R. 2005, Icarus, 178, 179

Pan, M. & Sari, R. 2005, Icarus, 173, 342

Parker, A. H. 2015, Icarus, 247, 112

Parker, A. H. et al. 2013, Astronomical Journal, 145, 96

Parker, A. H. & Kavelaars, J. J. 2010, Astrophysical Journal, Letters to the Editor, 722, L204

Petit, J. et al. 2016, ArXiv e-prints

Petit, J.-M., Kavelaars, J. J., Gladman, B., Jones, L., & Parker, J. 2014, in AAS/Division for Planetary Sciences Meeting Abstracts, Vol. 46, AAS/Division for Planetary Sciences Meeting Abstracts, 507.07

Petit, J.-M., Kavelaars, J. J., Gladman, B., & Loredo, T. 2008, Size Distribution of Multikilometer Transneptunian Objects (The University of Arizona Press), 71–87

Petit, J.-M., Kavelaars, J. J., Gladman, B. J., Jones, R. L., & Parker, J. W. 2015, AJ, inprep

Petit, J.-M. et al. 2017, Astronomical Journal, 153, 236

— 2011, Astronomical Journal, 142, 131

Pewsey, A., Neuhäuser, M., & Ruxton, D. 2013, Circular Statistics in R (OUP Oxford), 82–85

Philippov, J. P. & Chobanu, M. I. 2016, PASA, 33, e033

Pike, R. E., Kavelaars, J. J., Petit, J. M., Gladman, B. J., Alexandersen, M., Volk, K., & Shankman, C. J. 2015, Astronomical Journal, 149, 202

Pike, R. E., Lawler, S., Brasser, R., Shankman, C. J., Alexandersen, M., & Kavelaars, J. J. 2017, Astronomical Journal, 153, 127

Santos-Sanz, P. et al. 2012, Astronomy and Astrophysics, 541, A92

Schlichting, H. E., Fuentes, C. I., & Trilling, D. E. 2013, Astronomical Journal, 146, 36

Schwamb, M. E., Brown, M. E., & Rabinowitz, D. L. 2009, Astrophysical Journal, Letters to the Editor, 694, L45

Shankman, C. 2012, Master's thesis, University of British Columbia

Shankman, C., Gladman, B. J., Kaib, N., Kavelaars, J. J., & Petit, J. M. 2013, Astrophysical Journal Letters, 764, L2

Shankman, C. et al. 2016, Astronomical Journal, 151, 31

Shankman, C., Kavelaars, J. J., Lawler, S. M., Gladman, B. J., & Bannister, M. T. 2017, Astronomical Journal, 153, 63

Sheppard, S. S. & Trujillo, C. 2016, ArXiv e-prints

Sheppard, S. S. & Trujillo, C. A. 2010, Astrophysical Journal Letters, 723, L233

Sivaram, C., Kenath, A., & Kiren, O. V. 2016, Astrophysics and Space Science, 361, 230

Soares, J. S. & Gomes, R. S. 2013, Astronomy and Astrophysics, 553, A110

Solontoi, M. et al. 2012, Icarus, 218, 571

Stansberry, J., Grundy, W., Brown, M., Cruikshank, D., Spencer, J., Trilling, D., & Margot, J.-L. 2008, Physical Properties of Kuiper Belt and Centaur Objects: Constraints from the Spitzer Space Telescope (The University of Arizona Press), 161–179

Thommes, E. W., Duncan, M. J., & Levison, H. F. 2002, Astronomical Journal, 123, 2862

Toth, I. 2016, Astronomy and Astrophysics, 592, A86

Trujillo, C. A., Jewitt, D. C., & Luu, J. X. 2000, Astrophysical Journal, Letters to the Editor, 529, L103

Trujillo, C. A. & Sheppard, S. S. 2014, Nature, 507, 471

Veras, D. 2016, Monthly Notices of the RAS, 463, 2958

Veras, D. & Evans, N. W. 2013, Celestial Mechanics and Dynamical Astronomy, 115, 123

Volk, K. & Malhotra, R. 2008, Astrophysical Journal, 687, 714

Wang, J.-H. et al. 2009, Astronomical Journal, 138, 1893

Wyatt, M. C., Dermott, S. F., Telesco, C. M., Fisher, R. S., Grogan, K., Holmes, E. K., & Piña, R. K. 1999, Astrophysical Journal, 527, 918